Environmental Impacts of Firefighting Foams

Dissertation

zur Erlangung des akademischen Grades

Doktoringenieur

(Dr.-Ing.)

von M.Sc. Ardalan Fakhr Darbanan
geb. am 20.04.1988 in Mashhad, Iran

genehmigt durch die Fakultät für Verfahrens-und Systemtechnik
der Otto-von-Guericke-Universität Magdeburg

Promotionskommission: Prof. Dr.-Ing. habil. Eckehard Specht (Vorsitz)
Prof. Dr.-Ing. habil. Ulrich Krause (Gutachter)
Prof. Dr.-Ing. Stefanie Schubert-Polzin (Gutachter)
Assoc. Prof. Dr.-Ing. Bjarne Husted (Gutachter)

eingereicht am: 31.01.2020
Promotionskolloquium am: 16.06.2020

Dedicated to:

Eram

Abstract

In this study, three different strategies for encountering an open fire, based on their contribution to the occurrence of different environmental threats, were compared. The strategies are namely: (1) extinguishing the fire with water, (2) extinguishing the fire with CAF and (3) letting the fire burn.

Air dispersion modeling was applied to investigate the evolution of the smoke plume (air-borne pollutants) under different atmospheric conditions. The results show that the massive smoke plume produced during a large fire can affect the air quality even at very far distances from the fire. Accordingly, ‘letting the fire burn’ is not an option to deal with a large open fire since it results in the pollution of a considerably large zone near the surface for a long time. However, the smoke affected volume and degree of the suppression of pollutants near the surface depend on the meteorological condition.

To compare the environmental impacts of water and CAF as the alternative agents for extinguishing class A fires, a comparison according to the fire suppression effectiveness between both agents is necessary. In this regard, a set of small-scale indoor fire tests were conducted. The experimental results show up to 30 % higher fire-fighting efficiency of CAF over water. Higher fire-fighting efficiency results in less water consumption for extinguishment and consequently less amount of run-off water. So, the application of CAF reduces the amount of polluted soil that should be remedied after the extinguishment. This is the main environmental advantage of CAF over water.

The pollutants in the run-off can enter groundwater via infiltration into the soil. The traveling time for the pollutants to reach groundwater was investigated for soils with different textures by the simulation of flow in the vadose zone (unsaturated porous medium). The analysis was based on the concept of ‘groundwater vulnerability’. The traveling time can vary from several hours to weeks, depending on the textural class of the soil and depth of the water table. However, the application of either water or CAF as the extinguishing agent does not affect the traveling time for pollutants to groundwater.

Keywords: Compressed air foam (CAF), fire suppression effectiveness, CFD, vadose zone, air dispersion, unsaturated porous media

Zusammenfassung

In dieser Studie wurden verschiedene Strategien verglichen, einem offenen Feuer zu begegnen, basierend auf ihrem Beitrag zum Auftreten verschiedener ökologischer Risiken. Die Strategien sind (1) das Feuer mit Wasser löschen, (2) das Feuer mit CAF löschen und (3) das Feuer brennen lassen.

Modellierung der Schadstoffausbreitung wurde angewandt, um die Entwicklung der Rauchwolke (Luftschadstoffe) unter verschiedenen atmosphärischen Bedingungen zu untersuchen. Die Ergebnisse zeigen, dass die während eines großen Feuers erzeugte massive Rauchwolke die Luftqualität selbst von sehr weiter Entfernung aus beeinflusst. Dementsprechend ist „Das Feuer brennen lassen“ keine Option, um dem großen offenen Feuer zu begegnen, da es die Verschmutzung eines Bereichs nahe der Erdoberfläche von bedeutender Größe für eine geraume Zeit herbeiführt. Jedoch hängen das von Rauch betroffene Volumen und der Grad der Unterdrückung der Schadstoffe nahe der Erdoberfläche von den Wetterbedingungen ab.

Um die Umweltfolgen (-beeinträchtigung, -belastung) von Wasser und CAF als alternative Wirkstoffe zum Löschen des Klasse-A-Feuers zu vergleichen, ist ein Vergleich beider Mittel entsprechend der Effektivität der Feuerunterdrückung nötig. Zu diesem Zweck wurden eine Reihe kleiner Feuertests im Innenraum vorgenommen. Die Ergebnisse der Experimente zeigen eine um 30 % höhere Feuerbekämpfungseffizienz von CAF über Wasser. Die höhere Feuerbekämpfungseffizienz hat einen geringeren Wasserverbrauch beim Löschen zur Folge und folglich eine kleinere Menge von kontaminiertem Wasser. Somit reduziert die Verwendung von CAF die Menge verschmutzten Bodens, die nach der Löschung behoben werden muss. Dies stellt den primären Umweltvorteil von CAF über Wasser dar.

Die Schadstoffe im Abwasser dringen durch Infiltration des Bodens in das Grundwasser ein. Die Beförderungszeit der Schadstoffe in das Grundwasser wurde für Böden mit unterschiedlicher Textur untersucht durch die Simulation der Strömung in der vadosen Zone (ungesättigtes durchlässiges Medium). Die Analyse hat auf dem Konzept von „Grundwasser Vulnerabilität“ basiert. Die Beförderungszeit kann zwischen mehreren Stunden bis zu Wochen variieren, abhängig von der Texturart des Bodens und der Tiefe der wasserführenden Schichten. Nichtsdestotrotz ändert die Anwendung weder von Wasser noch von CAF als Löschmittel die Beförderungszeit des Schadstoffs in das Grundwasser.

Stichwörter: Druckluftschaum (CAF), Feuerbekämpfungseffizienz, CFD, Vadose Zone, air dispersion, ungesättigtes durchlässiges Medium

Table of Contents

List of Figures

List of Tables

Nomenclature

Symbol	Definition	Dimensions
A_t	Total surface area of the mixed crib	$[m^2]$
C_p	Specific moisture capacity	$[m^{-1}]$
c	Concentration	$[mol\, m^{-3}]$
c_0	Initial concentration	$[mol\, m^{-3}]$
$c_{p,air}$	Specific heat capacity of air	$[Jkg^{-1}K^{-1}]$
D	Hydrodynamic dispersion coefficient	$[m^2 s^{-1}]$
D_o	Diffusion coefficient	$[m^2 s^{-1}]$
D_{ii}	Longitudinal hydrodynamic dispersion coefficient	$[m^2 s^{-1}]$
D_{ij}	Transverse hydrodynamic dispersion coefficients	$[m^2 s^{-1}]$
D_p	Grain diameter	$[m]$
$D(\theta)$	Water diffusivity	$[m^2 s^{-1}]$
E	Total mechanical energy	$[J]$
g	Gravitational acceleration	$[ms^{-2}]$
H	Hydraulic Head	$[m]$
H_b	Air entry pressure head	$[m]$
H_p	Pressure Head	$[m]$
$h(D_p)$	Density function for the diameter distribution	$[-]$
K_s	Saturated Hydraulic conductivity	$[ms^{-1}]$
$K(S_e)$	Saturated hydraulic conductivity	$[ms^{-1}]$
k	Absolute permeability	$[m^2]$
k_{tur}	Turbulence kinetic energy	$[m^2 s^{-2}]$

L	Length of flow path	$[m]$
L_g	Real length of the flow path	$[m]$
L_s	shortest possible length of the flow path	$[m]$
M_{air}	Molar mass of air	$[kgmol^{-1}]$
m	Van-Genuchten shape parameter	$[-]$
m_α	Mass of component α	$[kg]$
$\dot{m}$	Mass flow	$[kg\ s^{-1}]$
m''	Mass flow per unit area	$[kg\ m^{-2}s^{-1}]$
n	Van-Genuchten shape parameter	$[-]$
p	Pressure	$[Pa]$
p_0	Pressure at the ground surface	$[Pa]$
P_c	Capillary Pressure	$[Pa]$
P_{nw}	Pressure in non-wetting phase	$[Pa]$
P_w	Pressure in wetting phase	$[Pa]$
Q	Heat	$[J]$
q	Darcy flux	$[ms^{-1}]$
q_{ad}	Advection flux	$[mol\ m^{-2}s^{-1}]$
q_{dif}	Diffusion Flux	$[mol\ m^{-2}s^{-1}]$
R	Universal ideal gas constant	$[Jmol^{-1}K^{-1}]$
Re	Reynolds number	$[-]$
r	Radius of pore throat	$[m]$
S	Storage coefficient	$[m^{-1}]$
S_e	Effective saturation of soil	$[-]$
S_x	Matchpoint or effective wetting-point saturation	$[-]$

S_y	Specific yield	$[-]$
T	Temperature	$[°k]$
T_i	Turbulence intensity	$[-]$
t	Time	$[s]$
U	Internal energy	$[J]$
u	x-component of velocity	$[ms^{-1}]$
V	Volume	$[m^3]$
V_{max}	Maximum volume of REV	$[m^3]$
V_{min}	Minimum volume of REV	$[m^3]$
V_p	Volume occupied by total number of pores	$[m^3]$
$V_{p,e}$	Total volume of interconnected pores	$[m^3]$
V_T	Total volume of soil	$[m^3]$
V_w	Volume occupied by water	$[m^3]$
v	y-component of velocity	$[ms^{-1}]$
v_{10}	Wind speed at the height of 10 m	$[ms^{-1}]$
W	Work	$[J]$
w	z-component of velocity	$[ms^{-1}]$
Y_i	Mass fraction of the species i	$[-]$
z	Elevation	$[m]$
z_0	Roughness length	$[m]$
α	Van-Genuchten pressure scaling parameter	$[m^{-1}]$
α_L	Longitudinal dispersivity	$[m]$
α_t	Transverse dispersivity	$[m]$
α_x	Porous media compressibility coefficient	$[ms^2kg^{-1}]$

β	Fluid compressibility coefficient	$[ms^2kg^{-1}]$
Γ	Dry adiabatic lapse rate	$[°k\ m^{-1}]$
Θ	Potential temperature	$[°k]$
θ	Water content	$[-]$
θ_r	Residual Liquid volume fraction	$[-]$
θ_s	Saturated Liquid volume fraction	$[-]$
θ_x	Contact angle	$[°]$
Λ	Actual lapse rate	$[°k\ m^{-1}]$
Λ	Pore size distribution index	$[-]$
μ_t	Turbulent viscosity	$[Pa\ s]$
μ_w	Dynamic viscosity of water	$[Pa\ s]$
ρ	Density	$[kg\ m^{-3}]$
ρ_w	Density of water	$[kg\ m^{-3}]$
σ	Interfacial tension	$[Jm^{-2}]$
τ_g	Geometrical tortuosity	$[-]$
Φ	Equivalence ratio	$[-]$
ϕ	Porosity	$[-]$
ϕ_e	Effective porosity	$[-]$

Abbreviations

ABL	Atmospheric Boundary
ASTM	American Society for Testing and Materials
B-C	Brooks-Corey
CAF	Compressed Air Foam
CFD	Computational Fluid Dynamics
DIN	German Institute for Standardization
ISSS	International Soil Science Society
LES	Large Eddy Simulation
PDE	Partial Differential Equation
REV	Representative Elementary Volume
RANS	Reynolds-Averaged Navier-Stokes
SCW	Superiority of CAF over Water
USDA	U.S. Department of Agriculture
V-G	Van-Genuchten
RW	Run-off Water
TW	Total water

1 Introduction

The environmental impacts of large open fires have always been a problematic issue for human beings. Open fires threaten air quality, soil and aquatic environment; therefore, selection of an efficient strategy to encounter and deal with an open fire is a subject of importance from the standpoint of environmental engineers and scientists.

Traditionally, water has been the most popular extinguishing agent for extinguishing class A fires. Class A fires are fires from the burning of solid combustible materials. However, various studies have noticed in the last eighty years that water is not always the most efficient fire-fighting agent [1, 2]. Although water has a high latent heat of vaporization which results in high cooling capacity, there are still serious restrictions for water to be applied generally as the extinguishing agent for all fires. The high surface tension of water prevents it to penetrate the burning material. Only 5 to 10 % of water gets involved in the extinguishing process upon its application [3], the rest runs away and leads to further financial and environmental damages.

Compressed air foam (CAF) technology addresses efficiently the drawbacks incorporated by using water as the fire-fighting agent. CAF is generated by mixing water, foam concentrate and compressed air (figure 1.1). A combination of water and foam concentrate in proper proportions creates the foam solution, then, compressed air is injected.

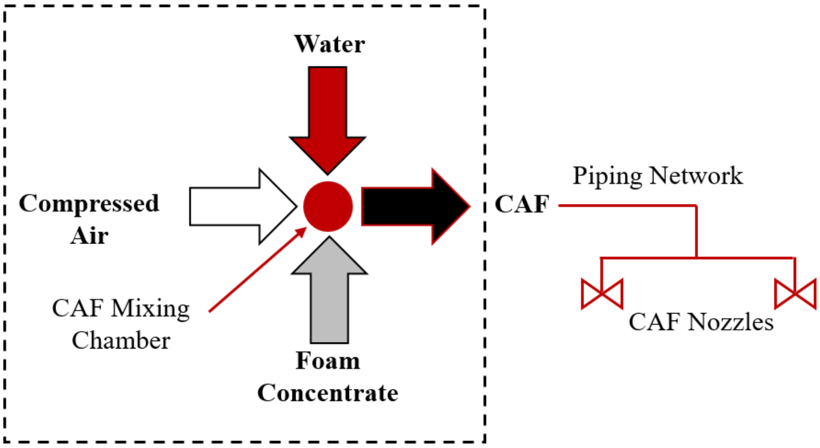

Figure 1.1: Compressed air foam system

Two important aspects of CAF technology improve its extinguishing ability over that of water. First, the surface tension of the liquid decreases to approximately one-third of the value of water due to the addition of the detergent [1]. Lower surface tension provides the possibility for the extinguishing agent to penetrate more into the burning material. Secondly, the injection of compressed air causes a large volume expansion of the extinguishing agent. The expanded agent can cover the fuel surface and establish a stable blanket over the burning material. This coverage acts as a barrier depriving the fire of air (oxygen) [4]. The latter technique is counted as the most innovative aspect of the CAF technology. However, other benefits such as high injection momentum and less water usage have also been mentioned for CAF [5].

One significant environmental threat of open fires is the contaminated run-off water after the extinguishment process. Run-off water flows over the land and eventually, a considerable portion of run-off infiltrates the soil. This infiltration flux pollutes the soil and is also susceptible to reach the groundwater which is one of the main resources of drinking water. Therefore, understanding water flow and solute transport in the soil is of importance to determine the risk of soil and groundwater pollution. The first layers of soil beneath the surface, also called the vadose zone, are partially saturated by water. The existence of air as the second fluid phase affects the hydraulic properties of the unsaturated zone. To characterize the water flow in the vadose zone, the relationship between the pore water pressure, water content and unsaturated hydraulic conductivity $(H_p - \theta - K)$ is required. This functional relationship is called the water retention function. Different authors proposed various parametric models for the retention function, out of which the van-Genuchten [6] and Brooks-Corey [7] are the most commonly used according to scientific citations [8]. The van-Genuchten (V-G) model is a more accurate predictor of the water retention curve and consequently the unsaturated hydraulic conductivity as the main regulator of flow in the partially saturated soils. The V-G function is continuous and applicable for every kind of soil at any degree of saturation. However, the mathematical complexity of the model makes it computationally expensive. On the other hand, the Brooks-Corey (B-C) model estimates the retention function by a simple power-law function which is easy to implement in the numerical modeling but not as precise as the V-G function. The B-C model performs relatively well for coarse-textured soils, but it loses its accuracy for finer-textured soils. Another undesirable feature of the B-C model is the discontinuity of the retention function near the saturation point which leads to numerical difficulties [6]. This is mainly due to the lack of well-defined air entry pressure value (the pressure head at which the first bubble of air enters the largest pore of the medium).

The other environmental threat of open fires is the massive smoke plume which can endanger the air quality at far distances from the fire. Smoke consists of various airborne toxicants and is the main concern in the non-thermal hazard analysis of a fire accident. The airborne pollutants released from a fire are transported by wind. The degree of dispersion of pollutants depends on the degree of turbulence in the atmosphere. In other words, the degree of turbulence in the atmosphere determines the concentrations at which the pollutants are present at different locations surrounding the pollutant source (fire). Air dispersion modeling is a tool to predict the fate of the pollutants. The main factors affecting the behavior of the smoke plume are the meteorological conditions, landscape, pollution source characteristics, and properties of the pollutants. Characterization of the meteorological condition requires knowledge about the vertical structure of the atmosphere which depends on the atmospheric stability. The most well-known atmospheric stability classification has been proposed by Pasquill-Gifford [9, 10] considering the influence of both solar radiation and wind speed. Having information about the atmospheric stability and wind velocity field is necessary for dispersion modeling. The most widely applied dispersion models are the Gaussian Plume Model, Stochastic Lagrangian Particle Model and Computational Fluid Dynamics (CFD). CFD is the most comprehensive and also computationally intensive method. CFD solves the bulk wind flow by the solution of the Navier-Stokes equation on a fixed grid. To calculate the concentration of smoke components, one extra transport equation should be implemented for each component.

The main objective of this study is to investigate the environmental impacts of CAF as the fire extinguisher. Some environmental concerns have recently arisen regarding the existence of chemical detergent in the foam solution. However, there is a lack of knowledge about the environmental damages or benefits which might appear upon the application of CAF as the fire extinguisher instead of water. This research compares quantitatively the impacts of CAF on soil pollution, groundwater and air pollution compared to alternative fire-fighting strategies. For this purpose, the following three strategies for encountering an open fire are compared: (1) extinguishing the fire with water, (2) extinguishing the fire with CAF and (3) letting the fire burn. In this regard, two imaginary fire scenarios are taken into consideration; two fires with different burning areas of $50 \times 50\ m^2$ and $100 \times 100\ m^2$. COMSOL Multiphysics 5.2 is used for the flow simulation in the unsaturated soil, and the dispersion modeling is carried out using ANSYS FLUENT 17.0.

This thesis includes seven chapters. Chapter 2 describes the fundamental concepts related to porous structures and solute transport in unsaturated soils including a review of the main parametric models characterizing the water retention curve. Chapter 3 provides the theoretical background of air dispersion modeling and atmospheric stability with a focus on the Pasquill-Gifford stability classification. In chapter 4, the experimental setup and results of the small scale class A fire tests are presented. The experiments aimed to compare the fire suppression effectiveness of CAF and water. Chapter 5 describes the simulation of the infiltration of run-off water through the vadose zone using both Brooks-Corey and van-Genuchten models including the error analysis. Chapter 6 describes the simulation of the smoke plume behavior under different atmospheric stability classes. Finally, the conclusions are presented in chapter 7.

2 Subsurface Flows

Terminology for subsurface waters

In hydrology, the flow of water in the soil beneath the earth's surface is referred to as the subsurface flow. There are two main categories of subsurface waters: the near-surface unsaturated or vadose zone and the deeper zone which is called the saturated or phreatic zone (figure 2.1). The boundary between these two zones is called water table and is denoted with the symbol ∇. Technically, the water table is recognized as the surface on which the water pressure in the pores equals the atmospheric pressure. The phreatic surface can also be used as an alternative term for the water table.

The unsaturated zone or vadose zone is positioned between the ground surface and the water table where the pore water pressure is less than the atmospheric pressure. In the vadose zone, air also occupies some pore spaces. The existence of two immiscible phases results in the appearance of capillary effects and consequently a negative pore water pressure. The vadose zone plays an important role as the hydrological connection between the surface water component of the hydrological cycle and the groundwater component [11].

Below the water table, where all the pores are saturated by water, is the saturated zone or phreatic zone. In the saturated zone, the water pressures exceed the atmospheric pressure. Groundwater is the term applied to the water in this zone.

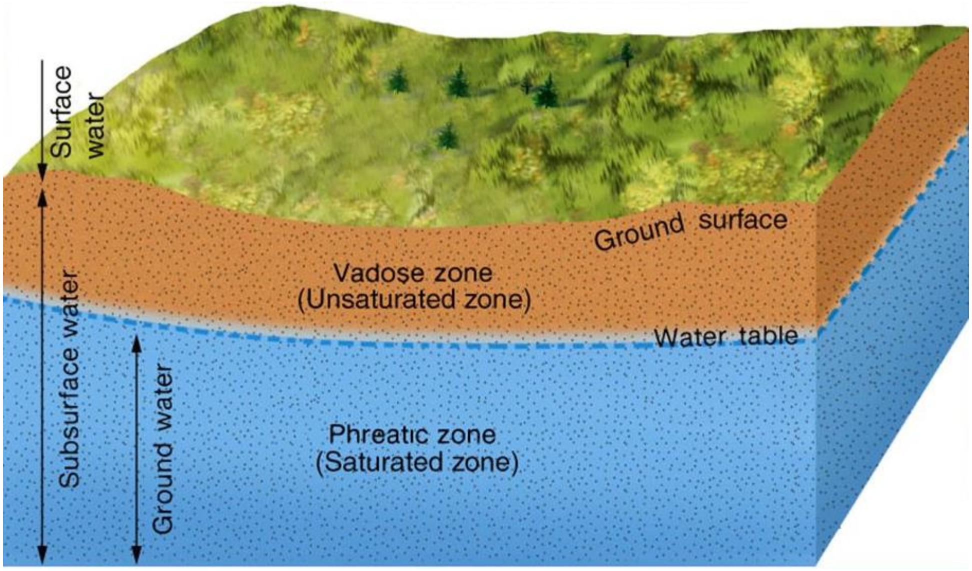

Figure 2.1: Subsurface water flow diagram showing unsaturated and saturated zones [12]

There is also another zone which is saturated by water but above the water table. This zone is named capillary fringe and has traditionally been assigned to the vadose zone. The thickness of the capillary fringe depends on the pore structure of the soil medium. Media with large pore sizes have thinner capillary fringes than media with smaller pore sizes. The pore water pressure in different zones of subsurface water is qualitatively depicted in figure 2.2.

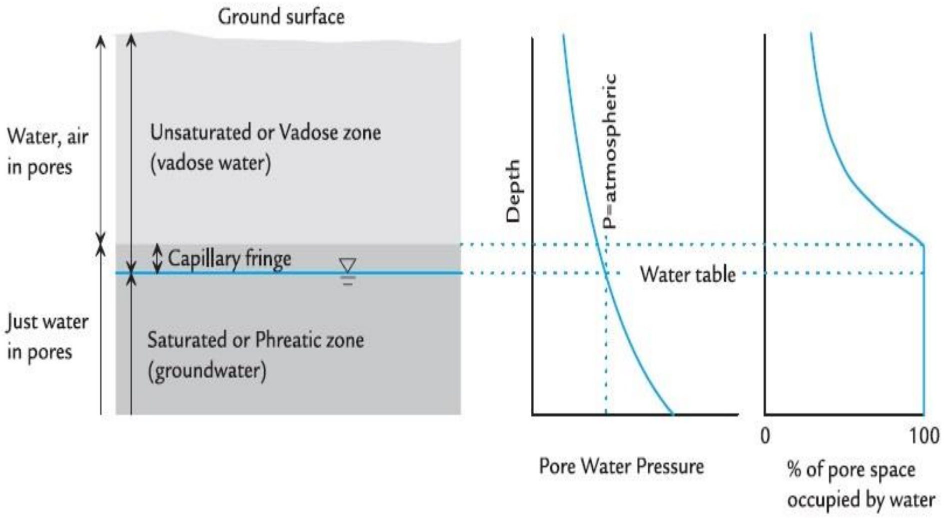

Figure 2.2: Pore water pressure variations with depth [13]

Fluxes affecting groundwater

The hydrological cycle describes the interactions between water above, on and below the Earth’s surface. All water fluxes contributing to the hydrological cycle are illustrated in figure 2.3, out of which only infiltration, recharge, overland flow, and interflow are the subjects of importance in groundwater science. The water brought to the land surface via precipitation may enter into subsurface due to ground porosity or flow over the ground surface. The infiltrated water is called infiltration flux whereas the run-off water is the overland flow. However, a part of the surface water is always evaporated. The infiltrated water in the unsaturated zone can be divided into two main fluxes. A part of it passes through the unsaturated zone and eventually reaches the saturated zone. This is called recharge which is the main issue of hydrology [14]. A part of the water in the unsaturated zone also moves laterally and finally reaches a water body. This flux is called interflow.

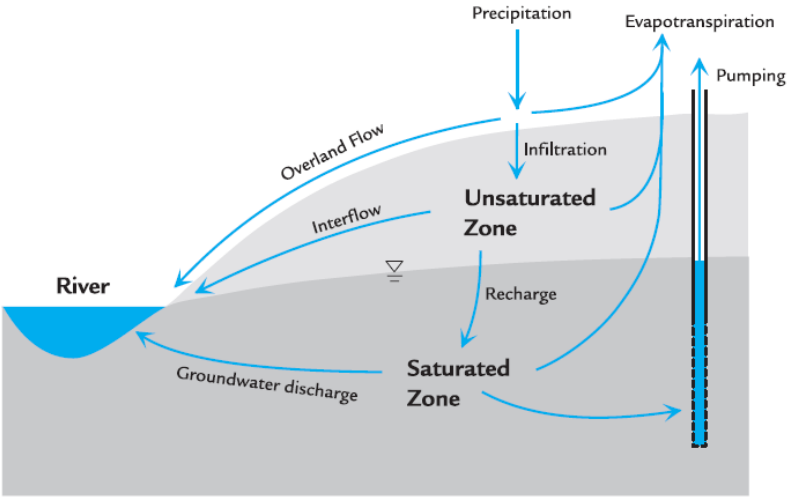

Figure 2.3: Water fluxes contributing to the hydrological cycle [13]

General characteristics of soil

Soil is a three-phase system that is a combination of solid particles, liquid, and gas [15]. The solid phase occurs in a wide range of sizes and shapes. The liquid phase is water containing various dissolved substances, whereas air is the gaseous phase. Typically, the soil is treated as a natural porous medium.

The soil texture is determined based on the size distribution of solid particles in the soil. Particle diameters can vary from over 100 mm to about 0.0001 mm. Conventionally, the soil is considered as the medium with particles smaller than 2 mm in diameter whereas a medium with larger particles is referred to as gravel. The largest soil particles are named sand, the smallest particles are defined as clay whereas the particles of intermediate size constitute the silt. In general, sand particles can be considered as spherical although they have jagged surfaces. Silt particles have the same characteristics as sand particles but are smaller, implying that silt exhibits a greater surface area per unit mass. Clay has plate-like or needle-like particles, which have noticeably high surface area per unit mass [16]. The most famous schemes for the textural classification of soils were introduced by USDA (U.S. Department of Agriculture) and the ISSS (International Soil Science Society) (figure 2.4). In both schemes, clay consists of particles smaller than 0.002 mm. According to USDA, sand has particles between 2 and 0.05 mm in diameter but ISSS defines sand as particles ranging in diameter between 2 and 0.02 mm. Therefore, silt particles lay in the range of 0.05 to 0.002 mm based on USDA and between 0.02 and 0.002 mm based on ISSS.

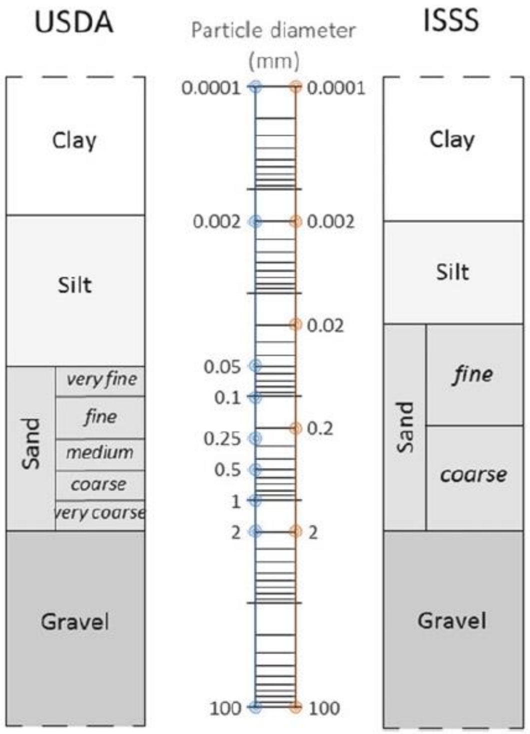

Figure 2.4: Particle sizes of different soils according to USDA and ISSS [17]

For any type of soil, the textural class is determined by the textural triangle (figure 2.5) according to the mass percentage of clay, silt, and sand. The triangle has twelve sections and gives names associated with various combinations of sand, silt and, clay. The twelve classes represented by the textural triangle are as follows:

- Clay
- Sandy clay
- Silty clay
- Sandy clay loam
- Clay loam
- Silty clay loam
- Sand
- Loamy sand
- Sandy loam
- Loam
- Silt loam
- Silt

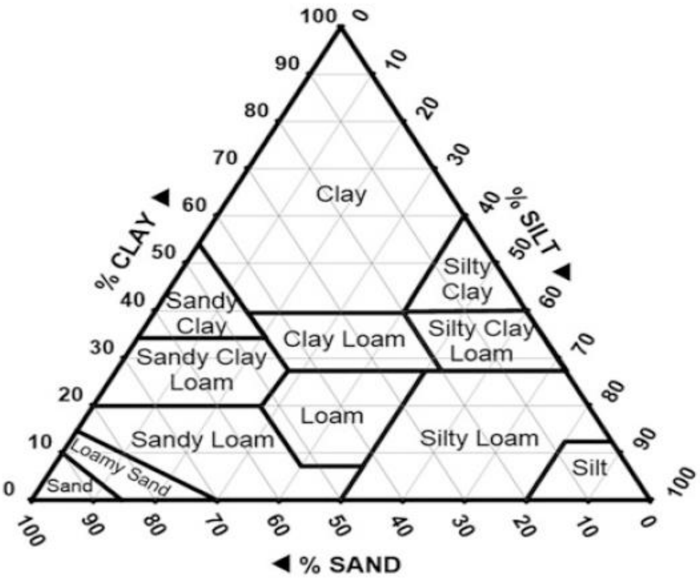

Figure 2.5: Soil textural triangle [18]

Porous media

A porous medium is defined as a medium consisting of a solid matrix with interconnected pores. The solid matrix is generally assumed as a rigid body. Porous media are able to transfer fluids due to the interconnectedness of the void.

Contrary to man-made porous materials, the morphology of the natural ones is not completely well-understood. In a natural porous medium, the geometry of the pores is highly irregular and stochastic with respect to the shape and size distribution. The porous media are mainly characterized based on their intrinsic properties which are introduced in this section.

2.1.1 Macroscopic consideration of porous media

There are two main approaches for the consideration of porous media and the transport mechanisms within that:

1) Microscale consideration
2) Macroscale consideration

In the microscopic approach, a mathematical point in the system is considered either within considering phase or at the interface between phases [19]. So, the microscopic approach recognizes all the discontinuities in the variables at length scales smaller than the pore or grain diameter. Due to the small length scale, pore structure and configuration should be taken into consideration for modeling the transport phenomena in the porous media. Complexity and irregularity of pore geometries at the microscopic scale make the microscopic approach practically very expensive with respect to mathematical formulation and solution of the governing equation [20].

In the macroscopic approach, all the microscopic phase properties and transport equations are averaged over a representative elementary volume (REV) (figure 2.6). Averaging the properties over a control volume results in the vanishment of the discontinuities identified in the microscopic approach. As Gray (2000) [21] stated "Flow in porous media is typically modeled at a length scale, referred to as macroscale, such that a point of the system encompasses tens to hundreds of pore diameters. To obtain the conservation equations at this scale, averaging theorems for the phases have been employed such that quantities appearing in the equations (i.e., density and velocity) are in fact average values from a region surrounding a point of interest."

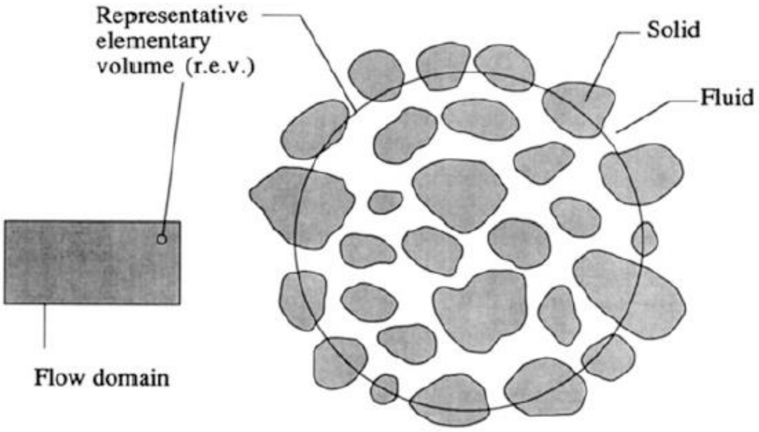

Figure 2.6: Representative elementary volume (REV) [22]

The representative elementary volume (REV) is defined as "the range of volumes for which all averaged geometrical characteristics are single-valued functions of the location of that point and time." [23] The main issue in this regard is the determination of the domain for the representative elementary volume. There is a volume range over which the averaged properties remain homogeneous. As illustrated by the figure (2.7), any averaged property fluctuates when the REV is smaller than a certain size. On the other hand, the assumption of homogeneity of the medium fails if the REV is chosen to be very large. Therefore, the size of the REV must be selected between the upper and lower limit to fulfill the assumption of homogeneity of the medium.

$$V_{min} < V < V_{max} \tag{2.1}$$

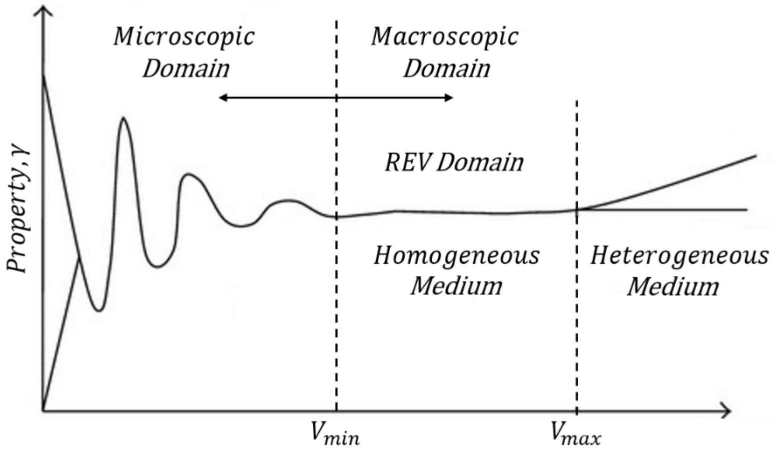

Figure 2.7: Conceptualization of the domain size for REV [20]

2.1.2 Porosity

The porosity ϕ of a porous medium is defined as the ratio of the void volume to the total volume (bulk volume). Porosity is a dimensionless number and varies between 0 and 1.

$$\phi = \frac{V_p}{V_t} \tag{2.2}$$

Where V_p $[m^3]$ is the volume occupied by pores and V_t $[m^3]$ is the total volume of the medium. The equation above refers to absolute porosity while in a natural porous medium not all the pores are interconnected. However, from the standpoint of flow through the porous material, only the interconnected pores are of importance. The dead-end pores do not contribute to the flow and the fluid is stagnant in such pores (figure 2.8). Thus, the concept of effective porosity based on the total volume of interconnected pores $V_{p,e}$ $[m^3]$ is introduced:

$$\phi_e = \frac{V_{p,e}}{V_t} \tag{2.3}$$

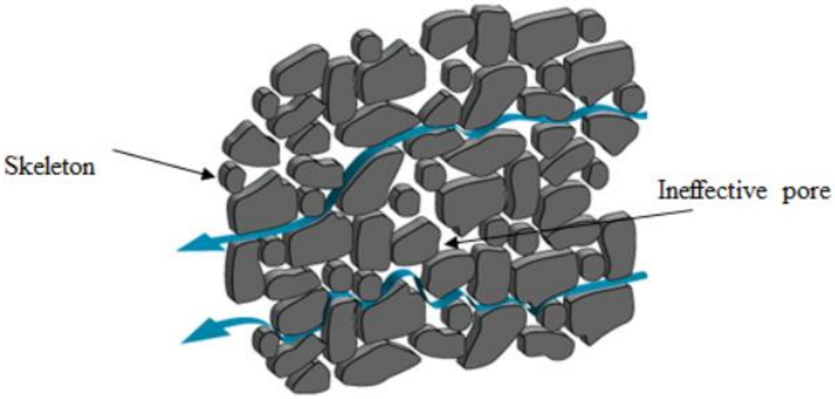

Figure 2.8: Representation of effective and ineffective pores [24]

Table 2.1 provides the typical range of values for the porosity of the main geological materials according to study of Davis (1969) [25].

Table 2.1: Typical values for porosities

Material	Porosity
Narrowly graded silt, sand, gravel	0.3 to 0.5
Widely graded silt, sand, gravel	0.2 to 0.35
Clay, clay-silt	0.35 to 0.6
Sandstone	0.05 to 0.3
Limestone, dolomite	0 to 0.4
Shale	0 to 0.1
Crystalline rock	0 to 0.1

2.1.3 Specific surface area

The specific surface area S_v is the ratio of the internal surface area of the pores and the total volume of the porous medium. The specific surface area strongly influences the magnitude of the capillary force. The smaller the pores are, the higher the specific surface area is.

2.1.4 Tortuosity

Geometrical tortuosity (τ_g) is another important characteristic of a porous medium which is defined as the ratio of the real length (L_g) of the flow path of a fluid particle through the medium to the shortest distance (L_s) between the starting and finishing points of the particles flow path.

The shortest distance is the length of the straight line between the two points. Due to the chaotic structure of the porous materials, the flow paths are not straight but tortuous. Then, the tortuosity factor (τ_g) is always greater than unity and mathematically introduced as following:

$$\tau_g = \frac{L_g}{L_s} \tag{2.4}$$

However, tortuosity is a crucial factor to investigate electrical and hydraulic conductivity of the medium, and also to estimate the traveling time and length for a fluid particle dispersing through the medium [26]. The concept of tortuosity is depicted in figure 2.9.

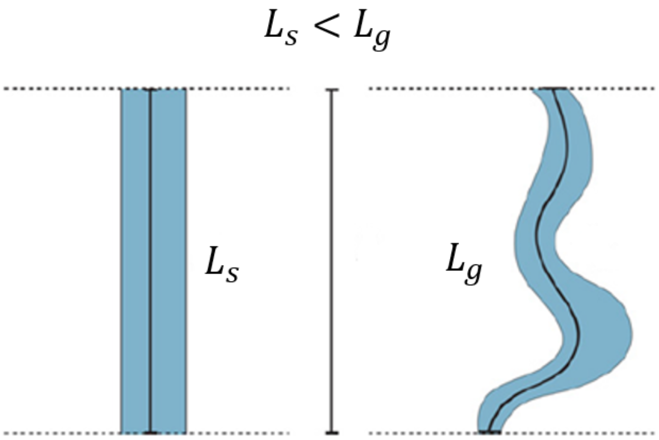

Figure 2.9: The concept of tortuosity, **(left)** straight flow path, **(right)** real tortuous path [27]

Several authors discussed different concepts of tortuosity such as hydraulic tortuosity and electrical tortuosity but they are not considered as intrinsic properties of the porous medium anymore [28-30]. For example, the hydraulic tortuosity depends also on the type of the flow and the degree of saturation of the medium and not only of the geometry of the pores.

2.1.5 Permeability

Absolute permeability k $[m^2]$ is a measure of the capacity and ability of a porous medium to transmit fluids. It is an intrinsic property of the medium in the sense that it is independent of the nature of the flow. Permeability is a complex function of different morphological variables of the medium. A great deal of effort has been spent to develop a model to estimate the permeability of the porous media. The simplified models express the permeability just as a function of porosity [31]. However, the permeability is strongly affected by pore configuration and not only by porosity. Among the different developed relationships that connect permeability, porosity, and pore structure, the Carman-Kozeny model is the most popular based on scientific citations. The Carman-Kozeny formula to calculate the permeability is expressed as [32, 33]:

$$k = \frac{D_{p2}^2 \phi^3}{180\,(1-\phi)^2} \tag{2.5}$$

Where:

$$D_{p2} = \frac{\int_0^\infty D_p^3\, h(D_p)\, dD_p}{\int_0^\infty D_p^2\, h(D_p)\, dD_p} \tag{2.6}$$

$h(D_p)$ is the density function for the diameter distribution and D_p $[m]$ is the particles' diameter. 180 is the curve fitting constant based on experimental results. The equation was originally derived for media with approximately spherical particles whose diameters experience a relatively narrow range. However, the Carman-Kozeny equation was modified by different scientists to be applicable under different circumstances [25, 34-37].

Hydraulic properties of the vadose zone

In the vadose zone, air occupies some pore spaces besides water. The existence of air as the second fluid phase changes the hydraulic properties of the soil compared to the completely saturated condition. Characterization of water movement in the unsaturated zone includes the estimation of the functional relationship between the pore water pressure, water content and unsaturated hydraulic conductivity ($H_p - \theta - K$).

2.1.6 Soil water content

The soil water content θ is the ratio of the volume of pores filled by water to the total volume.

$$\theta = \frac{V_w}{V_t} \tag{2.7}$$

Where V_w $[m^3]$ is the volume occupied by water and V_t $[m^3]$ is the total volume. The volumetric water content is a key factor to calculate the fluxes and water amount added to or removed from the soil. In most hydrologic applications, the normalized form of water content, also known as effective saturation S_e, is used.

$$S_e = \frac{\theta - \theta_r}{\theta_s - \theta_r} \tag{2.8}$$

Here, θ_s is the water content at saturation (maximum volumetric water content in soil). Theoretically, θ_s equals the porosity but practically it is always less than the porosity. This is because of the presence of entrapped or dissolved air. In general, θ_s is about 5 to 10 percent less than effective porosity [38]. θ_r is the residual water content and has an ambiguous physical meaning [11]. It refers to the maximum amount of water that does not contribute to water flow [39]. Soils with finer texture (smaller pores) have a higher value of residual water content (θ_r) [40].

2.1.7 Wettability

Wettability describes the preference of a solid surface to attract a fluid in the presence of another immiscible fluid [41]. Wettability has meaning when there is more than one phase present in the medium and is the result of the competition between adhesive forces between each fluid phase and the solid surface. The fluid phase which spreads across the solid surface is called the wetting phase whereas the fluid phase which has a tendency to minimize its contact surface with the solid surface is the non-wetting phase [42, 43].

Quantification of the wettability is by the contact angle θ_x. The contact angle is the angle formed when the interface between both fluid phases meets the solid surface. For a liquid droplet deposited on a solid surface (figure 2.10), the Young equation [44] gives the contact angle.

$$\sigma_{SG} - \sigma_{SL} - \sigma_{LG} \cos \theta_x = 0 \tag{2.9}$$

The Young equation is a force balance among interfacial tensions between solid/gas, solid/liquid and gas/liquid ($\sigma_{SG}, \sigma_{SL}, \sigma_{LG}$) interfaces under static condition [45].

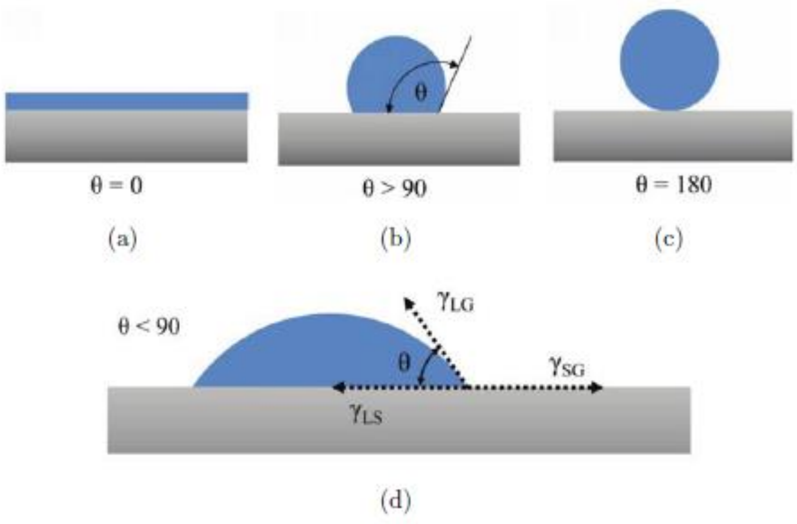

Figure 2.10: Wetting angle and spreading of a liquid (blue) on a solid surface (grey). Different wetting states: **(a)** complete wetting,**(b)** low wettability, **(c)** complete non-wetting (repulsion) and **(d)** high wettability. The unit of the contact angle θ is degrees (◦) [46]

Figure 2.10 shows a gas/liquid/solid system, where γ_{SG} is the gas/solid contact angle, γ_{LS} is liquid/solid contact angle and γ_{LG} is the gas/liquid contact angle. Complete wetting ($\theta = 0$) occurs when there is a strong solid/liquid affinity (figure 2.10 (a)). Contact angles less than 90° indicate high wettability of the liquid phase (figure 2.10 (d)), whereas contact angles larger than 90° show that the liquid phase has a low wettability (figure 2.10 (b)). Repulsion is represented by a contact angle of 180° which means that the solid/liquid affinity is very week (figure 2.10 (c)).

2.1.8 Capillarity

Capillary forces appear due to the simultaneous presence of immiscible fluids in the pore spaces i.e. partially saturated porous media. Capillary pressure P_c is the pressure difference across the interface between the wetting phase and the non-wetting phase at equilibrium.

$$P_c = \Delta P = P_{nw} - P_w \tag{2.10}$$

P_{nw} is the pressure of the non-wetting phase and P_w is the pressure of the wetting phase. The pressure of the non-wetting phase is always higher than the wetting phase pressure in a capillary. Accordingly, the capillary pressure is always positive [47]. The wetting phase is present on the concave side of the interface due to its lower pressure [48, 49]. Equation 2.11 shows the dependence of capillary pressure on the pore radius [50]:

$$P_c = \frac{2\sigma cos\theta_x}{r} \tag{2.11}$$

In the equation above, σ $[Jm^{-2}]$ is the interfacial tension, r $[m]$ is the radius of pore throat and θ_x [°] is the contact angle.

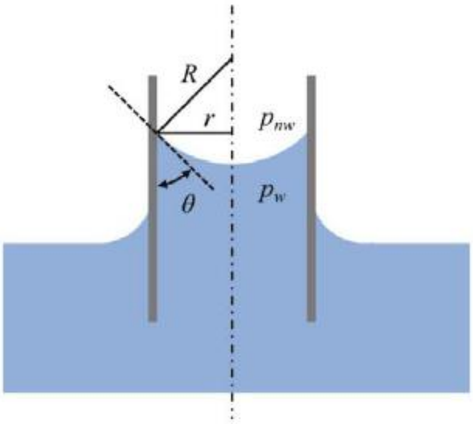

Figure 2.11: The capillary rise in the cylindrical tube of radius r [46]

As is clear by the equation 2.11, capillary pressure has an inverse relationship with the pore radius. Smaller pore radius leads to a larger capillary pressure and consequently larger capillary rise. On the other hand, the capillary rise is smaller in larger pores (figure 2.12).

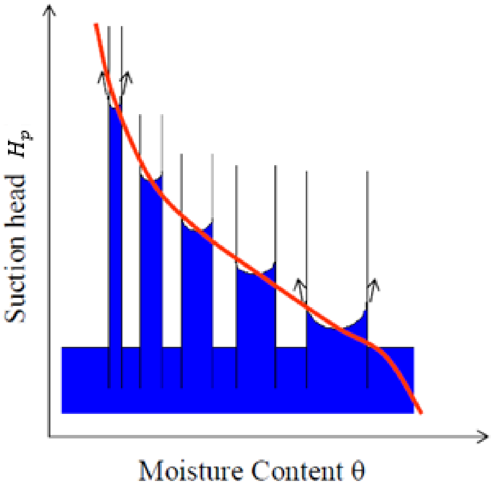

Figure 2.12: Capillary rise as a function of pore size [50]

2.1.9 Hydraulic Head

The driving force of water flow from one point to another point is the uneven distribution of mechanical energy within the water. Water always flows from a point at a higher level of mechanical energy towards a point at the lower level. The total mechanical energy (E) of water is quantified by Bernoulli equation as the sum of elastic potential, gravitational potential, and kinetic energy:

$$E = pV + mgz + \frac{1}{2}mv^2 \tag{2.12}$$

Where p is the pressure, V is the volume, m is the mass of the fluid, g is the gravitational acceleration, z is the elevation and v is the velocity. A more convenient parameter to analyze the water flow is the energy per weight of water which is called hydraulic head (H). In order to express the Bernoulli equation according to the head, all the terms in the Bernoulli equation should be divided by the weight of water (mg).

$$H = \frac{P}{\rho_w g} + z + \frac{v^2}{2g} \tag{2.13}$$

The terms on the right-hand side of the equation are respectively the pressure head, elevation head, and velocity head and ρ_w is the density of water. Groundwater moves very slowly and the velocity head does not contribute a significant amount to the hydraulic head. Thus, the velocity head can be neglected and the corresponding term disappears from the equation 2.13. The final form of the hydraulic head equation for subsurface flow can be written as below:

$$H = H_p + z \tag{2.14}$$

$$H_p = -\frac{P_c}{\rho_w g} \tag{2.15}$$

The suction head is another common term referring to the pressure head (H_p) which appears as the result of capillary forces. Equation 2.14 illustrates that the two main driving forces for water movement in the vadose zone (unsaturated porous media) are gravitational and capillary forces. It should be noted that the suction head becomes zero in the saturated zone and consequently the effect of capillarity is negligible in that zone. It is also clear that the pressure head has negative values in the unsaturated zone.

2.1.10 Storage

Storage refers to the change in the volume of water stored in an aquifer at a certain point due to a change in the pressure head. “Storage coefficient S is the volume of water added or removed from a unit volume of an aquifer for a unit change in hydraulic head.” [51]

An aquifer is the underground permeable layer of water storage. There are two kinds of aquifers (figure 2.13):

1) Confined aquifers
2) Unconfined aquifers

A confined aquifer confines the water movement into or out of the aquifer by relatively impermeable rocks. Water storage in such aquifers is due to either aquifer expansion or fluid compression [52]. The storage coefficient for confined aquifers is:

$$S = \rho g(\alpha_x + \phi\beta) \tag{2.16}$$

Where, S $[m^{-1}]$ is the storage coefficient, α_x $[ms^2kg^{-1}]$ is the compressibility coefficient of the porous medium, ϕ is the porosity and β $[ms^2kg^{-1}]$ is the fluid compressibility coefficient.

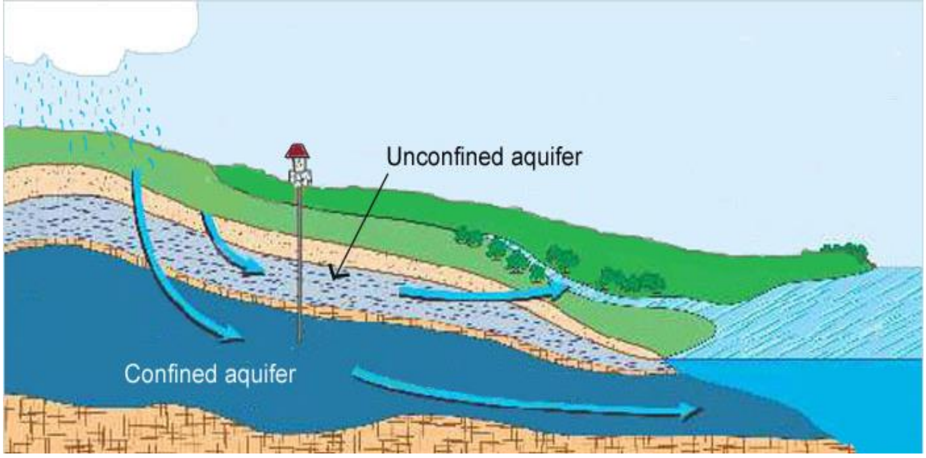

Figure 2.13: Confined and unconfined aquifers [53]

An unconfined aquifer, also named as a free aquifer, is water storage that is not limited by rocks or any other material. The upper surface of an unconfined aquifer is the water table. Water flows in all directions and is exposed to the atmosphere through pore spaces [7]. For unconfined aquifers, the storage coefficient equals the specific yield S_y which is the ratio of the volume of the water that can be drained from the medium by gravity to the total volume of the medium. Water and soil compressibility values are very smaller than specific yield and can be neglected. Therefore, the simplified formula for the storage coefficient of an unconfined aquifer is:

$$S = S_y = \theta_s - \theta_r \qquad (2.17)$$

2.1.11 Water retention curve

As discussed earlier (equation 2.14), suction head (pressure head) is a key factor for the characterization of flows in the unsaturated zone. In the unsaturated zone, the pressure head is a function of soil water content $H_p = f(\theta)$. This function is called the water retention curve. In other words, the water retention curve is the connection between the energy state of the soil and the degree of saturation by water. As illustrated by figure 2.14, a larger pressure head (energy) is needed to desaturate clay compared to sand at the same water content due to considerably higher specific surface area and capillary forces in clay. The retention function can be characterized by several parametric models (table 2.2) among which the Brooks-Corey and van-Genuchten are the most popular in terms of scientific citations [54].

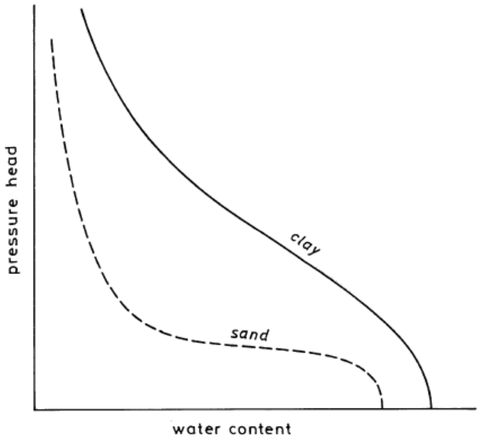

Figure 2.14: Water retention curve for sand and clay [17]

The exponential Brooks-Corey function is defined as:

$$Se = \begin{cases} \left(\dfrac{H_p}{H_b}\right)^{-\lambda} & H_p < H_b \\ 1 & H_p \geq H_b \end{cases} \qquad (2.18)$$

λ and H_b are the model parameters. λ is the pore-size distribution characteristic. Theoretically, λ varies between zero and infinity. For soils with perfectly uniform pore-size distribution it goes to infinity whereas, for soils with a wide range of pore sizes, it approaches zero. H_b is the air entry pressure which can be defined as the pressure head at which the first bubble of air enters the largest pore of the medium [7, 55]. A significant undesirable feature of the model is the existence of a discontinuity near the saturation (figure 2.15). This decreases the accuracy of the model especially for fine-textured soils where the air entry pressure value is not well-defined. However, the model shows relatively excellent results for large-textured soils [56]. In order to improve the description of the soil near the saturation, different smooth expressions were introduced by different authors [57-61]. However, these models are mathematically too complicated compared to van-Genuchten and that makes the van-Genuchten model more attractive than all of them [62]. The smooth retention curve proposed by the van-Genuchten model is [6]:

$$Se = \begin{cases} \left(\dfrac{1}{1 + \left|\alpha H_p\right|^n} \right)^m & H_p < 0 \\ 1 & H_p \geq 0 \end{cases} \tag{2.19}$$

α, m and n are the van-Genuchten parameters. For small n/m, α $[m^{-1}]$ is the inverse of air entry value whereas, for larger values of n/m, it approximately equals the inverse of the suction head at the inflection point [62]. α has larger values for large-textured soils with nearly uniform pore sizes and decreases as the texture becomes finer. m and n are independent dimensionless parameters characterizing the pore distribution. In order to have a closed-form of equations, the closure condition proposed by van-Genuchten relates *m* and *n* to each other [49].

$$m = 1 - \frac{1}{n} \tag{2.20}$$

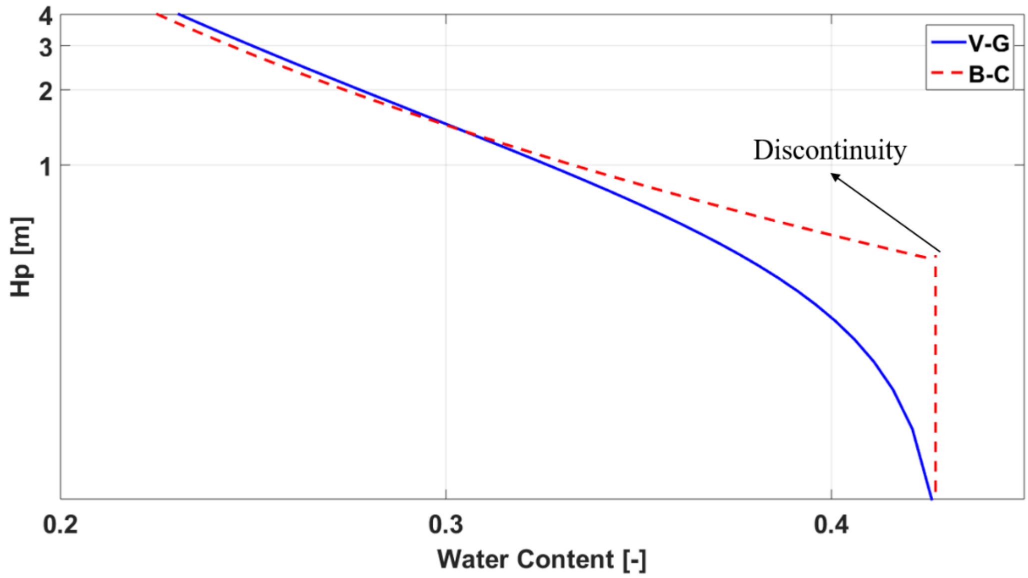

Figure 2.15: Comparison of pressure head moisture content curve (van-Genuchten solid line and Brooks-Corey dashed lines)

Table 2.2: Summary of water retention functions

Relationship	Reference
$S_e = \left(\frac{H_p}{H_b}\right)^{-\lambda}$	Brooks and Corey (1964) [7]
$S_e = \left(\frac{1}{1+\lvert\alpha H_p\rvert^n}\right)^m$	van-Genuchten (1980) [6]
$S_e = \frac{B}{(B + {H_p}^{\beta})}$	Brutsaert (1966) [63]
$S_e = \frac{\alpha}{(\alpha + (ln\lvert H_p\rvert)^{\beta})}$	Vauclin et al. (1979) [64]
$S_e = \frac{1}{[1+\exp[(H_p - H_b)/\beta]]}$	Bumb et. al. (1992) [65]

2.1.12 Saturated hydraulic conductivity

Saturated hydraulic conductivity K_s is defined as, "The volume of liquid flowing perpendicularly to a unit area of porous medium per unit time under influence of hydraulic gradient of unity." It is not an intrinsic property of the porous medium but rather depends on the fluid passing through the medium. The hydraulic conductivity and intrinsic permeability are connected via the viscosity and the density of the fluid [66]. The hydraulic conductivity is maximum under the saturation condition and is given by:

$$K_s = \frac{k \rho_w g}{\mu_w} \tag{2.21}$$

Where $K_s\ [ms^{-1}]$ is the saturated hydraulic conductivity, $k\ [m^2]$ is the permeability, $g\ [ms^{-2}]$ is the gravitational acceleration and $\rho_w\ [kg\ m^{-3}]$ and $\mu_w [Pa\ s]$ are the fluid density and viscosity respectively. The saturated hydraulic conductivity is measured in the laboratory. However, it can also be predicted by several empirical parametric models such as van-Genuchten and Brooks-Corey according to the textural class of the soil [67, 68].

Table 2.3: Typical values for saturated hydraulic conductivities [69]

Material	$\boldsymbol{K_s [cm/s]}$
Gravel	10^{-1} to 100
Clean sand	10^{-4} to 1
Silty sand	10^{-5} to 1
Silt	10^{-7} to 10^{-3}
Glacial till	10^{-10} to 10^{-4}
Clay	10^{-10} to 10^{-6}
Limestone and dolomite	10^{-7} to 1
Fractured basalt	10^{-5} to 1
Sandstone	10^{-8} to 10^{-3}
Igneous and metamorphic rock	10^{-11} to 10^{2}
Shale	10^{-14} to 10^{-8}

As is clear from table 2.3, the saturated hydraulic conductivity changes tremendously, about 12 orders of magnitude, in common soils.

2.1.13 Unsaturated hydraulic conductivity

Hydraulic conductivity is a crucial factor for the characterization of flow in unsaturated media. The existence of air as the second phase reduces the water conductivity from its maximum value at saturation (figure 2.16). The reason is simply the fact that water has less space because some pores are already filled by air. Consequently, the hydraulic conductivity in the unsaturated zone is a function of water content and it decreases as the water content decreases. A simple closed-form expression is derived from the Mualem model [70] for hydraulic conductivity in unsaturated media. According to Mualem's derivation, hydraulic conductivity is obtained from knowledge of the water retention curve and the hydraulic conductivity at saturation. The Mualem function for hydraulic conductivity is:

$$K(S_e) = K_s {S_e}^q \left[\int_0^{S_e} \frac{1}{H_p(x)} dx \,/ \int_0^1 \frac{1}{H_p(x)} dx \right]^2 \tag{2.22}$$

Where q is the model constant which indicates the pore connectivity and typically assumed to be 0.5 [71]. The hydraulic conductivity is derived by the integration of equation 2.22 while the pressure head function is provided by the water retention curve.

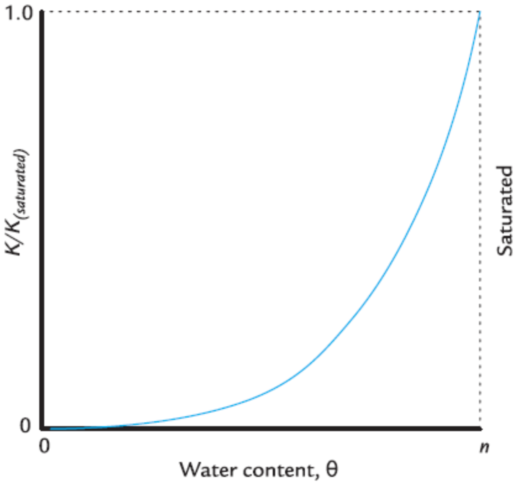

Figure 2.16: The relative conductivity as a function of water content [13]

The unsaturated hydraulic conductivity based on the van-Genuchten model:

$$K(S_e) = \begin{cases} K_s \, Se^{0.5} \left[1 - \left(1 - Se^{\frac{1}{m}} \right)^m \right]^2 & H_p < 0 \\ K_s & H_p \geq 0 \end{cases} \tag{2.23}$$

The unsaturated hydraulic conductivity based on the Brooks-Corey model:

$$K(S_e) = \begin{cases} K_s \, Se^{\frac{2}{\lambda}+3} & H_p < H_b \\ K_s & H_p \geq H_b \end{cases} \tag{2.24}$$

2.1.14 Darcy’s law

Darcy law is an expression that plays the role of momentum balance for the flow in porous media. It states that the discharge rate through porous media is directly proportional to the pressure gradient per unit length in the direction of flow [49]. Darcy’s law for one-dimensional flow (vertical direction) in the unsaturated zone is written as [11]:

$$q = -K(\nabla H_p + 1) \tag{2.25}$$

Where $q \; [ms^{-1}]$ is the Darcy flux which has the same unit as velocity but is not the real velocity. Darcy flux is an imaginary concept which predicts the average velocity of the flow under the condition that all the cross-sectional area is available for the fluid to pass through. However, in a porous medium due to the existence of grains (solid part), only a portion of the cross-section contributes to fluid flow. Darcy velocity and the real velocity of the fluid in the pores are connected via water content (in saturated media water content is replaced by the effective porosity).

$$q = v.\theta \tag{2.26}$$

The basic assumption behind the Darcy equation is that the law is just applicable for laminar flows in which the Reynolds number is less than unity ($Re < 1$) [72, 73]. As shown by equation 2.25, the pressure head distribution in the medium is needed in order to be able to solve the Darcy equation.

2.1.15 Richards equation

The transient water flow in partially saturated soil is traditionally described by the Richards equation. The Richards equation is derived by a combination of mass balance and Darcy equation and is mostly written in two forms [74]. The mass balance equation for vertical direction in the unsaturated zone is:

$$\frac{\partial \theta}{\partial t} = -\frac{\partial q}{\partial z} \tag{2.27}$$

Substitution of the Darcy flux in the mass balance (equation 2.27) gives the moisture-based form of the Richards equation:

$$\frac{\partial \theta}{\partial t} = \frac{\partial}{\partial z}\left[D(\theta)\frac{\partial \theta}{\partial z} - K\right] \tag{2.28}$$

Where $D(\theta)$ $[m^2 s^{-1}]$ is the water diffusivity and defined as:

$$D(\theta) = K\frac{dH_p}{d\theta} \tag{2.29}$$

The moisture-based form of the Richards equation is only applicable to unsaturated homogenous media and is unable to describe the saturated zone [75, 76]. To circumvent this issue, the Richards equation is rewritten in the head-based form [77]. To transfer the Richards equation to head-based form, specific moisture capacity (C_p $[m^{-1}]$) should be introduced. Specific moisture capacity is the change of water volume fraction with respect to the pressure head:

$$C_p = \frac{\partial \theta}{\partial H_p} \tag{2.30}$$

According to the relationship, C_p becomes zero at saturation. The water volume fraction is constant and equals the effective porosity at saturation. So, there is no variation in water fraction anymore.

Combination of equations 2.28, 2.29 and 2.30 provides the head-based form of Richard equation:

$$C_p\frac{\partial H_p}{\partial t} = \frac{\partial}{\partial z}\left(K\frac{\partial H_p}{\partial z} - K\right) \tag{2.31}$$

The Richards equation is based on two main assumptions. First, the soil is incompressible and the second is the ideal displacement of the air which means that there is no significant change in air pressure. So, air pressure is assumed to be constant and atmospheric [78, 79]. According to the second assumption, the governing equation is only solved for the water which means that the flow is considered as a single-phase flow. However, another term is introduced by Bear [80] on the left-hand side of the Richards equation to include the compressibility of the soil medium. The Richards equation is modified in the following form:

$$(C_p + S_e S)\frac{\partial H_p}{\partial t} = \frac{\partial}{\partial z}\left(K\frac{\partial H_p}{\partial z} - K\right) \tag{2.32}$$

The product of effective saturation and storage coefficient is the term investigating shrinkage and swelling of the medium. Equation 2.32 is used in this contribution as the modified form of the Richards equation.

As is clear by equation 2.32, the Richards equation includes both the moisture diffusion due to capillary forces ($\frac{\partial}{\partial z}\left(K\frac{\partial H_p}{\partial z}\right)$) and also the advective moisture transport induced by gravity ($\frac{\partial K}{\partial z}$). The Richards equation is strongly non-linear since all the variables in the equation except the storage coefficient are a function of the pressure head. The degree of non-linearity is even higher near the saturation where small changes in the pressure head lead to huge variations in conductivity. Then, due to the complex nature of the Richards equation, an analytical solution is not feasible except for very simplified cases [81]. The knowledge of the dependency of effective saturation, specific moisture capacity and hydraulic conductivity on pressure head, which is necessary to solve the Richards equation, is provided by the water retention curve.

Solute transport

The transport of dissolved contaminants in groundwater flow encompasses different processes among which the most important ones are: advection, diffusion, dispersion, sorption and, decay. However, the only processes that are involved in this study (advection, diffusion, dispersion) are discussed in the following.

2.1.16 Advection

Advection is the term referring to the transport of dissolved substances by the bulk motion of water. Advection is the most dominant and significant transport mechanism. The solute is carried by water with the average velocity of water through the pores. The average velocity of water is calculated by dividing the Darcy velocity by the water volume fraction.

$$v = \frac{q}{\theta} \tag{2.33}$$

The advective flux is also defined as the following:

$$q_{ad} = v.c.\theta \tag{2.34}$$

Where, c $[mol\ m^{-3}]$ is the concentration of solute and v $[ms^{-1}]$ is the pore velocity (advective transport velocity). In soils with high permeability, advection plays a dominant role and contaminants are transported mainly by advection [82].

2.1.17 Diffusion

Molecular diffusion is a mixing mechanism due to the random molecular motions. Molecular diffusion is the result of the concentration gradient. The solute diffuses from the zone with higher concentration to the zone with lower concentration until the dynamic equilibrium is established. The diffusive flux is expressed by Fick’s law of diffusion:

$$q_{dif} = -\theta . D_0 . \nabla c \qquad (2.35)$$

Where, D_0 $[m^2 s^{-1}]$ is the diffusion coefficient. For solute dissolved in water, the diffusion coefficient typically ranges from 1×10^{-9} to 2×10^{-9} [69].

2.1.18 Dispersion

In mechanical dispersion, the plume spreads along and across the direction of the main flow due to the velocity fluctuations that are caused by the heterogeneity of the porous medium (figure 2.17). The solute speed is not the same in all pores. The velocity of solute is higher in smaller pores but smaller in the larger ones. The solute velocity also changes in a pore from the center towards the edges. The mechanical dispersion occurs only when there is convection.

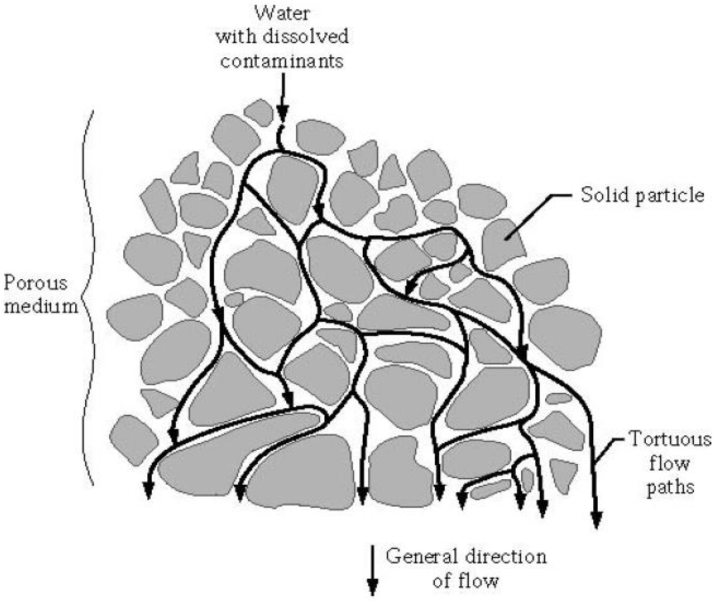

Figure 2.17: Schematic of mechanical dispersion [83]

In perfectly steady flow, the plume does not disperse transverse to the bulk flow direction and only longitudinal dispersion happens whereas, in transient flow, temporal changes lead to changes in the direction of longitudinal mixing and consequently lateral plume dispersion over the time with respect to the average flow direction [84].

Dispersion is mathematically analogous to diffusion and is expressed by Fick's law. In groundwater scientific literature, mostly mechanical dispersion and molecular diffusion are combined in a term called hydrodynamic dispersion. The longitudinal and transverse hydrodynamic dispersion coefficients are:

$$\theta D_{ii} = \alpha_L \frac{{v_i}^2}{\|v\|} + \alpha_T \frac{{v_j}^2}{\|v\|} + \theta \frac{D_o}{\tau} \tag{2.36}$$

$$\theta D_{ij} = D_{ji} = (\alpha_L - \alpha_T) \frac{v_i v_j}{\|v\|} \tag{2.37}$$

Where τ is the tortuosity factor defined as following for unsaturated porous media:

$$\tau = \theta^{-7/3}\, \theta_s^2 \tag{2.38}$$

α_L and α_T are the longitudinal and transverse dispersivities. In general, dispersivity is a function of both time and distance. However, the time dependence of the dispersivity is mostly ignored in common practice and dispersivity is considered just as a function of distance. A simple rough estimation for longitudinal dispersivity (α_L) is [85]:

$$\alpha_L = 0.1L \tag{2.39}$$

Where L is the length of the flow path. Another more accurate but also more complex formula was introduced by Neumann [86] for flow length less than 3500 m:

$$\alpha_L = 0.0175\, L^{1.46} \tag{2.40}$$

The transverse dispersivity (α_T) is typically estimated between 1/10 to 1/100 of the longitudinal dispersivity (α_L) [87].

2.1.19 Convection-Dispersion equation

The governing equation to describe the non-reactive solute transport in unsaturated porous media is a convection-dispersion equation (CDE) in the absence of source and sink terms.

$$\frac{\partial}{\partial t}(\theta c) + u.\nabla c + \nabla.(-\theta D_L \nabla c) = 0 \tag{2.41}$$

The convection-dispersion equation for solute transport in the vadose zone also considers the rate of change in the water content with time. The water volume fraction is changing with time during the flow in unsaturated media; however, this is not true in the case of saturated porous materials.

3 Air Dispersion Modeling

Plume dispersion terminology

Almost all the artificial and natural processes in the world result in some forms of air pollution. Although not all atmospheric pollutants are problematic, many forms are and make high costs for human beings with respect to lives and money.

The Royal Commission on Environmental Pollution defined pollution (in the general sense) as: “The introduction by man into the environment of substances or energy liable to cause a hazard to human health, harm to living resources and ecological systems, damage to structure or amenity or interference with legitimate use of the environment.” [88] This definition of pollution is very broad and includes many kinds of pollutants. However, the pollutants discussed in this study are compounds in the smoke plume from fire.

The random motions of a fluid caused by turbulence lead to the spreading and transfer of compounds existing in that fluid. This process is dispersion. The main factors affecting the dispersion of a pollutant plume (figure 3.1) can be categorized as following [89]:

1. Weather: wind speed, wind direction, weather temperature, atmospheric stability, the occurrence of temperature inversion, rainfall, sunshine
2. Terrain: buildings, hills, surface water and generally the landscape near the pollution source
3. Pollution source: the dimensions of the source (height and surface area), the plume exit speed, the plume exit temperature and the concentration of the pollutant in the plume
4. Pollutant’s physical and chemical properties: solubility, reactivity

Figure 3.1: Fire plume dispersion [90]

The degree of dispersion of a pollutant in the air characterizes the concentration at which the pollutant is present at different locations surrounding the pollutant source. Turbulence in the wind flow determines the degree of dispersion. Turbulence occurs mainly as a consequence of two physical phenomena. First is the heat released in the atmosphere which leads to inhomogeneous thermal distribution and consequently convective air fluxes due to buoyancy. This kind of atmospheric turbulence is called thermal turbulence. Second is the effect of the ground surface on wind flow. The degree of disturbances in the airflow due to the ground surface depends on the roughness of the surface. The turbulence induced by the surface is mechanical turbulence.

Air dispersion models

The pollutants produced by any pollution source can be transferred. Air dispersion modeling is a quantitative technique to evaluate the impact of the source of the pollution on the air quality and the fade of the pollutants. In other words, the dispersion modeling provides the possibility to predict the concentration of pollutants at every relevant location of all time which is not feasible by direct measurements. The most popular dispersion models are:

1. Gaussian Plume Model: The model states that for the steady condition (constant wind field, constant pollution source, and constant atmospheric turbulence), the time-averaged concentration profile of a pollutant in both lateral and vertical directions is Gaussian profile [9]. The model is very simple and applicable for the first order of approximation. However, the basic assumptions of the model are not very accurate because of the stochastic behavior of the atmosphere [91].

2. Stochastic Lagrangian Particle Model: The model is based on the assumption that a pollutant source produces a large number of particles that move randomly around the mean wind flow. The model calculates the trajectory of particles at each time step and accordingly the concentration of the pollutant is predicted. The model is accurate and applicable up to long distances (thousands of kilometers) but computationally expensive [89].

3. Computational Fluid Dynamics (CFD): CFD aims to solve the bulk wind flow field by the solution of the Navier-Stokes (momentum balance) equations. The direct solution of the turbulent motions of air masses is not possible. Large-eddy simulation (LES) and

Reynolds-averaged Navier-Stokes (RANS) are the main two techniques to simulate the wind turbulence in CFD. CFD provides the properties of the atmosphere and pollutants by solving the complete set of conservation equations for mass, momentum and energy including partial mass balance for different species. CFD simulation is highly reliable compared to other dispersion modeling but extremely computationally intensive. The main restriction of the Gaussian Plume Model and Stochastic Lagrangian Particle Model is that they are not applicable for the near-source region ($< 150\ m$), whereas CFD has not such a limitation and is the only possible way for calculation of dispersion near the source.

The tool to predict atmospheric dispersion in this study is computational fluid dynamics (CFD) which will be later discussed in detail in this chapter.

Meteorology for air dispersion modeling

3.1.1 Atmosphere

Figure 3.2 explains schematically the vertical structure of the atmosphere based on the temperature profile. The atmosphere can be subdivided into four layers according to the temperature variations:

1. Troposphere: The shallow layer above the earth's surface is the troposphere. The depth of the troposphere varies between 10 to 15 km. The air temperature decreases with height, which is mainly due to the pressure variation. The troposphere is the relevant layer with respect to air pollution concerns.

2. Stratosphere: The layer of 30 to 40 km depth above the troposphere is called the stratosphere. The stratosphere has nearly most of the ozone in the atmosphere. The ozone accumulated in this zone absorbs the ultraviolet lights resulting in the occurrence of a temperature inversion layer [89].

3. Mesosphere: The next 30 to 40 km above the stratosphere is the mesosphere. This layer experiences the coldest temperature in the atmosphere.

4. Thermosphere: The zone exists above the mesosphere. The temperature reaches values higher than 1000 °C in this zone.

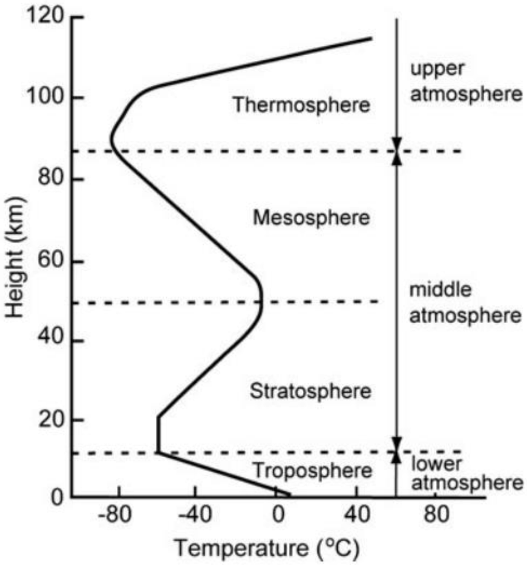

Figure 3.2: Vertical structure of the atmosphere [92]

The lower part of the troposphere is influenced by the presence of the Earth's surface. The surface creates a disturbance in the wind flow resulting in the establishment of a turbulent boundary layer above the surface. This layer is the atmospheric boundary layer (ABL) [93]. The height of the atmospheric boundary layer is also called the mixing height meaning the height of the zone, in which the degree of turbulence is sufficiently high to cause the complete mixing. The mixing height changes over a huge range daily (figure 3.3). During the day, the ground is heated by the sun and transfers the heat to the air masses next to it. The warm air next to the ground moves up due to buoyancy and an upward convective flux occurs in the boundary layer. This upward air flux increases the degree of mixing and consequently the mixing height. The mixing height is usually between 1 and 4 km during the day. The thermal distribution of the atmospheric boundary layer is different at night. The ground is colder than the atmosphere and consequently, the adjacent air layer to the surface becomes colder than the air layers at higher heights. The cold air next to the surface has no tendency to go up; hence the degree of mixing in the boundary layer is considerably lower at nights compared to day-times. The mixing height ranges from less than 100 to about 400 m at night, which is one order of magnitude less than its values in the day.

However, the surface layer is the relevant layer in the context of microscale meteorology. The surface layer is defined as the region where the wind velocity field is mainly characterized by the surface roughness. The surface layer is approximated as the first 10 % of the mixing layer [94]. The vertical fluxes of momentum and heat can be assumed constant in the surface layer.

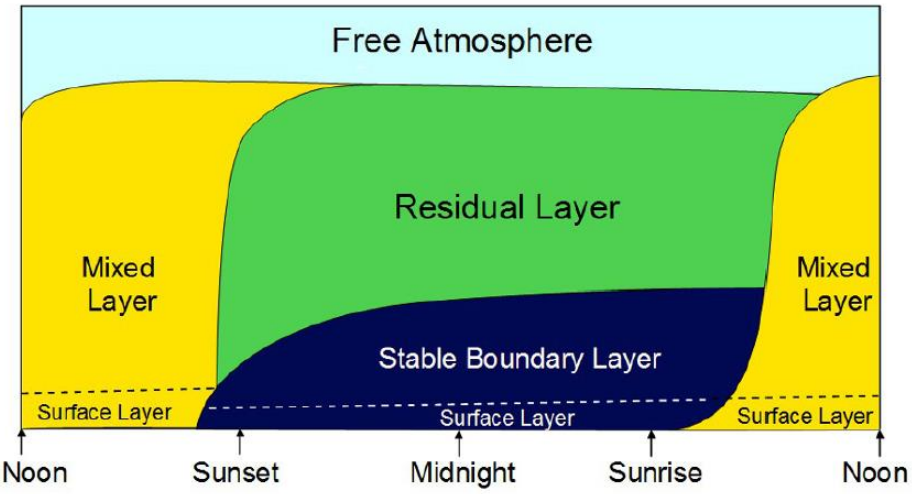

Figure 3.3: A daily cycle of the atmospheric boundary layer [95]

3.1.2 The vertical structure of the atmosphere

3.1.2.1 Pressure

The calculation of the barometric pressure change with height is the preliminary step for the understanding of the physics and properties of the atmosphere. This relationship is obtained based on the hydrostatic equation:

$$\frac{dp}{dz} = -\rho g \tag{3.1}$$

Where, $p\ [Pa]$ is the barometric pressure, $\rho\ [kgm^{-3}]$ is the air density, $z\ [m]$ is the altitude and $g\ [ms^{-2}]$ is the gravitational acceleration which is assumed constant and equals 9.80665. According to the fact that the atmosphere is remarkably shallow in comparison with Earth's diameter, the assumption of the constant gravitational acceleration in the surface layer is acceptable [88]. The air density is obtained by ideal gas law.

$$\rho = \frac{pM_{air}}{RT} \tag{3.2}$$

Here, $R\ [Jmol^{-1}K^{-1}]$ is the universal ideal gas constant and equals 8.314472, $T\ [K]$ is the absolute temperature and $M_{air}\ [kgmol^{-1}]$ is the molar mass of air which is 0.028964. Substitution of equation 3.2 into the hydrostatic equation and then integration over the height provides the mathematical relationship for the dependence of the barometric pressure on height as following:

$$p = p_0 exp\left(-\frac{M_{air}g}{RT}z\right) \tag{3.3}$$

p_0 $[Pa]$ is the pressure at the ground surface.

3.1.2.2 Temperature

The starting point to calculate the dependence of the temperature on the altitude is an adiabatic atmosphere (neutral atmosphere). It means that if a parcel of air is displaced vertically in the atmosphere without exchanging any heat, it experiences a pressure change. The temperature of the air parcel also changes as a result of changes in the pressure.

The energy conservation law should be applied to the air parcel and the energy terms should be written as a function of temperature. The conservation of energy states that the total change in the internal energy of the air parcel equals the amount of heat added to it minus the work done by it on the surrounding:

$$dU = dQ + dW \tag{3.4}$$

Where, U $[J]$ is the internal energy, Q $[J]$ is the heat and W $[J]$ is the work. For an adiabatic process, there is no heat transfer between the air parcel and the surrounding environment. So, the energy balance is rewritten as:

$$dU = dW \tag{3.5}$$

The internal energy can be expressed by the enthalpy (H) of the system:

$$U = H - pV \tag{3.6}$$

Then the differentiation of the internal energy leads to:

$$dU = dH - p\ dV - V\ dP \tag{3.7}$$

The change of enthalpy by the temperature in an isobaric process is:

$$dH = mc_{p,air}\ dT \tag{3.8}$$

Here, m $[kg]$ is the mass of the air parcel and $c_{p,air}$ $[Jkg^{-1}K^{-1}]$ is the specific heat capacity of air. As the air parcel moves in the atmosphere, the pressure change causes compression work on the parcel or expansion work by the parcel. This work is quantified as:

$$dW = -p\ dV \tag{3.9}$$

By substitution of equation 3.7 and 3.9 respectively instead of dU and dW into equation 3.7, the energy balance will be in the following form:

$$mc_{p,air}\,dT = V\,dp \tag{3.10}$$

By combining the hydrostatic equation and ideal gas law, dp can be given as a function of temperature:

$$dp = -\frac{pM_{air}g}{RT}\,dz \tag{3.11}$$

Substitution of equation 3.11 in equation 3.10 provides a relationship, which connects the temperature and height in the atmosphere:

$$\frac{dT}{dz} = -\frac{g}{c_{p,air}} \tag{3.12}$$

It should be mentioned that equation 3.12 is only applicable for dry air. However, the values of gravitational acceleration (9.80665 ms^{-2}) and specific heat (1006 $[Jkg^{-1}K^{-1}]$) are known. Hence:

$$\frac{dT}{dz} = -0.00975\ Km^{-1} \tag{3.13}$$

Equation 3.13 shows that the temperature of dry air reduces about 1 K per hundred meters change in the altitude. This ratio is called the dry adiabatic lapse rate ($\Gamma = 0.00975\ Km^{-1}$). The lapse rate is the criterion to distinguish between different atmospheric stabilities.

3.1.2.3 Potential temperature

The potential temperature Θ of a parcel of air is defined as the temperature the parcel would reach if it were to be brought to a surface at $p_0 = 100\ kPa$ in an adiabatic way. The stability of the atmosphere depends on both temperature and pressure. The potential temperature was introduced in order to combine the pressure and temperature into a single variable and discuss the stability according to that. The relationship for the potential temperature is:

$$\Theta = T\left(\frac{p_0}{p}\right)^{R/(c_{p,air}\,M_{ar})} \tag{3.14}$$

3.1.3 Stability

The assumption of the adiabatic atmosphere is not always valid. The atmospheric stability discusses the thermal stratification of the atmosphere under different circumstances. Three main atmospheric classes can be recognized according to the comparison between the actual lapse rate (Λ) and the adiabatic lapse rate (Γ).

Case 1: $\Lambda < \Gamma$ (sub-adiabatic)

This case happens when the actual or prevailing lapse rate is smaller than the adiabatic lapse rate. This means that the temperature change with the elevation in the atmosphere is lower than the adiabatic condition (figure 3.4). Under this circumstance, when a parcel of air is displaced adiabatically it has the tendency to come back to its original position because of the forces exerted by the surrounding environment upon it. For example, if a parcel of air moves up without exchanging any heat, it becomes colder than the surrounding air and tends to go down again because of the higher density. On the other hand, if a parcel of air sinks adiabatically in the subadiabatic atmosphere, it reaches a higher temperature and consequently lower density than the surrounding air and has the tendency to go up again. This kind of atmosphere is called a stable atmosphere. A lower degree of mixing is expected in a stable atmosphere.

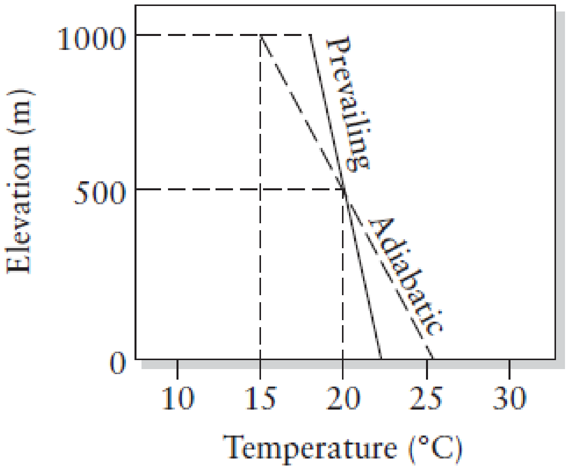

Figure 3.4: Temperature change with height in a stable atmosphere [96]

Case 2: $\Lambda > \Gamma$ (super-adiabatic)

The atmosphere is super-adiabatic when the actual lapse rate in the atmosphere is larger than the adiabatic lapse rate. This implies that the variation of the temperature with respect to height in the atmosphere is more than the adiabatic atmosphere (figure 3.5). If a parcel of air is to be displaced without any heat exchange with the surrounding in the super-adiabatic atmosphere, it has the tendency to prolong its movement. When a parcel of air moves up adiabatically, it experiences a smaller reduction of temperature. So, the parcel is hotter and lighter than the surrounding air and continues to go up. On the other hand, an air parcel becomes colder than surrounding air as it sinks adiabatically in the super-adiabatic atmosphere; hence it sinks more. This atmosphere is called an unstable atmosphere. The degree of mixing is high in such an atmosphere because of turbulence. The 'convective atmosphere' is another term for an unstable atmosphere. The term convective is used because of the upward air fluxes carrying heat from the surface to higher layers.

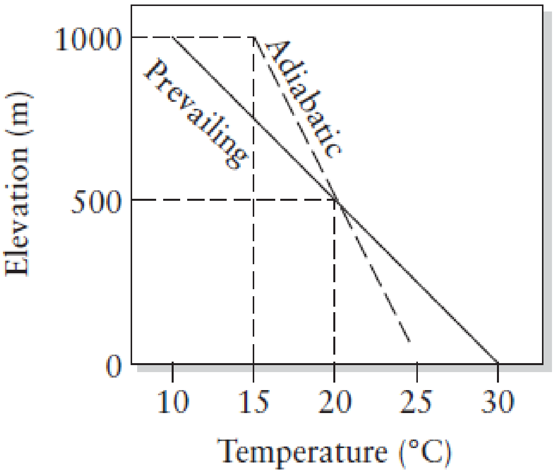

Figure 3.5: Temperature change with height in an unstable atmosphere [96]

Case 3: $\Lambda = \Gamma$ (neutral)

In a neutral atmosphere, the actual lapse rate is the same as the adiabatic lapse rate. Then, when a parcel of air moves vertically (either up or down) it stays at an identical temperature as the surrounding air (thermal equilibrium). Hence, the parcel has no tendency to move anymore.

3.1.3.1 Inversion

Inversion is an extremely stable atmosphere, in which the temperature increases with elevation. The air layer at the surface is colder than the layer that overlies it. The inversion layer behaves as a cap (wall) and prevents the upward air flux (figure 3.7). Therefore, the degree of turbulence and mixing in the atmosphere is very limited. This atmosphere has great potential to keep the pollutants near the ground.

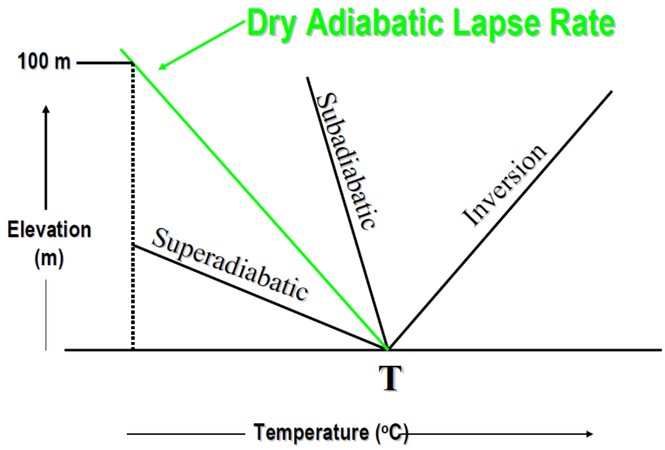

Figure 3.6: Lapse rates for different atmospheres [96]

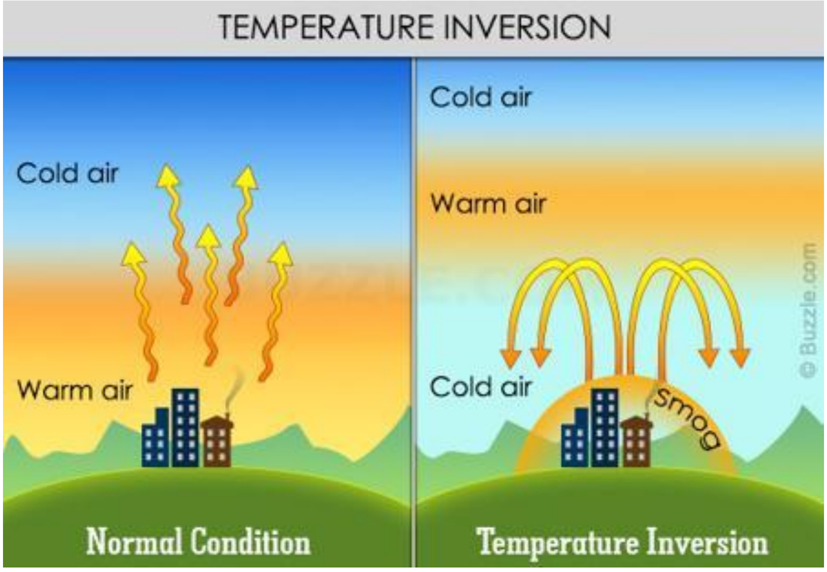

Figure 3.7: Occurrence of temperature inversion layer [97]

The temperature inversion is likely to happen under the following conditions:

1. Long nights, so the radiation emitted from the surface is larger than the radiation absorbed by the surface
2. Clear skies, which do not impede against the escape of radiation
3. Calm and stable air, so the degree of mixing is very limited

There are four types of temperature inversion:

1. A temperature inversion in a valley
2. Ground inversion (surface temperature inversion)
3. Subsidence inversion (upper surface temperature inversion)
4. Frontal inversion

The height, at which the capping layer is established, depends on the type of temperature inversion. Since this study focuses on the worst scenarios, only ground inversion will be discussed. Ground inversion results in the capping layer very close to the surface. A ground inversion is developed when the cold surface cools the adjacent layer of air to the temperature less than the overlying atmosphere. This happens mostly on clear nights when the surface temperature decreases rapidly by radiation. Ground inversion takes place most often in the higher latitudes.

3.1.3.2 Pasquill-Gifford stability classes

Pasquill-Gifford stability classification identifies six stability classes considering the influence of solar radiation and wind speed [9, 10]. On sunny days when the ground is hot because of solar energy, the lowest layers of air become warm due to heat transfer from the surface and rise. This leads to an unstable atmosphere. This effect decreases as the sunshine is reduced. As the wind speed increases, the atmospheric stability tends to the neutral atmosphere. This is mainly due to the fact that the high wind speed breaks the thermal stratification of the atmosphere. Hence, the buoyancy starts to be overwhelmed by the mechanical turbulence. At nights, the surface is cold and makes also the lowest layers of air cold. The surface air which is colder than the overlying atmosphere has no tendency to rise. This phenomenon makes the atmosphere stable. This effect is even more intense at clear nights.

The stability classes according to Pasquill-Gifford are:

A: Very unstable

B: Moderately unstable

C: Slightly unstable

D: Neutral

E: Slightly stable

F: Stable

Table 3.1: Pasquill-Gifford stability classes

	Day			**Night**	
	Incoming solar ernergy			Cloudiness	
u (ms^{-1})[a]	Strong[b]	Moderate[c]	Slight	Cloudy $(\geq 4/8)$[d]	Clear $(\leq 3/8)$[e]
<2	A	A-B[f]	B	E	F
2-3	A-B	B	C	E	F
3-5	B	B-C	C	D	E
5-6	C	C-D	D	D	D
>6	C	D	D	D	D

[a] Measured at height of 10 meter

[b] Clear summer day with sun higher than 60° above the horizon

[c] Summer day with a few broken clouds or a clear day with the sun 35-60° above the horizon

[d] Fall afternoon or cloudy summer day with the sun 15-35° above the horizon

[e] Fractional cloud cover

[f] The average dispersion values of two classes

Table 3.2: Range of temperature change for Pasquill-Gifford stability classes [88]

Stability Class	$°C/100\ m$
A	$\Delta t < -1.9$
B	$-1.9 \leq \Delta t < -1.7$
C	$-1.7 \leq \Delta t < -1.5$
D	$-1.5 \leq \Delta t < -0.5$
E	$-0.5 \leq \Delta t < 1.5$
F	$1.5 \leq \Delta t < 4$
Inversion	$4 \leq \Delta t$

3.1.3.3 Vertical wind profile

A key factor to analyze the atmosphere is the knowledge of the vertical distribution of the wind in the atmospheric boundary layer. The wind profile characterizes the degree of mixing in the atmosphere and consequently vertical momentum transfer. The wind profile is a function of height, atmospheric stability, and topology of the terrain [98]. The wind speed increases with the elevation but the degree of the dependence is strongly influenced by the atmospheric stability (figure 3.8) [99].

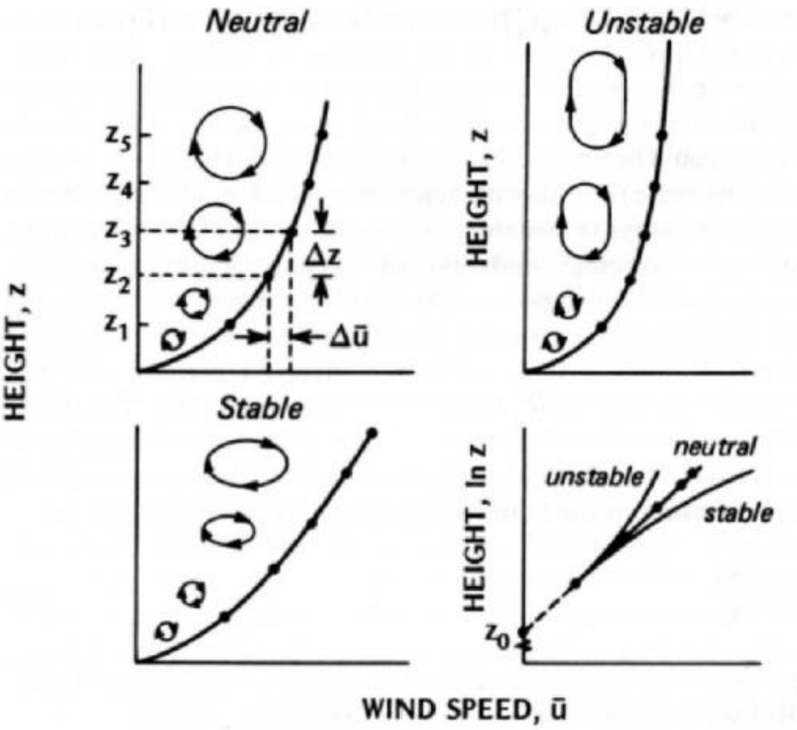

Figure 3.8: Wind profile for different atmospheres [100]

The wind profile is normally approximated by either logarithmic law or power law. The wind speed is measured at a certain height which is usually 10 m, then the wind profile is extrapolated for other heights accordingly. For engineering purposes, mostly the power-law approximation is used due to its simplicity although it has no theoretical basis [101]. The power law wind profile is given by:

$$v = v_{10}\left(\frac{z}{10}\right)^{p} \tag{3.15}$$

Where v $[ms^{-1}]$ is the wind velocity, v_{10} $[ms^{-1}]$ is the wind speed at the height of 10 m, z $[m]$ is the elevation and the exponent p is the constant determined by atmospheric stability and surface roughness. Traditionally the p exponent is assumed 1/7 for the neutral atmosphere. Moving towards the unstable zone, the value of p decreases. The p values larger than 1/7 indicate a stable atmosphere [102]. The higher the shear exponent is (stable regimes), the wind profile is more sensitive with respect to change in the elevation. This can be explained by the fact that the surface layer is not strongly coupled with the rest of the atmospheric boundary layer and the rate of the vertical momentum transfer is limited. In contrast, the lower values for the shear exponent (unstable regimes) lead to a nearly uniform vertical wind profile (figure 3.8). This is due to the substantial vertical mixing throughout the mixing layer in the unstable atmosphere. The typical values of p for the rural and urban areas under different atmospheric conditions are shown in table 3.3.

Table 3.3: Values for the exponent p in the power-law wind profile [103]

Stability Class	p for Rural Terrain	p for Urban Terrain
A	0.07	0.15
B	0.07	0.15
C	0.1	0.2
D	0.15	0.25
E	0.35	0.3
F	0.55	0.3

Surface Roughness

Surface roughness is the indicator of surface texture and is usually determined by the land cover. It plays an important role in the intensity of mechanical turbulence in the wind field near the ground. Surface roughness is characterized by the roughness length (z_0). Roughness length can be defined as the elevation from the ground at which the horizontal component of the wind vector is zero [104]. Estimation of the roughness length is controversial; however, Wieringa (1993) [105] provides a comprehensive review over the surface roughness and offered well-validated roughness length values for various landscapes.

Table 3.4: Classification of surface roughness length for different landscapes [105]

Class	Roughness length	Landscape features
1. Sea	0.0002	open water, tidal flat, snow-covered terrain
2. Smooth	0.005	featureless land, ice
3. Open	0.03	flat terrain with grass or very low vegetation, airport runway
4. Roughly open	0.1	cultivated area, low crops, obstacles of height H separated by at least 20 H
5. Rough	0.25	open landscape, scattered shelter belts, obstacles separated by 15 H or so
6. Very rough	0.5	landscape with bushes, young dense forest etc. separated by 10 H or so
7. Closed	1	open spaces comparable with H, e.g. mature forest, low-rise built-up area
8. Chaotic	Over 2	irregular distribution of large elements, e.g. city center, large forest with clearings

Computational Fluid Dynamics (CFD)

Fluid flows are described by a set of partial differential equations, which represent conservation laws for mass, momentum, and energy. The analytical solution for these governing equations is not possible except for very simple cases. Computational fluid dynamics (CFD) is the numerical calculation of the flow equations. In other words, CFD is the technique of converting these partial differential conservation equations into a set of algebraic equations.

However, CFD is not completely reliable and there are always some errors and uncertainties. The simulation errors come from two sources: 1) the physical assumptions and simplifications, 2) the mathematical based errors due to discretization and rounding.

3.1.4 Governing equations

The scope of this study is the investigation of the evolution of the hot fire plume under different atmospheric stability conditions. In this contribution, the plume is considered a hot gaseous phase including different components. According to the nature of the problem, the following considerations should be noticed:

- The simulation is single-phase flow with species transport
- The flow is compressible
- The buoyancy is significant

The species transport equation for each component of the gaseous mixture is:

$$\frac{\partial}{\partial t}(\rho Y_i) + \nabla.(\rho \boldsymbol{v} Y_i) = -\nabla.\vec{J}_i + S_i \tag{3.16}$$

Where, Y_i is the mass fraction of the species i, S_i is the source term for species i and $\vec{J}_i$ is the diffusion flux of species i which appears because of concentration and temperature gradients. For a mixture of N components, an equation of this form is solved for N-1 components and the mass fraction of the N^{th} species is calculated as one minus the sum of the computed N-1 mass fractions. This is due to the fact that the sum of the mass fractions of all species is unity ($\sum Y_i = 1$). In ANSYS FLUENT the mass diffusion, due to the concentration gradient, is described by the dilute approximation (Fick's law). The mass diffusion flux in a turbulent flow is calculated by:

$$\bar{J}_i = -\left(\rho D_{i,m} + \frac{\mu_t}{Sc_t}\right)\nabla Y_i - D_{T,i}\frac{\nabla T}{T} \tag{3.17}$$

Here, $D_{i,m}$ and $D_{T,i}$ are the mass and thermal diffusion coefficients respectively, μ_t is the turbulent viscosity and Sc_t is the turbulent Schmidt number. The default value for turbulent Schmidt number in ANSYS FLUENT is 0.7.

The momentum balance equations for a compressible flow are written as:

$$\frac{\partial(\rho u)}{\partial t} + div(\rho u \boldsymbol{v}) = -\frac{\partial P}{\partial x} + div(\mu\, grad\, u) \tag{3.18}$$

$$\frac{\partial(\rho v)}{\partial t} + div(\rho v \boldsymbol{v}) = -\frac{\partial P}{\partial y} + div(\mu\, grad\, v) \tag{3.19}$$

$$\frac{\partial(\rho w)}{\partial t} + div(\rho w \boldsymbol{v}) = -\frac{\partial P}{\partial z} + div(\mu\ grad\ w) + F_g \tag{3.20}$$

The momentum balance states that the rate of change in the momentum of a fluid particle equals the sum of the whole forces acting on that. The first term on the right-hand side of the momentum equation indicates the pressure forces and the second term refers to viscous forces. The z-component of the momentum equation includes an extra term (F_g) on the right-hand side which appears due to the existence of the gravitational body force. The buoyancy term is present when the density variation in the flow is not negligible. The buoyancy force is defined as:

$$F_g = (\rho - \rho_0)g \approx -\rho_0\beta(T - T_0)g \tag{3.21}$$

The Boussinesq approximation is used to replace the density by temperature in the buoyancy term. The Boussinesq approximation is given by:

$$\rho = \rho_0(1 - \beta\Delta T) \tag{3.22}$$

Where β is the thermal expansion coefficient:

$$\beta = -\frac{1}{\rho}\left(\frac{\partial\rho}{\partial T}\right)_p \tag{3.23}$$

The energy balance in term of the internal thermal energy for a fluid particle is written:

$$\frac{\partial(\rho i)}{\partial t} + div(\rho i \boldsymbol{v}) = -p\ div\ \boldsymbol{v} + div(k\ grad\ T) + \Phi + S_i \tag{3.24}$$

The term (Φ) on the right-hand side of the energy balance is called the dissipation function and refers to the effect of viscous stresses on the internal energy.

For incompressible flows, the motion of the fluid can be described only by mass balance and momentum equations. In the absence of heat transfer, there is no coupling between flow equations and the energy balance. However, the situation is different for compressible flows. The mass and momentum equations are linked to the energy balance because of the dependence of density on the pressure and temperature. In order to solve the momentum equations, the knowledge about the temperature field is necessary. Also, the buoyancy term on the right-hand side of the z-component of the momentum balance is approximated as a function of temperature. So, there is a strong connection between the mass, momentum and energy equations. The linkage is provided by the equations of state. The thermodynamic state of each substance at equilibrium is characterized by two state variables. The other thermodynamic variables can be obtained from the state variables via the equations of state. The equations of state for an ideal gas are defined as:

$$p = \rho RT \quad and \quad i = c_v T \tag{3.25}$$

Turbulence

The motion of the air near the ground surface is mostly turbulent. In general, when a fluid of low viscosity flows over a rigid surface, it is susceptible to be disturbed by the surface easily. So, the wind field near the surface can be rarely considered as a laminar flow where the fluid molecules follow a regular pattern. In the turbulent boundary layer, the fluid motion is totally irregular and stochastic and changes randomly with time (figure 3.9). The random nature of the turbulent flows is represented by the generation and disappearance of the turbulent eddies, which can vary over a huge range of length scales. Direct numerical simulation of the turbulence in the atmosphere (solving the whole eddies of all sizes in the atmosphere) is nearly impossible due to extremely high computational expenses. Speziale (1991) [106] stated that the direct solution of turbulence even in a very simple pipe flow requires computers ten million times faster than the current ones. This means that some modeling techniques should be applied to investigate turbulence.

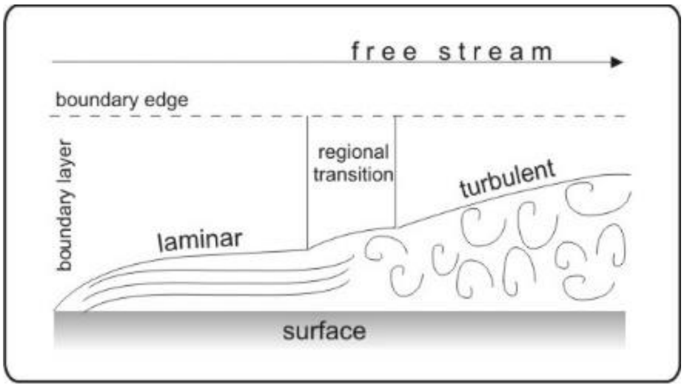

Figure 3.9: Laminar and turbulent boundary layer [107]

Two main modeling methods dealing with turbulence are called Reynolds-Averaged Navier-Stokes (RANS) and Large Eddy Simulation (LES). The RANS method removes the turbulence features of the velocity field and parameterizes the fluctuating component of velocity in terms of the mean velocity. RANS method assumes that the fluctuations of velocity are negligible compared to mean bulk velocity. The second way of modeling turbulence (LES) is more accurate but also computationally expensive. The LES method is also based on averaging but not for the whole flow field. According to the physics of the phenomenon, a critical length scale is selected. The turbulence eddies larger than the critical size are solved directly, whereas eddies smaller than the critical length scale are parameterized by averaging.

In practice, the Reynolds-Averaged Navier-Stokes (RANS) method is the most popular technique dealing with the simulation of turbulence. Although the RANS model only provides information about the mean properties of the flow, it is still adequately satisfactory for many engineering purposes [108]. According to Reynolds decomposition theory, the velocity can be split into two components namely, mean value and fluctuating component (figure 3.10).

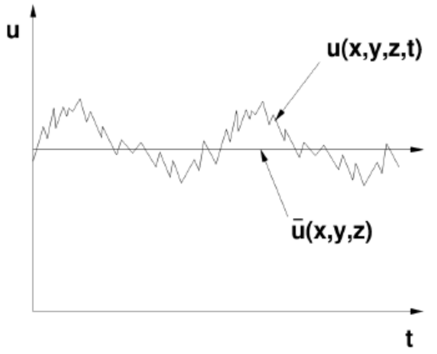

Figure 3.10: Turbulent velocity at a point [109]

As is clear in figure 3.10:

$$u = \bar{u} + u' \tag{3.26}$$

Where $\bar{u}$ is the mean component of the velocity and u' is the fluctuating component. For both mean and fluctuating components the following Reynolds averaging rules must be kept:

$$\overline{u'} = 0, \tag{3.27}$$

$$\bar{\bar{u}} = \bar{u} \tag{3.28}$$

$$\overline{\bar{f}\bar{g}} = \bar{f}\bar{g} \tag{3.29}$$

The mean velocity is calculated by the integration of the velocity profile over a time interval (Δt).

$$\bar{u} = \frac{1}{\Delta t} \int_{t-\Delta t/2}^{t+\Delta t/2} u \, dt \tag{3.30}$$

The selection of the time interval is not straightforward. It should be long enough to be able to capture a sufficient amount of fluctuations. On the other hand, a very long time interval might include substantial changes in the velocity and a single mean value cannot be an accurate representation of the velocity over the interval.

The turbulence in a flow field is mostly described by two quantities, the turbulence intensity and the turbulence kinetic energy per unit mass. The turbulence kinetic energy is given by:

$$k_{tur} = \frac{1}{2}\left(\overline{u'^2} + \overline{v'^2} + \overline{w'^2}\right) \tag{3.31}$$

And turbulence intensity is defined as:

$$T_i = \frac{\sqrt{\frac{2}{3}k}}{\bar{V}} \tag{3.32}$$

Where $\boldsymbol{v}$ is the mean total velocity of the fluid:

$$\boldsymbol{v} = \sqrt{\bar{u}^2 + \bar{v}^2 + \bar{w}^2} \tag{3.33}$$

In order to derive the time-averaged equations for a turbulent flow, the Reynolds averaging rules should be applied to all the variables in the momentum balance. The mean momentum equations after time averaging, also called Reynolds equations, for a compressible flow are given as follows:

$$\frac{\partial(\rho\bar{u})}{\partial t} + div(\rho\bar{u}\boldsymbol{v}) = -\frac{\partial P}{\partial x} + div(\mu \, grad \, \bar{u}) + \left[-\frac{\partial\left(\rho\overline{u'^2}\right)}{\partial x} - \frac{\partial(\rho\overline{u'v'})}{\partial y} - \frac{\partial(\rho\overline{u'w'})}{\partial z}\right] + S_x \tag{3.34}$$

$$\frac{\partial(\rho\bar{v})}{\partial t} + div(\rho\bar{v}\boldsymbol{v}) = -\frac{\partial P}{\partial y} + div(\mu \, grad \, \bar{v}) + \left[-\frac{\partial(\rho\overline{v'u'})}{\partial x} - \frac{\partial\left(\rho\overline{v'^2}\right)}{\partial y} - \frac{\partial(\rho\overline{v'w'})}{\partial z}\right] + S_y \tag{3.35}$$

$$\frac{\partial(\rho\overline{w})}{\partial t}+div(\rho\overline{w}\boldsymbol{v})=-\frac{\partial P}{\partial z}+div(\mu\, grad\,\overline{w})+\left[-\frac{\partial(\rho\overline{w'u'})}{\partial x}-\frac{\partial(\rho\overline{v'w'})}{\partial y}-\frac{\partial\left(\rho\overline{w'^2}\right)}{\partial z}\right]+S_z \quad (3.36)$$

Momentum equations above show that the Reynolds averaging method introduces six additional terms on the right-hand side of the momentum balance equations.

$$-\rho\overline{u'^2}, -\rho\overline{v'^2}, -\rho\overline{w'^2}, -\rho\overline{u'v'}, -\rho\overline{u'w'}, -\rho\overline{v'w'}$$

The new terms are dependent on the velocity fluctuations but not on viscosity. They are called Reynold stresses and indicate the momentum transport via velocity fluctuations. The normal Reynolds stresses ($-\rho\overline{u'^2}, -\rho\overline{v'^2}, -\rho\overline{w'^2}$) cannot be zero since the square of a non-zero value (the fluctuating component of the velocity) is never zero, whereas the shear Reynolds stresses might be zero depending on the flow condition and the degree of turbulence. However, in fully turbulent flows, the turbulent shear stresses are substantially larger compared to viscous stresses, meaning the turbulence has the dominant contribution to the vertical momentum transport and the vertical transport of momentum by viscosity is negligible. In the end, it should be noticed that there is no mathematical description for Reynolds stresses which can be derived from the first principals. In this regard, turbulence closure conditions are needed to circumvent the problem. These closure conditions are called turbulence models.

Although the above discussion is about the momentum transport in the flow because of turbulence, this procedure can be applied to any other quantity. This means that in turbulent flow, turbulence has a contribution to the transport of any quantity. The time-averaged transport equation for any the arbitrary scalar φ is given by:

$$\frac{\partial\varphi}{\partial t}+div(\bar{\varphi}\boldsymbol{v})=div\left(\Gamma_\varphi^*\, grad\,\bar{\varphi}\right)+\left[-\frac{\partial\overline{u'\varphi'}}{\partial x}-\frac{\partial\overline{v'\varphi'}}{\partial y}-\frac{\partial\overline{w'\varphi'}}{\partial z}\right]+S_\varphi \quad (3.37)$$

As shown by equation 3.37, the transport terms resulting from turbulence appear on the right-hand side of the equation. Similar to the time-averaged momentum equations, there is no expression to estimate the turbulent transport terms and turbulence models are needed to close the set of equations and connect the turbulent transport terms to the bulk mean properties.

The main classical turbulence models for time-averaged governing equations are classified as:

1. Zero equation model: mixing length model
2. Two-equation model: $k-\varepsilon$ model

3. Reynolds stress equation model
4. Algebraic stress model

Up to date, the $k-\varepsilon$ model is the most widely accepted turbulence model among the CFD users in industrial applications [110]. The $k-\varepsilon$ model makes a compromise between accuracy and computational costs. The $k-\varepsilon$ model is based on the assumption of analogy between the viscous stresses and Reynolds stresses, meaning the Reynolds stresses are mathematically described in the same way as the viscous stresses. The model introduces the turbulence (eddy) viscosity to connect the Reynolds stresses to the rate of changes in the mean velocity field. The standard $k-\varepsilon$ model [111] describes the turbulence in the flow by introducing two additional transport equations (partial differential equations) for the production of the turbulence kinetic energy (k) and the dissipation of the turbulence kinetic energy (ε).

The turbulent viscosity (μ_t) is:

$$\mu_t = \rho C_\mu \frac{k^2}{\varepsilon} \tag{3.38}$$

The governing equation for the production of turbulence kinetic energy:

$$\frac{\partial(\rho k)}{\partial t} + div(\rho k \boldsymbol{v}) = div\left[\left(\mu + \frac{\mu_t}{\sigma_k}\right) grad\ k\right] + G_k + G_b - \rho\varepsilon + S_k \tag{3.39}$$

The governing equation for the dissipation of the turbulence kinetic energy:

$$\frac{\partial(\rho \varepsilon)}{\partial t} + div(\rho \varepsilon \boldsymbol{v}) = div\left[\left(\mu + \frac{\mu_t}{\sigma_\varepsilon}\right) grad\ \varepsilon\right] + C_{1\varepsilon}\frac{\varepsilon}{k}(G_k + C_{3\varepsilon}G_b) - C_{2\varepsilon}\rho\frac{\varepsilon^2}{k} + S_\varepsilon \tag{3.40}$$

Where, G_k indicates the production of turbulence kinetic energy due to the mean velocity gradient, G_b refers to the turbulence kinetic energy because of buoyancy and S_k and S_ε are the source terms.

$C_\mu, C_{1\varepsilon}, C_{2\varepsilon}, \sigma_k$, and σ_ε are the model constants and for a wide range of turbulent flows can have the following default values [112]:

$$C_\mu = 0.09, \qquad C_{1\varepsilon} = 1.44, \qquad C_{2\varepsilon} = 1.92, \qquad \sigma_k = 1.0, \qquad \sigma_\varepsilon = 1.3 \tag{3.41}$$

4 Small scale experiments

This set of experiments was performed by the Aerius team during the Aerius project in 2016 [142]. The aim was to provide a comparison between the fire suppression efficiencies of a class A compressed air foam (CAF) and water (the traditional and most common extinguisher) for class A fire (fire from burning of solid combustible materials). In this regard, six different small scale fire experiments (rated less than 1 MW) were accomplished. The compressed air foam had a 1 % foam solution and was produced by a mini-CAF-system consisting of pressure vessel, control valve and connection for a nozzle. The operating pressure was adjusted in a way (6 bar) that the foam expansion ratio was 7. The influence of the mass flow rate of the extinguishing agent on the fire suppression process was also investigated via the application of three different flow rates of 1.05, 1.5 and 1.8 kg/s for each agent. The summary of the experimental setup is shown in table 4.1. In order to minimize the uncertainties and effects of external stochastic parameters such as wind, all the experiments were conducted in an indoor environment. Based on the findings of Melcher, T., et al [113], substantial discrepancies might occur in fire tests even under identical conditions due to stochastic behavior of fire. In order to reduce the experimental uncertainties, each test was repeated and the mean value of both tests was used.

Table 4.1: The summary of 6 different fire scenarios

Tests	Extinguisher	Burning material	Mass flow rate
Test 1	CAF	Wood & Plastic	1.8 kg/min
Test 2	CAF	Wood & Plastic	1.5 kg/min
Test 3	CAF	Wood & Plastic	1.05 kg/min
Test 4	Water	Wood & Plastic	1.8 kg/min
Test 5	Water	Wood & Plastic	1.5 kg/min
Test 6	Water	Wood & Plastic	1.05 kg/min

Burning material

Class A fire is the fire from solid combustible materials. In reality, the burning material is never just one substance; different materials take part as fuel in open fires such as land fires, municipal waste fires, construction materials fires, etc. A mixed crib is considered in this contribution as the representative of real burning materials. The mixed crib was the combination of the 8A standard wood crib plus plastic round rods of PP, PU, PVC, and PE. According to DIN EN 3 [114], 8A wood crib consists of 35 wooden sticks of 80 cm length and 56 sticks with a length of 50 cm. The wooden rods are stacked in 14 layers on a metal frame with a height of 250 mm, a width of 900 mm and the same length as that of the test object (800 mm for A8 wood crib). In odd layers, there are 5 longer bars (80 cm) and even layers have 8 shorter sticks (50 cm). All the wooden sticks have a square cross-section with a side length of 4 cm (figure 4.1). The wood using in this purpose was pine wood with moisture fraction varying between 10 to 15 %. The crib's weight was approximately 55 kg. Then, plastic rods were added to the A8 crib in a way that the mass fractions of PP, PU, PVC, PE and wood in the final mixed crib were respectively 0.05, 0.067, 0.074, 0.055 and 0.75. The popularity of standard wood cribs for fire tests is because of their relative ability to provide reproducible results. A8 standard wood crib is shown from both short and long sides by figures 4.1 and 4.2. Dimensions in the following figures are in mm.

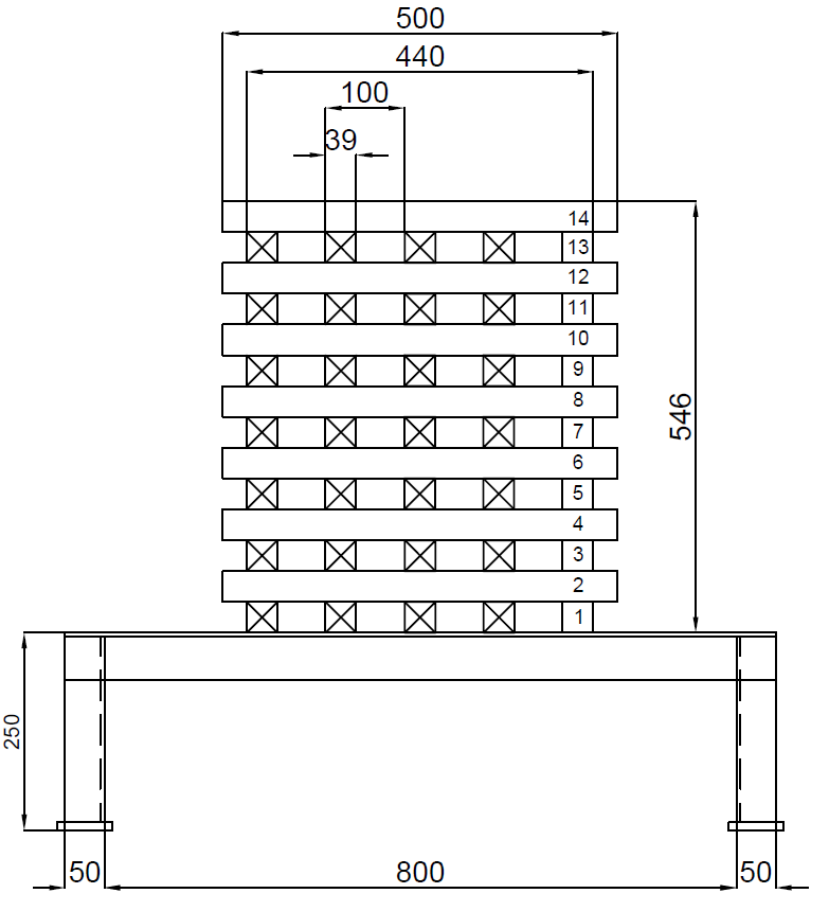

Figure 4.1: The short side of A8 wood crib

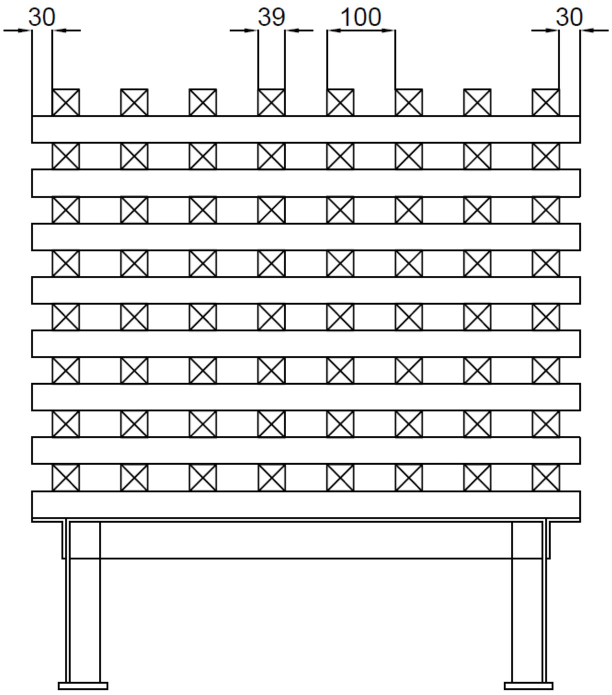

Figure 4.2: The long side of A8 wood crib

Experimental procedure

To submit the amount of extinguishing agent reproducible in flow rate, time and dislocation, a semi-automated extinguishing system was designed. As is clear by figure 4.3, the mixed crib was placed on a turntable and ignited by n-Heptane for 2 minutes to reach the fully-developed stage. Then, the fire was allowed to continue for 6 minutes to establish the steady fire mode where the mass loss rate of the fuel and heat flux released from the fire are approximately constant with time. Then, extinguishment started. With the start of extinguishment, the turntable began to rotate with a circular velocity of 2 rpm. The extinguishing agent was applied by the experimental apparatus shown in figure 4.3, where a nozzle was installed on the swivel arm moving vertically with rotational speed 10 rpm. The angle through which the swivel arm was moving had been calculated in a way that gave the possibility to the extinguishing agent to cover all areas of the burning fuel. The numbers 1, 2, and 3 in figure 4.3 indicate the automated system designed, the nozzle installed at the top of the swivel arm and the turntable respectively.

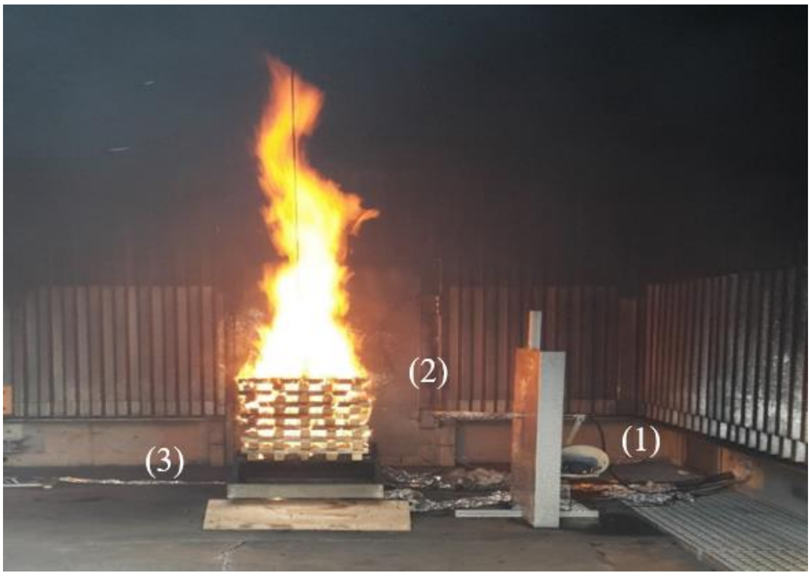

Figure 4.3: Designed automated system, turntable and extinguishing nozzle

Extinguishing effectiveness

The reduction in heat flux density was considered as the basis for the evaluation of the extinguishment effectiveness. The radiative heat flux released from the fire was recorded by two different sensors during the fire test. The sensors were located at different positions next to the fire. The distribution of heat around the fire is not homogenous. This is due to the random and stochastic nature of fire. Hence, heat flux density should be measured at more than one measuring point to circumvent the uncertainties due to local measurements. More measuring points lead to a more reliable and accurate investigation. Figure 4.4 illustrates schematically the experimental field and locations of sensors. Both sensors were installed at a height of 70 cm from the bottom of the turntable.

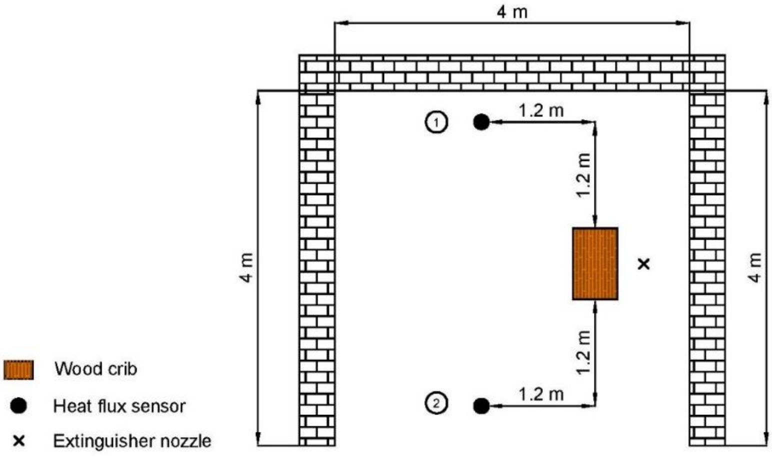

Figure 4.4: Schematic representation of the experimental field, top view

Discussions

As mentioned before, the relative reduction in heat flux density was used as the criterion to quantify the efficiency of the extinguishing agent to suppress and control the fire. Figure 4.5 shows the heat flux over time as measured by each sensor for test 1. The heat flux curves for other tests also have the same trend.

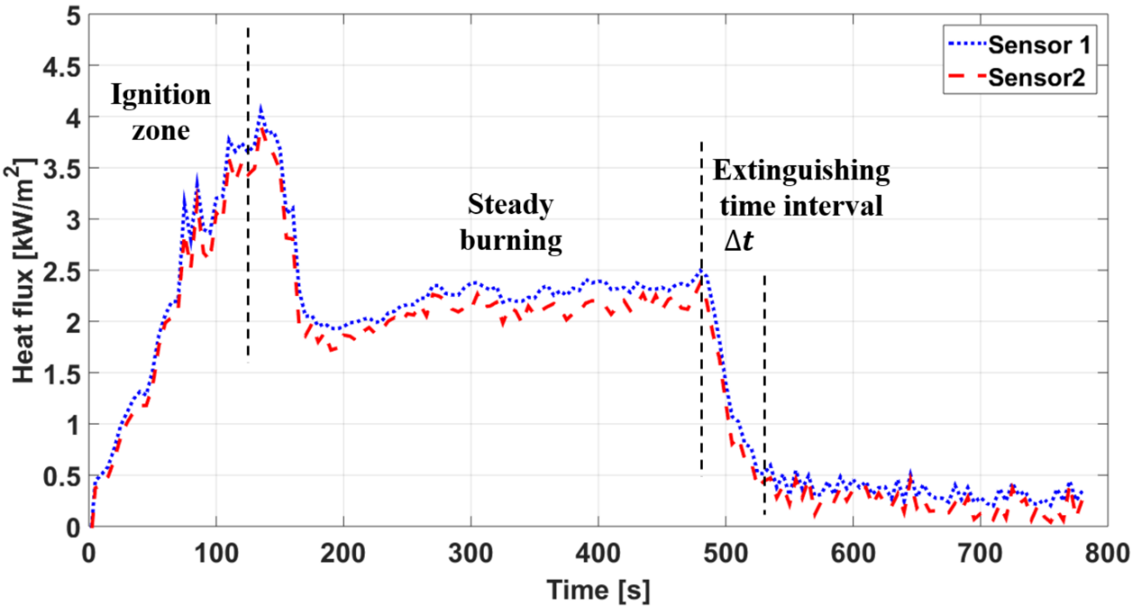

Figure 4.5: Heat flux density curves measured by each sensor for test 1

The heat flux curve increases substantially in the first two minutes because of the burning of n-Heptane. Then, it remains constant for the next six minutes and decreases with the beginning of the extinguishment process. The heat flux decreases substantially in the first 50 s of the extinguishment. Thus, this period (first 50 s) was selected as the time interval of investigation in this study meaning the amount of decrease of the heat flux in these seconds is the indicator of the fire-fighting effectiveness.

Although increasing the number of sensors leads in more reliable results but the curves from both sensors are relatively the same. This implies that two sensors are reasonably sufficient for this experimental setup and the statement based on measurements of two sensors is acceptable.

4.1.1 Fire suppression effectiveness

In the following, the calculated values of the heat flux reduction ($\Delta Q_{\Delta t}$) for each sensor during the extinguishing time interval for each extinguishing agent at different flow rates are discussed (figure 4.6).

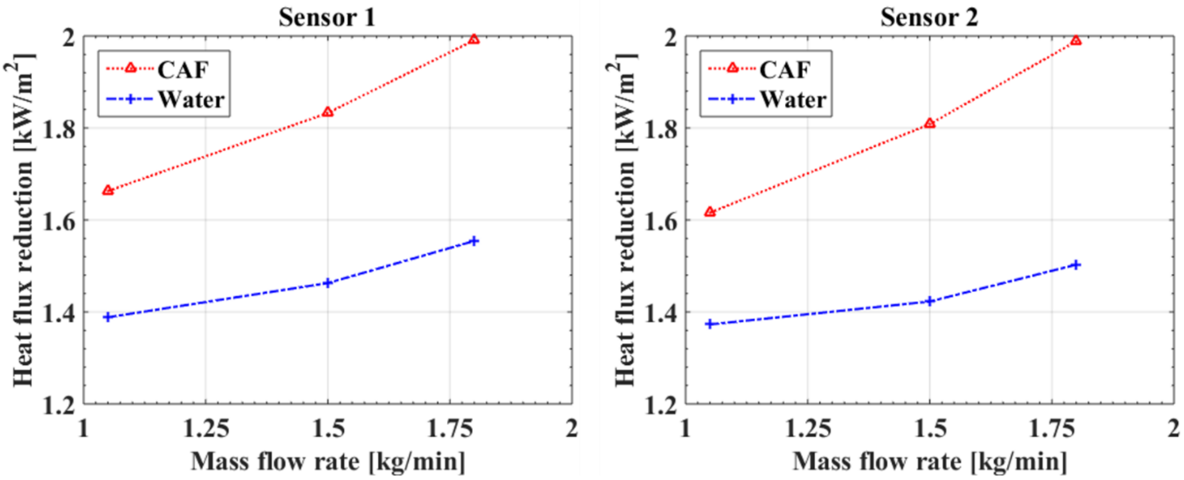

Figure 4.6: Radiative heat flux reduction measured by each sensor at different mass flow rates for tests 1 to 6

As depicted by figure 4.6, CAF shows an absolute prominence compared to water. This is mainly due to the existence of plastics in the fuel. During the fire, the plastics melted. Melting of plastics led to pool-fire-like behavior in the turntable under the fire load. Pool fire is the fire of flammable liquids in confined geometry. When it comes to the extinguishment of pool fires, water is not the best extinguishing agent. Water jet stirs up the surface of the burning liquid and lifts up burning droplets. Furthermore, it should be also taken into account that water possesses a higher density than most of the liquid fuel and upon its application, it has the tendency to sink down to the bottom. Hence, the liquid fuel can float on the water and continue burning; there is also the risk of spreading the floating burning fuel and enlarging the fire. On the contrary, CAF is an excellent agent which can address the shortcomings of water in the case of pool-fire-like fires. CAF behaves like a blanket, establishing a barrier over the burning surface, and deprives the burning material from oxygen. It is also a noticeable point that there are a lot of hydrophobic burning materials and water is not able to penetrate through them completely, so water runs away. Here, the plastics incorporated in the mixed cribs were hydrophobic and this is another important reason for the superior performance of CAF.

There are still slight differences between the data from different measuring points (figure 4.6). This reveals the fact that even in the absence of wind (indoor environment) as an important disturbing factor, the heat release from the fire is still inhomogeneous because of the stochastic nature of fire.

Based on the mean values obtained from averaging data recorded by both sensors (values from figure 4.6), the superiority of CAF over water is discussed quantitatively in table 4.2. The mathematical expression which was used in this study to calculate the fire suppression superiority of CAF over water (SCW) is:

$$SCW = \frac{\Delta Q_{CAF,\Delta t} - \Delta Q_{water,\Delta t}}{\Delta Q_{water,\Delta t}} \tag{4.1}$$

Here, $\Delta Q_{CAF,\Delta t}$ and $\Delta Q_{water,\Delta t}$ are the reduction in the heat flux density during the extinguishing time interval for CAF and water respectively.

Table 4.2: Prominence of CAF over water at different flow rates

Mass flow rate of agent	Superiority of CAF over water
1.05	18.7 %
1.5	26.1 %
1.8	30 %

As both figure 4.6 and table 4.2 express, with increasing the mass flow rate of the extinguishing agent upon its application, the prominence of CAF over water becomes more significant. The main functional advantage of CAF technology is the ability of CAF to cover the fuel, making a barrier over the burning surface. For this purpose, the mass flow rate of CAF during extinguishment should be sufficiently high to let the CAF establish a blanket over the fuel. Otherwise, CAF is not able to show its main beneficial function. However, this study assumes 30 % of higher fire-fighting efficiency for CAF compared to water.

4.1.2 Mass loss rate

A crucial factor needed to be obtained from the experiments was the burning rate of the burning material per unit area. The mass flux was needed to estimate the rate of production of smoke from the fire and use it as a boundary condition for the numerical simulation. The mass loss of the crib during the test was measured. Figure 4.7 depicts the mass loss rate of the burning material with time. The mass-loss rate was measured from the beginning until the start of the extinguishment process ($t = 480\ s$).

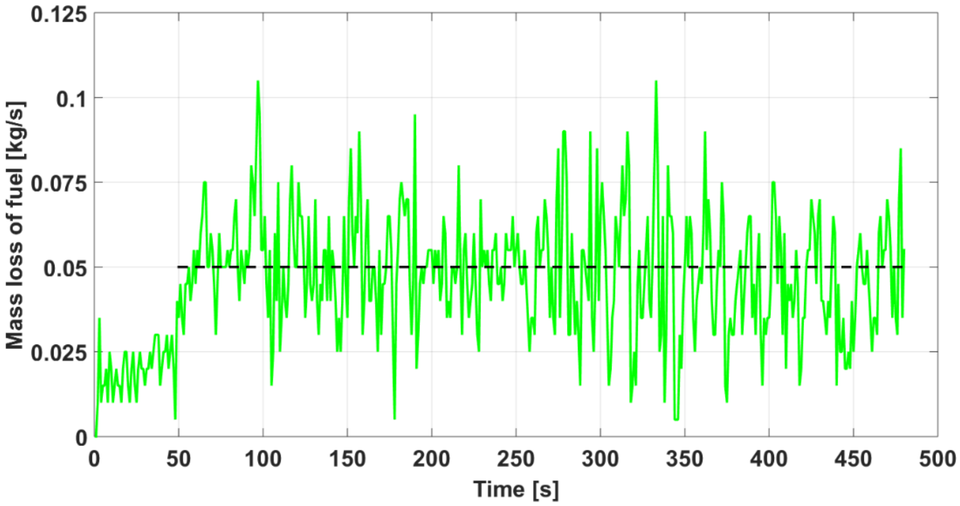

Figure 4.7: Mass loss rate of the mixed crib

The burning rate went up at the beginning of the test and then, fluctuated around the constant value of 0.05. Thus, the constant mass-loss rate of 0.05 kg/s was assumed as the burning rate of the crib during the steady-burning stage of the fire. However, the mass-loss rate per unit area of the fuel was required for numerical simulation. Accordingly, the total surface area of the mixed crib that gets involved in the fire was needed. A rough approximation for our case (A8 wood crib plus plastic rods) was done by hand and the active area of the crib participating in the fire is about 6.31 m^2. The mass loss per unit surface area is calculated via:

$$m''_{fuel} = \frac{\dot{m}_{fuel}}{A_t} = \frac{0.05\ {}^{kg}/_{s}}{6.31\ m^2} = 0.0079 \approx 0.008\ \frac{kg}{m^2.s} \qquad (4.2)$$

Outcomes of experiments

The main outcomes used in this study from these experiments can be summarized as follows:

- **Burning rate per unit surface area:**
  The burning rate of the fuel per unit area was needed to predict the approximate rate of production of smoke from the fire. The smoke was considered as the product of the combustion reaction of fuel with available air. The burning rate per

unit area was obtained from our experiments ($0.008\ \frac{kg}{m^2.s}$), then the burning rate of fuel for a large scale fire was the product of burning rate per unit area from the small scale experiment and the total surface area of the fuel in the large scale fire.

- **Extinguishing superiority of CAF over water**

  CAF exhibited better extinguishing performance and higher efficiency. According to this set of experiments, the prominence of CAF over water was quantified. Higher fire-fighting efficiency implies two considerable further consequences. First, the better fire-fighting performance leads to the faster extinguishment of the fire and less production of the gaseous pollutants. However, this is not the most significant result of better extinguishing efficiency. The second and more important consequence of higher fire suppression effectiveness is its impact on the amount of run-off water. The run-off water carries the pollutants from the fire itself and also sweeps the path as it flows. The run-off water is one of the main concerns with respect to the environmental impacts of fire incidents. The higher extinguishment efficiency means less water consumption for fire-fighting and consequently less amount of run-off water. A lower amount of run-off water results in less intensive water flood and a consequently smaller polluted area which should be remedied. According to these tests, CAF shows a 30% higher efficiency compared to water and consequently a minimum 30 % reduction in the affected area by run-off water.

5 Pollutant transport in the soil

The water used during the extinguishment process can be divided into four subsets:

1. Vaporized water because of the heat of the fire
2. Absorbed water by the fuel
3. Sprayed water on adjacent objects
4. Contaminated run-off water

The run-off water is the center of attention with respect to environmental concerns. The run-off water threatens the aquatic environment from toxic releases in two ways. On one hand, it might directly enter the surface waters which is the worst possible scenario. On the other hand, the run-off water is also susceptible to infiltrate through the soil (unsaturated zone of soil) and reaches the groundwater which is one of the main supplies of the drinking water. In this study, the infiltration of run-off water was investigated assuming the fireplace is not in the close vicinity of the surface waters which implies strict regulations about the extinguishment process. In order to investigate the risk of pollution of groundwater due to the run-off water, a rough estimation of the total amount of agent used for extinguishing is needed. Although it is nearly impossible to predict the total amount of agent needed for fire-fighting, Günther developed an empirical approximation to quantify the amount of extinguishing water and also run-off water based on the size of fire [115].

The total extinguishing water (TW):

$$TW\ [m^3] = 1.5 * burning\ area\ [m^2] \tag{5.1}$$

And the amount of run-off water (RW):

$$RW\ [m^3] = 0.75 * burning\ area\ [m^2] \tag{5.2}$$

The main controversial issue is the determination of the composition of the run-off water. There are different factors affecting the type of pollutants and their concentrations in the run-off. The main sources for pollutants in the run-off water are [116]:

1. Burning material:
   Unburnt chemicals, partially burnt chemicals, and products of the combustion reaction
2. Site area:
   Pollutants that are not produced by the fire but exist at the fire scene in the path of run-off. These pollutants are also washed and transported by run-off water

3. Fire-fighting foam:
   The additives added to the extinguishing agent

The hazardous materials from the first two sources can vary over a huge range. The type of the substances in the run-off depends on the burning material and the location where fire takes place. So, the run-off water may encompass a variety of toxicants among which the main subjects of environmental concerns can be classified as:

- Acids such as HCl, HF, HBr, HI, SO_2, NO_x, HCN, etc.
- Heavy metals such as Hg, Cd, As, Pb, Sb, Zn, etc.
- Carbon compounds such as polycyclic aromatic hydrocarbons (PAHs)

However, the characterization of the type and concentration of the pollutants in the run-off is not possible due to the fact that this is scenario dependent and varies from case to case. In order to circumvent this problem and draw a general statement about the pollutant transport by run-off, the concept of ‘groundwater vulnerability’ [117] was chosen as the method dealing with the run-off in this study. Groundwater vulnerability is a measure of how easily contaminants are transported from the land surface to the groundwater and neglects the nature of the possible toxicants contributing to run-off pollution. Thus, the number of factors affecting the investigation is decreased. It just discusses the degree of protection of the groundwater by the first aquifers beneath the ground. Many authors already defined the groundwater vulnerability and some of them are offered in the following in chronological order:

- “Aquifer vulnerability is the possibility of percolation and diffusion of contaminants from the ground surface into natural water-table reservoirs, under natural conditions.” [118]

- “Vulnerability is the degree of endangerment, determined by natural conditions and independent of the present source of pollution.” [119]

- “Groundwater vulnerability is the sensitivity of groundwater quality to anthropogenic activities which may prove detrimental to the present and/or intended usage-value of the resource.” [120]

- "Vulnerability of a hydrogeological system is the ability of this system to cope with external, natural and anthropogenic impacts that affect its state and character in time and space." [121]

- "Groundwater vulnerability is the tendency of, or likelihood for, contaminants to reach a specified position in the groundwater system after introduction at some location above the uppermost aquifer." [122]

As is clear by all the definitions above, the traveling time for pollutants to reach the groundwater is a crucial factor for investigation of the vulnerability of groundwater. The longer the traveling time is, the less is the vulnerability of the groundwater. This is the applied approach in this study to quantify the risk of groundwater pollution due to run-off water. Moreover, the vulnerability assessment is not a precise scientific method to predict the fate of the pollutants; although, It is an efficient way for the first order of approximation.

Soils taken into consideration

The soils' characteristics vary significantly from one place to another place. Precise knowledge about the soil texture and hydraulic properties of the soil can be provided only by experiments. Even in a certain area, changing the location for several meters results in different values for the soil's characteristics. The soil layers are moving next to each other constantly, so the texture of the soil is not constant and is a function of topology. However, the aim of this study is to offer some general ideas about the vulnerability of groundwater and investigation is based on average values representing the texture class of soil. Five different soils were taken into account in this study, three common soils were selected from the twelve standard soil classes provided by Carsel and Parish [123] and two samples were taken randomly from the nature in Magdeburg. The main textures according to Carsel and Parish study are given in table 5.1. The three selected soils are colored in table 5.1.

The other two soil samples were taken from nature in Magdeburg and analyzed in the laboratory [143]. In order to recognize the texture of the soil, the mass percentage of sand, silt, and clay in the soil sample should be known. Then the soil texture and also the hydraulic properties of soil are predicted accordingly. The main procedure in the laboratory was to find the size distribution of the particles in the soil. Based on the knowledge of particle sizes, the contributions of sand, silt, and clay in the soil sample were calculated. The size distributions of both soils are represented in figure 5.1.

Table 5.1: Average values for selected soil water retention and hydraulic conductivity parameters for 12 major soil textural groups according to Carsel and Parrish [123]

Texture	θ_r	θ_s	α 1/cm	N	K_s cm/day
Sand	0.045	0.43	0.145	2.68	712.8
Loamy Sand	0.057	0.41	0.124	2.28	350.2
Sandy Loam	0.065	0.41	0.075	1.89	106.1
Loam	0.078	0.43	0.036	1.56	24.96
Silt	0.034	0.46	0.016	1.37	6.00
Silt Loam	0.067	0.45	0.020	1.41	10.80
Sandy Clay Loam	0.1	0.39	0.059	1.48	31.44
Clay Loam	0.0	0.41	0.019	1.31	6.24
Silty Clay Loam	0.089	0.43	0.010	1.23	1.68
Sandy Clay	0.1	0.38	0.027	1.23	2.88
Silty Clay	0.07	0.36	0.005	1.09	0.48
Clay	0.068	0.38	0.008	1.09	4.80

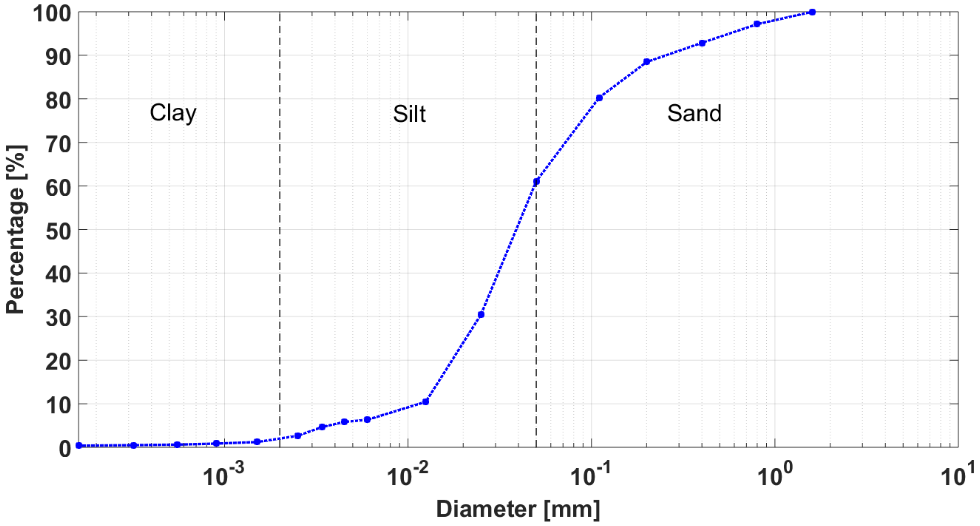

(a)

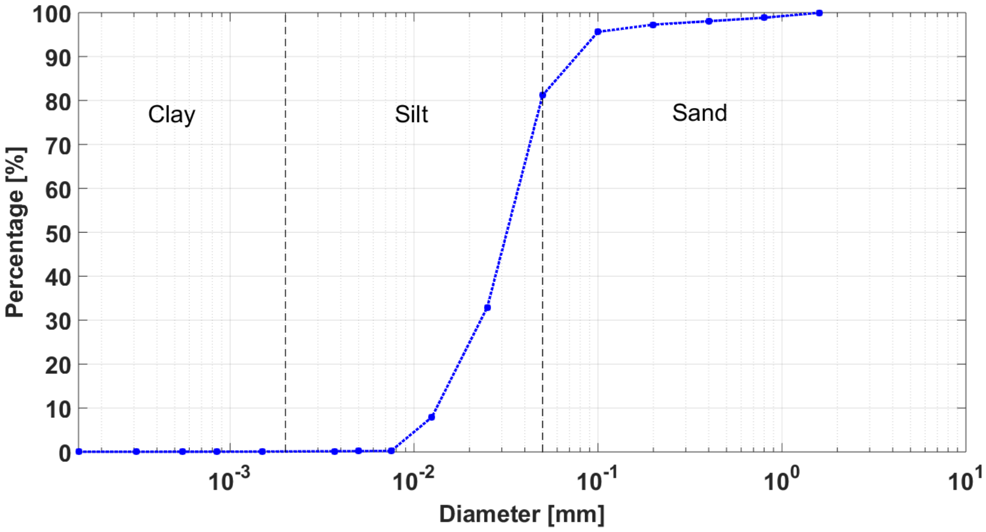

(b)

Figure 5.1: Size distribution, **(a)** for soil 1 and **(b)** soil 2

Particles larger than 0.05 mm are considered as sand whereas particles smaller than 0.002 mm are categorized as clay. The particles with a diameter between 0.002 and 0.05 mm are an indicator of the silt texture. As is clear, both samples have a relatively coarse texture. Soil 1 has 35 % sand, 62 % silt, and 3 % clay. Soils 2 consists of 15 % sand, 85 % silt without any clay. The data about size distributions of both soils are also represented in table 5.2.

Table 5.2: Size distribution data for both soils

Diameter [mm]	**Cumulative mass fractions for soil 1 [%]**	**Cumulative mass fractions for soil 2 [%]**
>0.8	100	100
0.8	97.13	98.85
0.4	92.86	98.06
0.2	88.46	97.27
0.1	80.27	95.65
0.05	61.07	81.20
0.025	30.50	32.92
0.0125	10.44	7.93
<0.0125	3.7	0.21

Both soil samples have nearly coarse texture due to the fact that they are collected from the land surface. This is why both samples also have high hydraulic conductivity. Going deeper, the soil has a higher clay percentage and the texture becomes finer. This implies that samples from the land surface cannot be sufficiently accurate to represent the average characteristics of the unsaturated soil layer. However, these coarse-textured samples can be used to investigate worst-case possible scenario when the soil layer beneath the ground has a very high conductivity (> 50 cm/day) and the vulnerability of the groundwater is high.

The soil texture and the bulk density of the soil are needed to calculate the hydraulic properties and van-Genuchten parameters for soil with RETC code [56]. The soil bulk density is also not a unique function of the type of the soil itself and depends on the topology. The bulk density of the soil is influenced strongly by land use. The region can be urban terrain, rural area, agroforestry, forest, pasture or something else. Every land type results in different pressure and tensions on the soil and consequently different soil bulk density. The bulk densities of the soil 1 and soil 2 were respectively 2 and 1.5 gr/cm^3. Table 5.3 shows the retention data for both soil samples according to the RETC program.

Table 5.3: Soil water retention and hydraulic conductivity parameters for both soils

Texture	$\boldsymbol{\theta_r}$	$\boldsymbol{\theta_s}$	$\boldsymbol{\alpha}$ **1/cm**	$\boldsymbol{n}$	$\boldsymbol{K_s}$ **cm/day**
Soil 1	0.0374	0.35	0.03	1.58	48.05
Soil 2	0.041	0.4	0.05	1.63	62.8

The five selected soil classes as the cases under investigation were chosen in a way to include soils with different textures and hydraulic conductivities. Thus, the effect of type of soil as a significant factor in vulnerability analysis can be discussed.

Simulation setup

The tool used for simulation of solute transport in the unsaturated soil is COMSOL Multiphysics. It allows simulating complex multi-physics by solving highly non-linear partial differential equations. This feature enables us to solve various hydro-geological problems by coupling flow and solute transport equations. The Richards and solute transport equations were defined in the form of partial differential equations available in the Mathematics panel. The coefficient form PDE was selected for expression of the both Richards and solute transport equations (Appendix A).

The run-off water after extinguishment covers the land and forms a pond over it. Therefore, the land surface is saturated with water. The nature of the pollutants was not taken into account in the present study. All dissolved pollutants were considered as a single substance called pollutant (solute) which was present in the run-off at a constant concentration. The dissolved solute was assumed non-reactive, meaning there is no sorption or reaction between the solute phase and soil particles.

The polluted water infiltrates into the soil and carries the pollutants. It is controversial to determine the total area covered by the run-off. This is something that depends on the topology and fire location. Thus, just vertical infiltration and solute transport were considered (1D simulation). The subject of importance in vulnerability analysis is the traveling time for pollutants to reach the water table and the lateral (horizontal) solute transport does not play an important role regarding critical transport time. However, the effect of lateral transport will also be discussed in this chapter due to its effect on the total amount of the soil to be treated after the incident. Other noticeable physical assumptions for the sake of simplicity are that the soil is homogenous and isotropic and also the flow is isothermal. Finally, the simulations were transient due to the transient nature of infiltration through the vadose zone where the water content is constantly varying with time.

5.1.1 Geometry and boundary conditions

The length of the computational domain is the depth of the water table. The depth of the unsaturated soil layer can vary over a considerable range depending on the location. According to online available data offered by Bundesanstalt für Gewässerkunde, the thickness of the soil layer between the surface and water table mostly varies from 1 to 4 m in Germany. It is rarely less than 1 m but can be more than 4 m. However, since this study deals with the worst cases, the depths more than 4 m were not considered because of the lower vulnerability of the groundwater. Four different water table depths of 1, 2, 3 and 4 m were taken into account in this study. Two PDEs were used for modeling of solute transport, therefore, we have two dependent variables (c and H_p). The boundary conditions for each dependent variable must be defined.

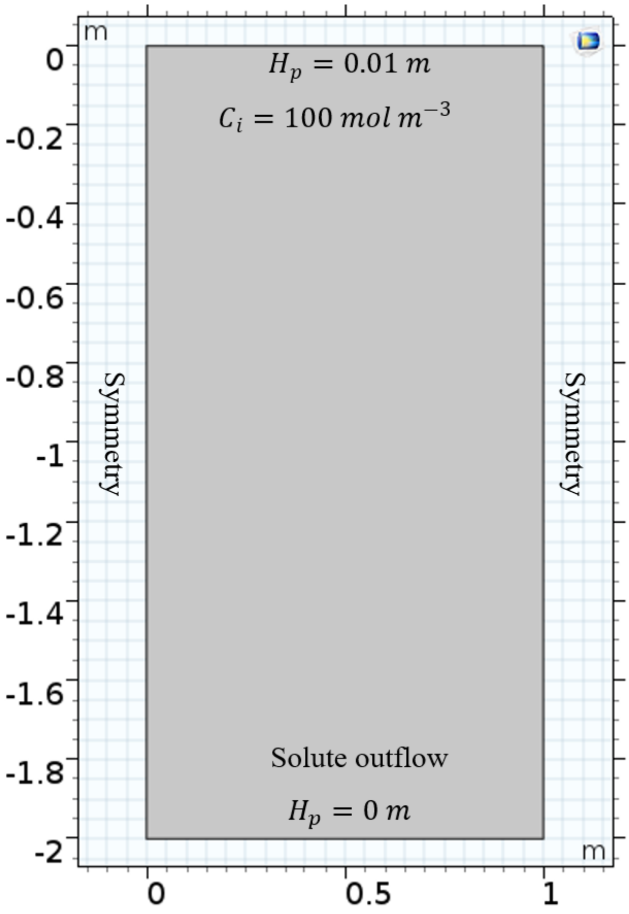

Figure 5.2: Representation of the geometry and boundary conditions

As is clear by figure 5.2, the pressure head at the land surface is zero due to saturation and the concentration of the solute is the constant value of c_0. There is no knowledge about the amount of this constant concentration of the solute in the polluted run-off although this value affects the diffusive solute transport. This effect is discussed at the end of this chapter in the error analysis section. The side edges are symmetry for both concentration and pressure head which reduces the simulation in one direction. The bottom of the domain is the water table. The solute can leave the domain freely with water. So, the corresponding boundary condition for the concentration equation is the outflow condition whereas the boundary condition for pressure head is again the constant value of zero because of fully saturation. Figure 5.2 shows the computational domain just for the case that the water table depth is 2 m. As mentioned, there were four different water table depths under investigation and for each case, a different geometry should be applied. The main reason in this regard is the effect of saturation condition at the water table which can suppress the downward movement of the water and acts as a sort of resistance. However, a detailed explanation of the phenomenon is beyond the aim of this study.

5.1.2 Mesh

Meshing is the spatial discretization of the domain over which the governing equations are supposed to be solved. Therefore, the mesh size plays an important role in the solution accuracy. Although increasing the mesh resolution improves the accuracy, the computational costs are also increased. So, meshing always deals with making a compromise between accuracy and time. In this contribution, the physics-controlled extra fine mesh, which is an unstructured triangular mesh, was used. However, in this set of simulations in this chapter, opting for the meshing technique was not a controversial decision due to the simplicity of the geometry. For such a simple geometry, even a physic-controlled mesh is sufficient to provide fast and accurate results and the user does not need to define the mesh features manually. It should be always taken into account to check the mesh dependency of the simulation results. The mesh dependency was also conducted in our simulations and the extra-fine mesh size was the optimum mesh size. Decreasing the mesh size to extremely fine mesh or manually via the user-controlled option does not change the results furthermore but increases the simulation time.

5.1.3 Initial condition

Each of the PDEs requires an initial condition. The initial condition for the solute transport was the constant zero concentration of the pollutant in the domain meaning at the beginning ($t = 0$), there is no pollutant in the soil. The pollutant enters the soil with the infiltration of run-off water.

The characterization of the initial condition for the water content is not straightforward. The moisture content of the soil varies continuously with the weather conditions. For example, even at a certain location with a certain type of soil, it changes with seasons or even during a day. However, the range of the variation of the water content is limited. It varies between the ‘moisture field capacity’ and saturation. Field capacity is defined as the volume fraction of the moisture without any additional water source after an extended period of gravity drainage [124]. The field capacity values are shown in table 5.4 according to the data offered by Schroeder et al (1994) [125].

Table 5.4: Field capacity values

Soils	Field capacity [%]	S_e(field capacity)
Soil 1	24	0.7
Soil 2	20	0.5
Loam	28	0.65
Silt loam	31	0.69
Clay loam	36	0.86

The saturation at the field capacity is the minimum possible saturation for land soil. The initial degree of saturation of the soil influences the capillary effects and also the unsaturated hydraulic conductivity. Due to the fact that the initial saturation might play a very important role in the infiltration process, the effect of different initial saturations should be investigated. The numerical simulations were conducted at three different initial saturations for each soil. Once with the initial saturation corresponding to the field capacity indicating to the condition that the soil is initially dry. The second time, the initial saturation is chosen very close to the saturation to represent the vulnerability of the groundwater beneath the wet soils. At the third attempt, the average value between the saturation at field capacity and unity (the saturation of a saturated soil) was considered as the initial saturation of the domain. Thus, soil can be initially dry, semi-dry or wet.

Another difficulty in this regard was the characterization of the behavior of the initial moisture curve. The initial saturation can be assumed constant through the whole unsaturated zone but this assumption is not very accurate. The initial saturation is the lowest exactly beneath the land surface and increases with depth (moving towards the water table). The mathematical function for the way saturation goes up with depth is ambiguous. However, the linear increase of initial saturation with depth was assumed for our simulations. Other possibilities for the initial distribution of moisture in the soil are discussed in the error analysis at the end of this chapter.

The dependent variable in the Richards equation is the pressure head. So, the corresponding pressure head for each initial saturation must be calculated to be imported to COMSOL as the input for the initial condition. The calculation of the pressure head based on the saturation was done according to the van-Genuchten relationships.

Table 5.5: Initial conditions for each soli

Soils	**Initial saturation [%]**	**Corresponding pressure head [cm]**
Soil 1	0.7	-45
	0.85	-23
	0.95	-10
Soil 2	0.5	-53
	0.75	-21
	0.95	-6
Loam	0.65	-47.64
	0.85	-19.43
	0.95	-8.36
Silt loam	0.69	-98
	0.85	-40.72
	0.95	-15.56
Clay loam	0.84	-56.18
	0.9	-33.85
	0.95	-17.82

Infiltration

The time needed for pollutants carried by water to reach the groundwater depends on the infiltration rate of water in the soil. As mentioned before, the water table depth in Germany varies between 1 and 4 m. Therefore, four different depths of 1, 2, 3 and 4 m respectively are discussed here. Furthermore, the simulations were conducted for three different initial saturations although in the following only the infiltration graphs corresponding to the field capacity are shown. The solute transfer at other initial saturations follows nearly the same trend for all the cases meaning the initial water content of the soil does not play a substantial role when there is a huge water load. However, the results of all the sixty cases simulated are represented in table 5.6. The criterion to distinguish the moment that the solute reaches the water table was the ratio of $\frac{c}{c_0} = 0.2$ at the lower boundary. This critical concentration ratio for determining the breakthrough curve is mostly assumed a value between 0.15 and 0.3 [140]. So, the time at which the concentration of the pollutant phase at the water table reaches 0.2 of its value available in the run-off water at the land surface is the critical traveling time.

Figure 5.3 shows the solute concentration varying with depth for clay loam. The traveling time for the worst case where the water table depth is the shortest (1 m) is about five and half days (134 Hours) and for the regions with the deepest water table (4 m) is nearly twenty-two and half days (538 Hours). Therefore in the areas where the soil has the texture of clay loam or finer, the traveling time of pollutants to the groundwater is considerably large. So, cleaning and remediation of the soil after the extinguishment is not problematic.

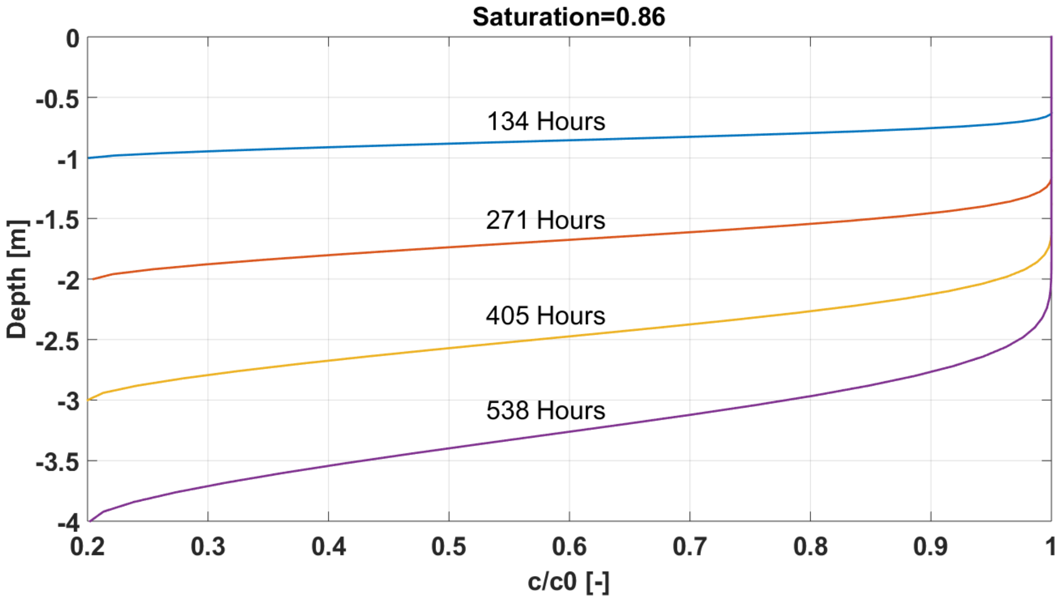

Figure 5.3: Concentration plot of clay loam for water table depths of 1, 2, 3, and 4 m

Moving towards the coarser-textured soils, the hydraulic conductivity increases and the polluted water reaches the water table faster. Silt loam and loam as the soils with moderate texture are discussed by figures 5.4 and 5.5.

For silt loam, the traveling time for polluted infiltrating water to reach the groundwater varies from three and half days (84 hours) for shallow water table with a depth of 1 m to more than two weeks (343 hours) when the water table depth is 4 m (figure 5.4). Loamy soils transfer the water faster compared to clay loam and silt loam due to coarser texture and consequently larger hydraulic conductivity. Figure 5.5 shows that the infiltrating water reaches the depth of 1 m after nearly one day and a half (35 hours). Deeper water tables require more time. As is clear, for the case when groundwater occurs at a depth of 4 m, it takes a little less than six days (141 hours) for pollutants to reach the water table.

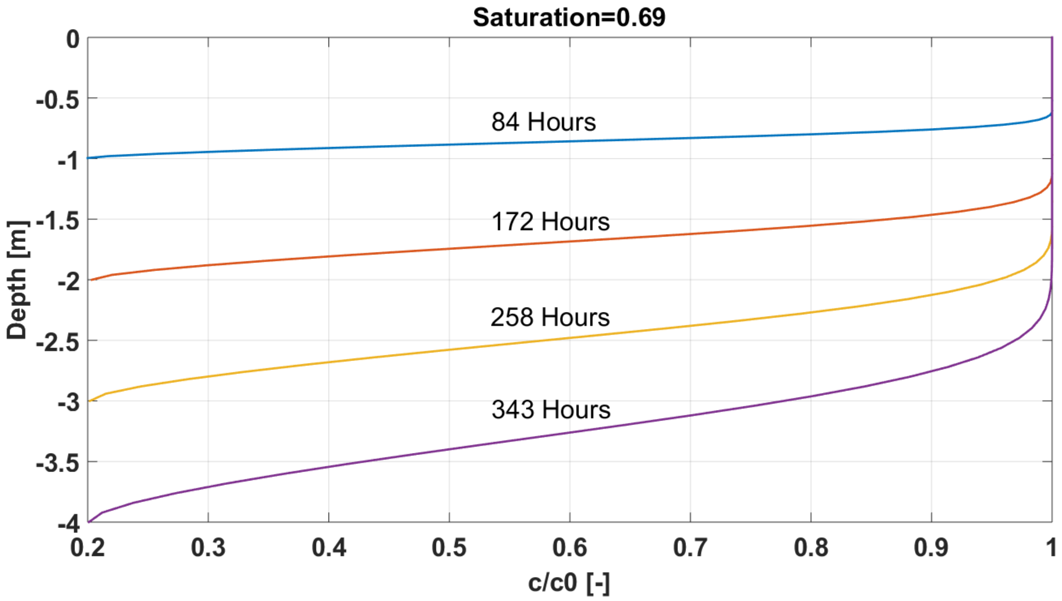

Figure 5.4: Concentration plot of silt loam for water table depths of 1, 2, 3, and 4 m

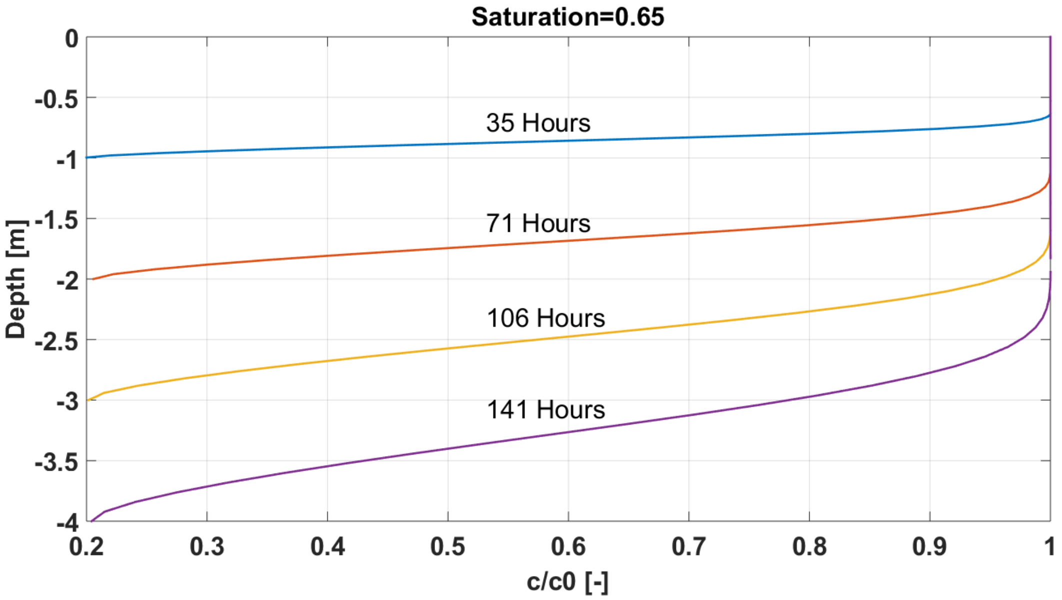

Figure 5.5: Concentration plot of loam for water table depths of 1, 2, 3, and 4 m

However, in areas such as rural areas, agricultural areas, jungles and forests, the soil is less compact compared to municipal areas because of less load and tension on it. In these areas the occurrence of the large texture coarse in the unsaturated zone is probable. Soil 1 and soil 2 were both collected from the different rural areas around Magdeburg. Both samples had a relatively coarse texture and large particle sizes (figure 5.1). In this case, the groundwater is more vulnerable due to the high transfer rate of the unsaturated zone. For both cases, if the groundwater is very close to the land surface (1 m) the polluted water enters the saturated zone in less than one day. So, the groundwater reservoirs are tremendously endangered and the remediation process should start as soon as possible after the extinguishment process. This can be the worst possible scenario when the groundwater level is so close to the surface and soil in the unsaturated zone has a coarser texture and high hydraulic conductivity. The simulation results for soil 1 and soil 2 are illustrated by figures 5.6 and 5.7.

The larger-textured soils do not only transfer the polluted water much faster but also are not able to filter the pollutants effectively. The finer-textured soils can trap a lot of pollutants such as large hydrocarbon molecules, larger carbon, and metal particles and prevent them from entering into the saturated zone.

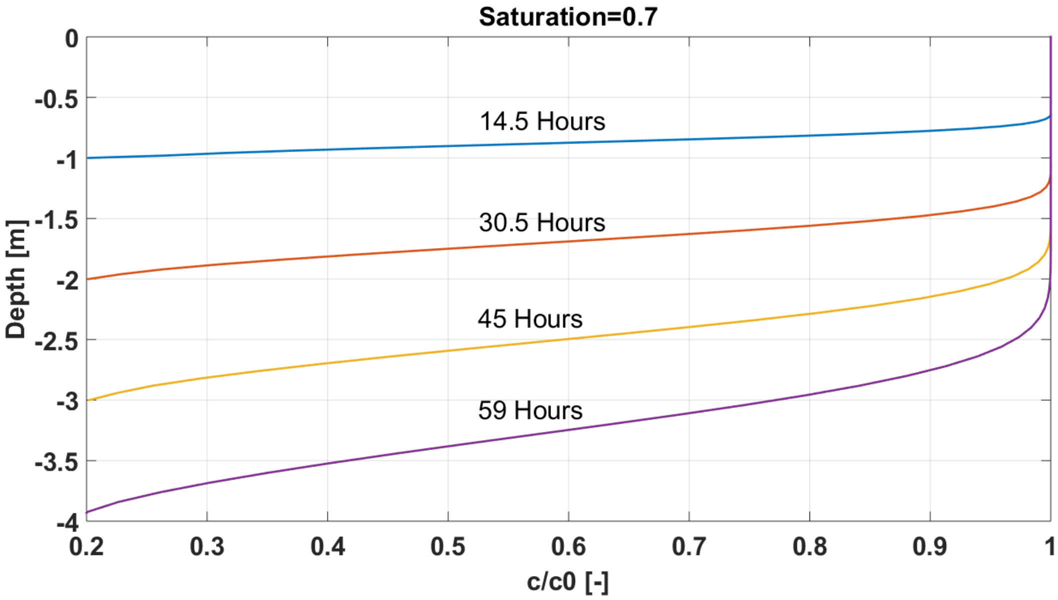

Figure 5.6: Concentration plot of soil 1 for water table depths of 1, 2, 3, and 4 m

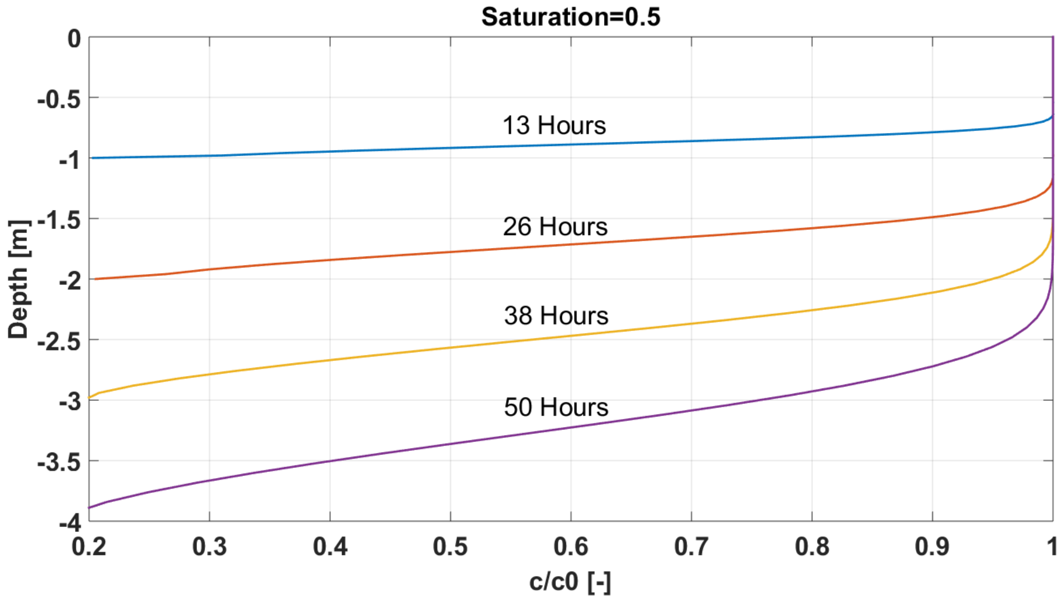

Figure 5.7: Concentration plot of soil 2 for water table depths of 1, 2, 3, and 4 m

A noticeable point that can be seen in all the above figures is that the front of the concentration curve is very sharp at the depth of 1 m (blue curves) whereas it becomes relatively smoother for larger depths. The sharpness of the front of the curve is characterized by mechanical dispersion. The larger the dispersive flux is, the smoother the front of the curve is. As discussed in section 2.6.3, the dispersion coefficient is a function of the field length scale. It increases with increasing the domain size. For small domains the dispersion contribution to the mass transfer is negligible but the effect of mechanical dispersion is more considerable in larger domains where the water table is deeper. The two factors affecting the dispersive flux are the dispersion coefficient and the concentration gradient which depends on the initial concentration of the pollutants in the run-off water. Both factors are discussed in the error analysis section.

All curves shown above are the infiltration curves for the initial saturation corresponding to the field capacity. Each case was simulated with three different initial conditions; initially dry, semi-dry, and wet. The results from all the sixty cases simulated are represented in table 5.6.

Table 5.6: Simulation results of all the 60 cases

Clay Loam	Depth	1 m	1 m	1 m	2 m	2 m	2 m
	Se	0.86	0.9	0.95	0.86	0.9	0.95
	Time	134 h	136 h	137 h	271 h	272 h	273 h
	Depth	3 m	3 m	3 m	4 m	4 m	4 m
	Se	0.86	0.9	0.95	0.86	0.9	0.95
	Time	405 h	407 h	408 h	538 h	539 h	540 h
Silt Loam	Depth	1 m	1 m	1 m	2 m	2 m	2 m
	Se	0.69	0.85	0.95	0.69	0.85	0.95
	Time	84 h	85 h	87 h	172 h	171 h	172 h
	Depth	3 m	3 m	3 m	4 m	4 m	4 m
	Se	0.69	0.85	0.95	0.69	0.85	0.95
	Time	258 h	257 h	258 h	343 h	341 h	342 h
Loam	Depth	1 m	1 m	1 m	2 m	2 m	2 m
	Se	0.65	0.85	0.95	0.65	0.85	0.95
	Time	35 h	36 h	36 h	71 h	72 h	72 h
	Depth	3 m	3 m	3 m	4 m	4 m	4 m
	Se	0.65	0.85	0.95	0.65	0.85	0.95
	Time	106 h	107 h	107 h	141 h	141 h	142 h
Soil 1	Depth	1 m	1 m	1 m	2 m	2 m	2 m
	Se	0.7	0.85	0.95	0.7	0.85	0.95
	Time	14.5 h	15 h	14.5 h	30.5 h	30 h	29.5 h
	Depth	3 m	3 m	3 m	4 m	4 m	4 m
	Se	0.7	0.85	0.95	0.7	0.85	0.95
	Time	45 h	45 h	45 h	59 h	60 h	60 h
Soil 2	Depth	1 m	1 m	1 m	2 m	2 m	2 m
	Se	0.5	0.75	0.95	0.5	0.75	0.95
	Time	13 h	13 h	13 h	26 h	26 h	26 h
	Depth	3 m	3 m	3 m	4 m	4 m	4 m
	Se	0.5	0.75	0.95	0.5	0.75	0.95
	Time	38 h	38 h	39 h	50 h	51 h	51 h

Change in the initial saturation has no significant effect on the traveling time for the pollutants. This is due to the huge water load and dominance of the gravitational force over the capillary force which acts as a resistant force against the infiltration. In all cases, changing the initial condition does not change the traveling time more than two percent which can be neglected. However, in all the simulations it was assumed that the pressure head increases linearly with depth which does not necessarily happen in reality. The pressure head can increase with depth according to various manners. The effect of other initial distributions of the pressure head is discussed in the error analysis section.

Error Analysis

Error analysis means considering the effect of the factors which can affect the simulation results. Errors can appear due to two reasons, the scientific physical assumptions which are assumed for the sake of the simplicity and the mathematical rounding method chosen for the numerical solution of the partial differential equations. The investigation of the simulation error was conducted just for clay loam and soil 2 as the soils with the finest and largest texture. Maximum and minimum errors may appear for these two soils. The most important parameters considered as the potential risks for errors production in the simulation of solute transport in the soil are:

1) The initial distribution function of the pressure head
2) Dispersivity
3) Initial pollutant concentration in the run-off
4) Transverse mass transfer of the pollutants (validity of the 1D simulation)
5) The choice of the water retention curve

5.1.4 Initial function of pressure head

The Richards equation is in terms of pressure head which means that the pressure head is the dependent variable in the partial differential equation (the Richards equation). Therefore, the initial condition is provided for pressure head. However, the initial pressure head is calculated in the way to correspond to the desired initial saturation. The degree of saturation of the soil increases with depth until the fully saturation at the water table. At the surface and shallow depths, the suction is higher and it reduces moving towards the water table. However, the mathematical function of the initial distribution of the pressure head is not clear and its effect on the simulation results will be discussed in the following. The linear increase of the pressure head with depth is assumed in all the simulations in the previous part. In this section, we discuss the circumstances in which the initial pressure head is not linear but parabolic or constant. Four different initial suction head functions were simulated and the solute transport for each initial condition was compared. For the clay loam with domain length of 1 m, the initial pressure head functions investigated are as following:

$$H_p = -0.56y - 0.56 \tag{A}$$

$$H_p = 0.56y^2 - 0.56 \tag{B}$$

$$H_p = -0.56y^2 - 1.12y - 0.56 \tag{C}$$

$$H_p = -0.56 \tag{D}$$

Figure 5.8 shows schematically the different initial pressure head functions used for simulation of clay loam with domain depth of 1 m. However, the same process was repeated for simulation of clay loam with domain depth of 4 m and soil 2 with domain depth of both 1 and 4 m. The initial functions for the other three cases are not written here, but they follow the same trend. Each case was solved four times with four different initial suction head curves, a linear curve (A), two parabolic curves (B & C) and one constant curve (D).

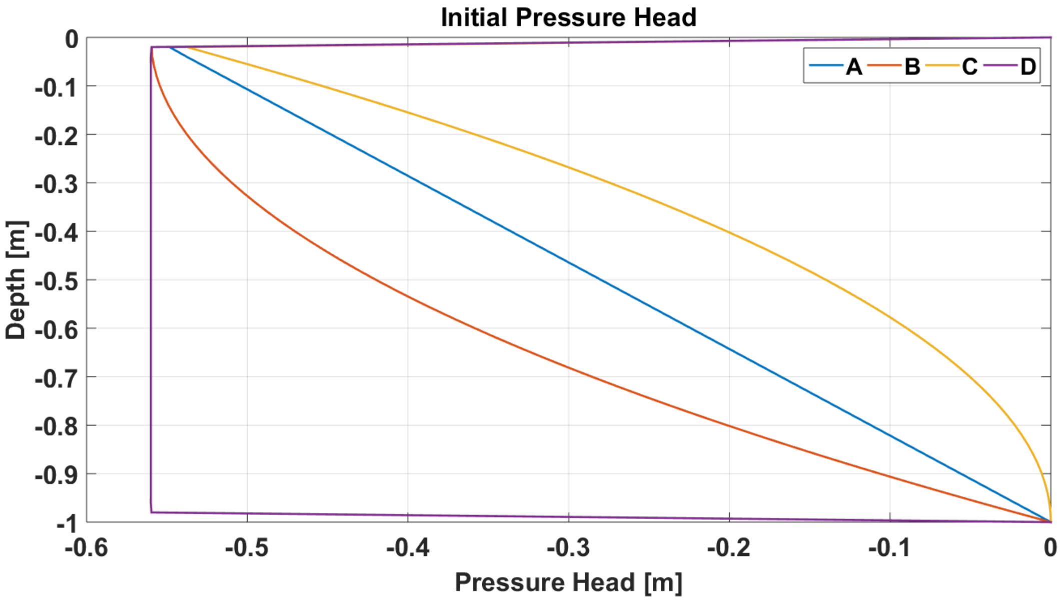

Figure 5.8: Four different initial conditions for pressure head distribution

The comprehensive knowledge of initial pressure head distribution in the unsaturated zone is impossible. In the following, the effect of these initial distribution functions (A, B, C & D) on the solute transport and critical time for the solute to reach the groundwater is clarified.

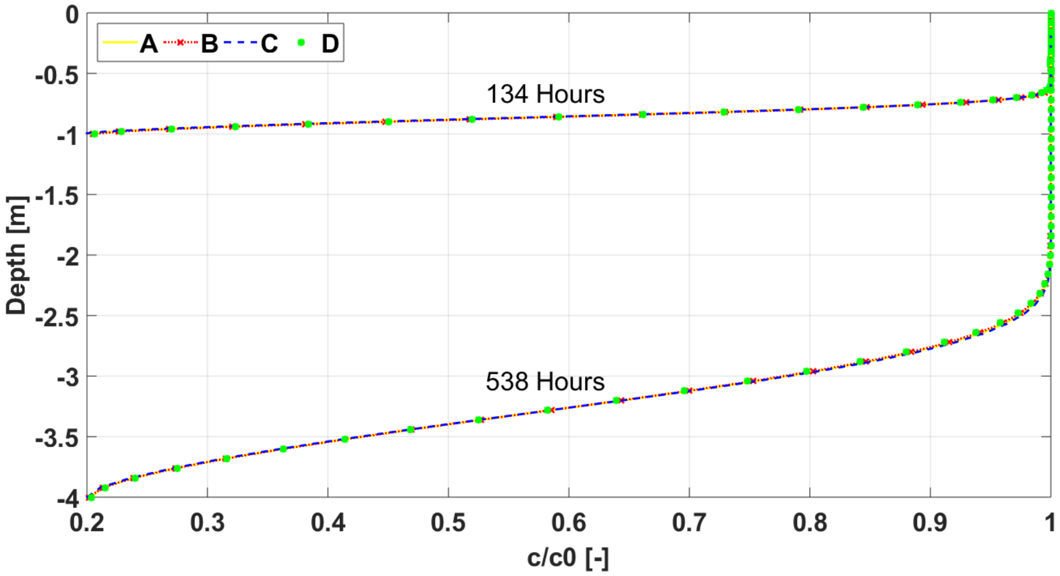

Figure 5.9: Concentration plots of clay loam for water table depths of 1 and 4 m with different initial pressure head functions

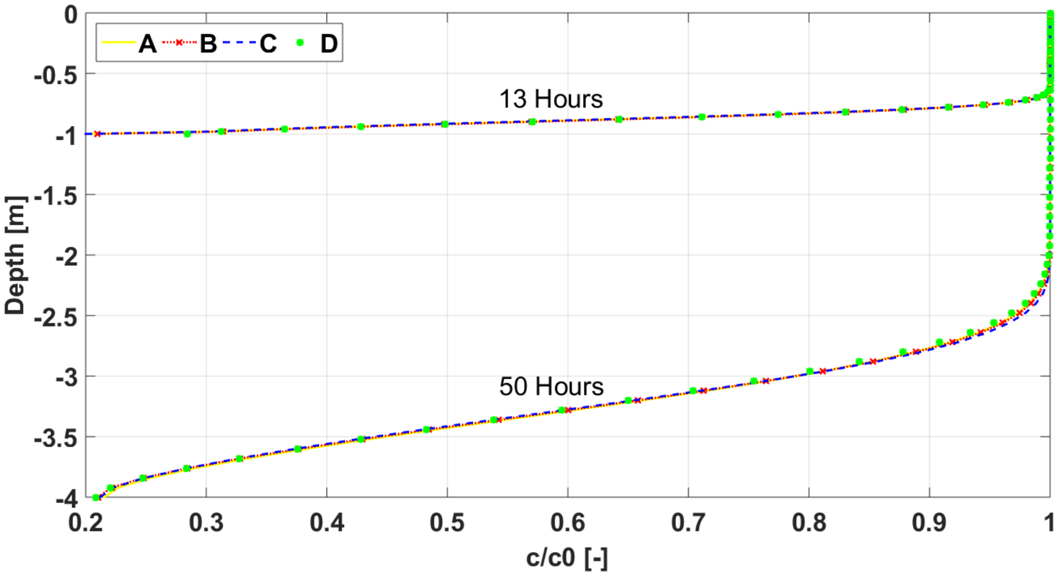

Figure 5.10: Concentration plots of soil 2 for water table depths of 1 and 4 m with different initial pressure head functions

The simulation results from section 5.3 proved that different initial saturations of the soil do not cause a significant difference in the solute transport process. All three initial water content conditions namely dry (field capacity), semi-dry and wet lead to relatively same results. In this section, the effect of initial mathematical function for pressure head given to software is analyzed. All four cases under consideration (clay loam '1 m', clay loam '4 m', soil 2 '1 m', soil2 '4 m') reveal the fact that the final results are independent of the defined initial function for pressure head. The concentration curves obtained from simulations with all the four initial functions (A, B, C, and D) lay on each other.

This noticeable outcome circumvents the controversial process of estimation of the initial water distribution in the soil. This implies the fact that the initial degree of saturation of the soil and the manner of variation of the water content with depth has no serious effect on the pollutant transport phenomenon when a huge water flux enters into the soil continuously for a long period which happens during extinguishment process of the huge fires. The water needed for fire-fighting creates a massive run-off flood covering a big area. This establishes a pond on the ground staying for a long time and making the land surface completely saturated. The infiltrating water flux into the soil reaches its maximum capacity. Under this condition, the capillary force loses its importance and gravity is the dominant force.

The importance of the capillary force depends on the degree of saturation. The negligible capillary effect means that the degree of saturation is not important. It should be noticed that this outcome cannot be extended to all cases of pollutant transport through the vadose zone. This is only true for the condition where there exists a huge continuous load over the land surface like the pond created by run-off water after extinguishment. However, it is a great point to know that a comprehensive knowledge of the initial saturation is not necessary since it is not possible in reality to measure it easily. This fact can be even more important for the fire accident scenario when there is always a lack of time for making the decision.

5.1.5 Dispersivity

Dispersivity is needed to calculate the mechanical dispersion coefficient and consequently the dispersive flux. So, the dispersivity controls the contribution of the mechanical dispersion in the solute transport process. For small scale laboratory experiments, the dispersivity can be assumed constant whereas the assumption of the constant dispersivity is not true in the real field scale. As discussed before, dispersivity is a function of both time and distance although in practice mostly the dependence of dispersivity on time is ignored. For large-scale domains such as the unsaturated zone where the length scale varies from one to several meters, the influence of the distance on the dispersivity should be taken into account. There are several mathematical expressions representing dispersivity as a function of distance out of which the following relationships are the most widely accepted according to the literature [124]:

$$alpha1 = 0.1L \tag{5.3}$$

$$alpha2 = 0.0175\, L^{1.46} \tag{5.4}$$

Both relationships are valid for length scales smaller than 100 m. The dispersivity function ‘alpha2’ is much more accurate based on literature [124]. The formula for dispersivity ‘alpha1’ is less complex resulting in much less simulation duration but not as precise as the ‘alpha2’. In this section, the effect of the different dispersivity functions on the prediction of the contribution of dispersive flux in the pollutant transport process will be analyzed. The same as before, error analysis is limited to four extreme cases of clay loam with water table depths of 1 and 4 m and soil 2 with water table depths of 1 and 4 m. However, due to the dependence of dispersion on the length scale, it is expected that the effect of the selection of different expressions for dispersivity should be more noticeable and considerable for larger domains where the groundwater is deeper from the land surface.

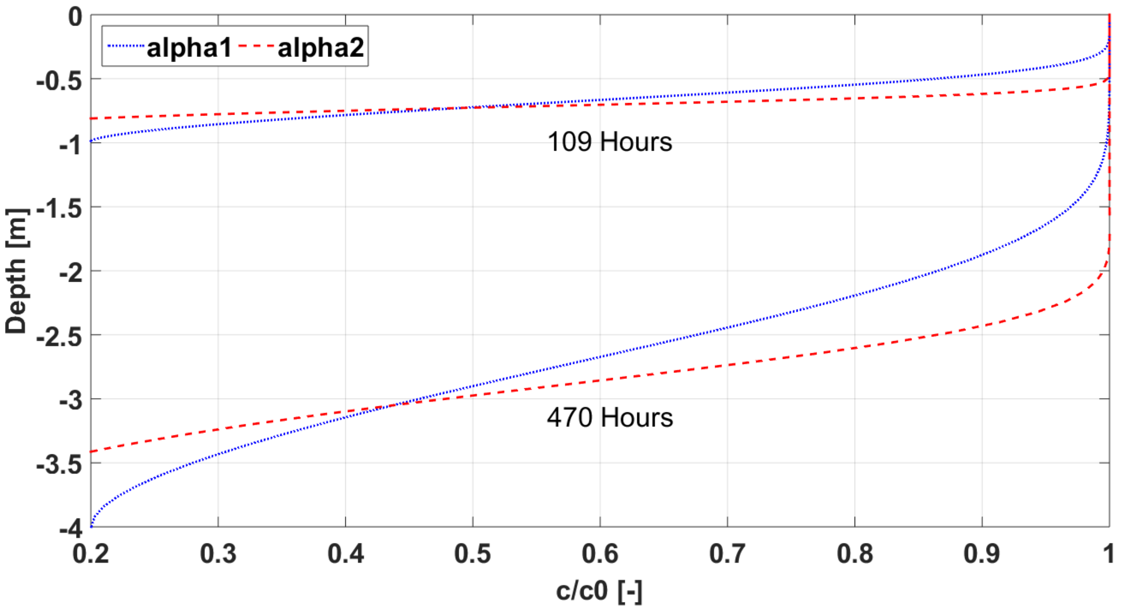

Figure 5.11: Concentration plots of clay loam for water table depths of 1 and 4 m with different dispersivity functions

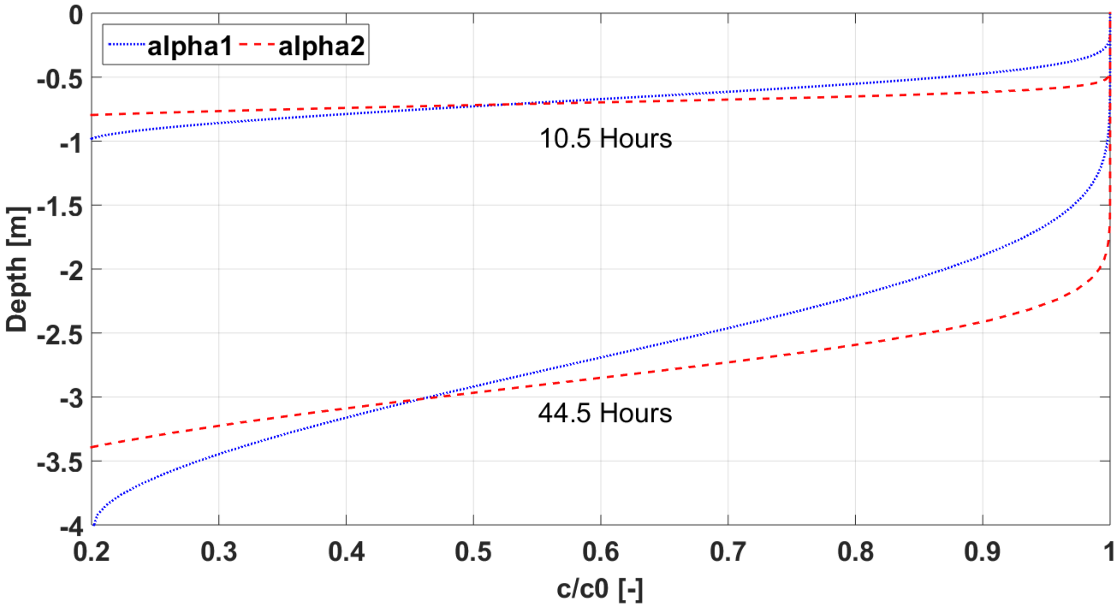

Figure 5.12: Concentration plots of soil 2 for water table depths of 1 and 4 m with different dispersivity functions

The blue lines in each graph are the concentration plots obtained from the simulations in which the 'alpha1' function was used for dispersivity whereas the red curves are from simulations with 'alpha2' function as the dispersivity function. As is clear, from both figures (5.11 and 5.12), the discrepancy between the concentration curves becomes more substantial at deeper depths which was also expected before running the simulations. The 'alpha1' function predicts larger dispersive flux and consequently faster solute transport. The smooth blue concentration curves indicate the gradual decrease of concentration at the solute front which represents the larger dispersion zone. The beginning of the dispersion zone in most of the studies is approximated by the point where $\frac{c}{c_0} = 0.95$. In all four cases, the blue curve shows a larger dispersion zone.

To quantify the effect of the dispersivity function, the simulations of this section should be compared with the results available in table 5.6. For clay loam, the polluted water reaches the depth of 1 m after 134 hours and 4 m after 538 hours when the 'alpha2' function is used for dispersivity according to table 5.6. Applying the 'alpha1' function results in 109 and 470 hours of traveling time for respectively 1 and 4 m deep water tables. Using 'alpha1' for the simulations predicts faster transport of pollutants from the land into the groundwater. In the case of soil 2, the traveling time for pollutant flux to reach the depths of 1 and 4 m is respectively 13 and 50 hours using 'alpha2' as dispersivity whereas applying the 'alpha1' shortens the traveling time to 10.5 and 44.5 hours. Comparison of the results obtained from simulations with both dispersivity functions reveals the fact that the dispersivity function is susceptible to alter the final simulation results between 10 to 20 percent which is a considerable deviation.

The simulation results are more sensitive to dispersivity function for coarser-textured soils due to higher hydraulic conductivity. The mechanical dispersion is the result of diffusion and advection at the same time. Dispersion flux becomes greater when the advection velocity is higher. This phenomenon occurs in coarser-textured soils with larger conductivity through which water moves faster. It can be concluded from this section that the dispersivity has a serious influence on the solute transport process which should always be noticed. In this study, the ‘alpha2’ was chosen for all the simulations but it is not always straightforward to apply it due to its complexity. The geometry is so simple in our simulations which does not happen all the time. Sometimes the domain is complex or very large which demands a huge computational effort. In such circumstances, simpler mathematical functions are favorable to save a considerable amount of time and run the simulations faster especially when there is an estimate over the potential possible error that can appear applying the simpler mathematical expression. According to the size of the domain and complexity of the geometry, the user should decide on the selection of the dispersivity function.

5.1.6 Initial dissolved concentration

The characterization of the composition of the run-off is not feasible. There are many factors affecting the type and concentration of pollutants in the run-off water. The aim of this section is to explain the dependency of simulations on the initial dissolved concentration of the pollutants. In other words, the subject of importance is the effect of the initial concentration of the dissolved pollutants on the traveling time the pollutant flux needs to enter the groundwater. Convection and mechanical dispersion are the only two fluxes contributing to the pollutant transport process. Convective velocity is independent of the concentration of the pollutants. The pollutants are carried by the bulk motion and the transportation speed is not affected by the concentration of the solute whereas there is another story for the dispersive flux. The dispersive flux is mathematically described by Fick’s law which includes the concentration gradient. The concentration gradient is the driving force for the dispersion phenomenon. This effect will be discussed in the following.

In order to examine the effect of initial dissolved pollutant concentration on the solute transport, the simulations are conducted for four different initial concentrations of 1, 10, 100 and 300 $kmol/m^3$. The cases under investigation were introduced at the beginning of the section of error analysis; clay loam and soil 2 both with water table depths of 1 and 4 m. As shown by figures 5.13 and 5.14, all the concentration curves obtained from simulations with different initial dissolved concentrations lay on each other meaning the initial concentration of the pollutants in the run-off does not change the traveling time considerably. Therefore, for the sake of calculation of the risk endangering groundwater by the run-off, the exact knowledge of the composition of the run-off is not necessary.

As is clear, altering the initial dissolved concentration from 1 to 300 $kmol/m^3$ has no effect on the concentration plots. This can be explained according to the role that each transport flux plays in the solute transport process. For short distances, the convective flux is the dominant mechanism of solute transport. The Dispersion effect becomes noticeable for longer length scales. Water owes high density and gravity acts enormously upon it. The effect of the gravitational force is incorporated in the convective mass transport. So, due to the dominance of the gravity over other forces in the case of water flood, the convection plays the most important role for the solute transport process. Dispersion can be significant for gasses or fluids with lower density.

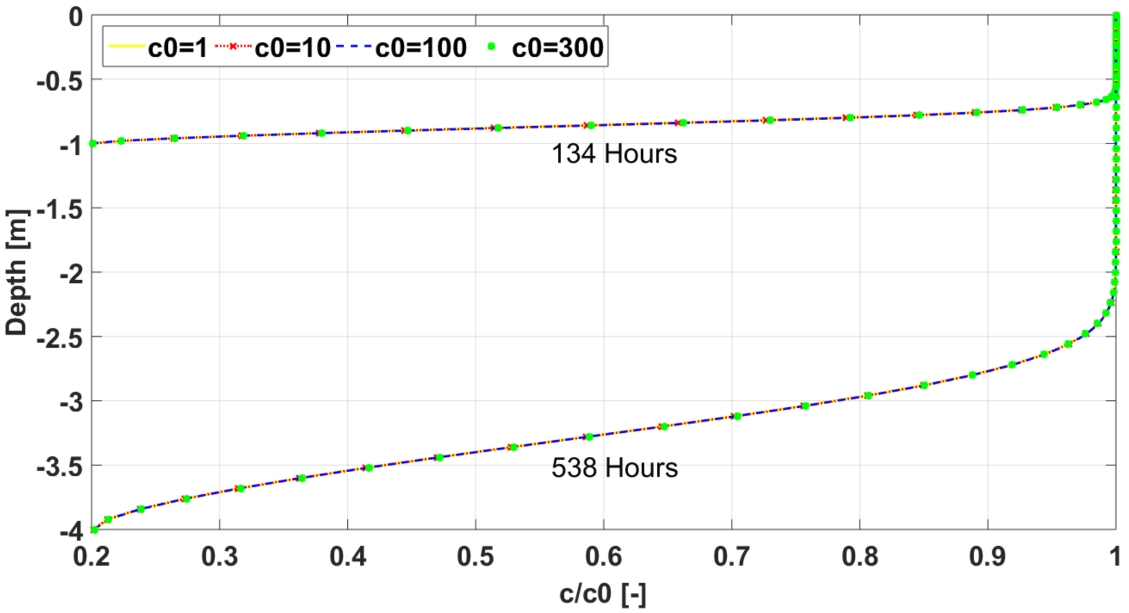

Figure 5.13: Concentration plots of clay loam for water table depths of 1 and 4 m with different initial solute concentrations

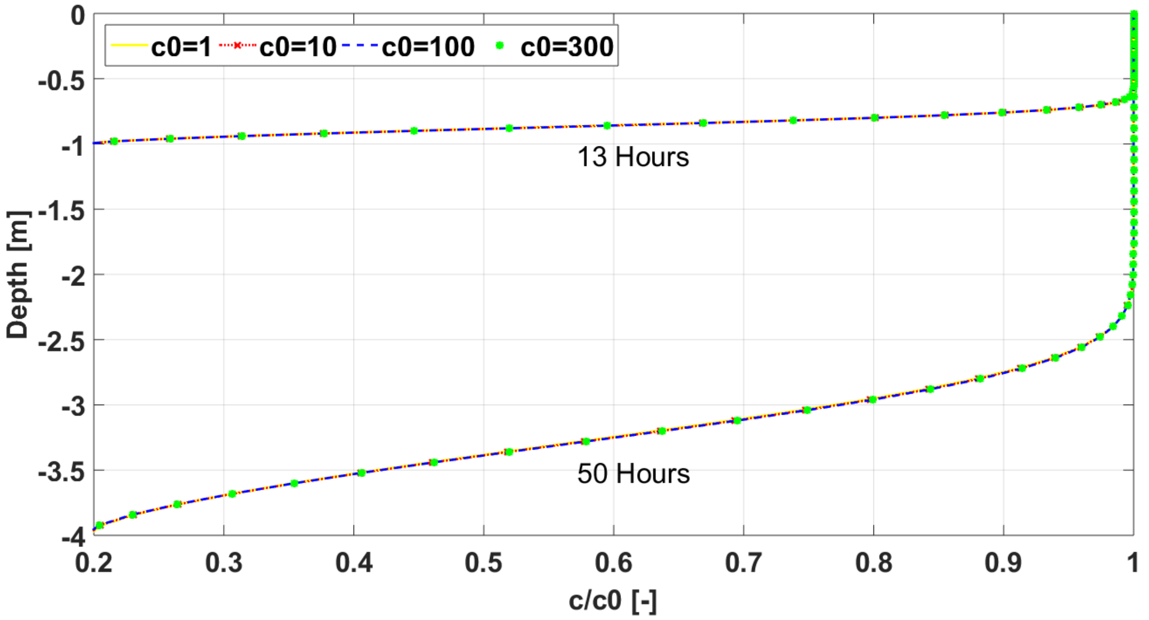

Figure 5.14: Concentration plots of soil 2 for water table depths of 1 and 4 m with different initial solute concentrations

The reason that why changing the initial concentration has no substantial influence on the transport process can be made clear by investigation of the importance of both convective and dispersive fluxes in the transport process (figure 5.15). For this purpose, the simulation case of clay loam with a depth of 4 m was selected to be discussed. However, all the other cases also follow the same trend. The case was solved four times with different initial concentrations of 1, 10, 100 and 300 $kmol/m^3$. The convective velocity is the same for all four cases and is independent of the solute concentration whereas the convective flux increases with an increase of concentration. The dispersive flux varies with the change in the initial concentration but as figure 5.15 illustrates, the dispersive flux for all the cases is approximately one order of magnitude smaller than the convective flux. According to this point, the problem of characterization of the run-off water composition is solved or at least can be forgotten for the first emergency risk analysis which is the determination of the traveling time for polluted water to reach the water table and enter groundwater resources.

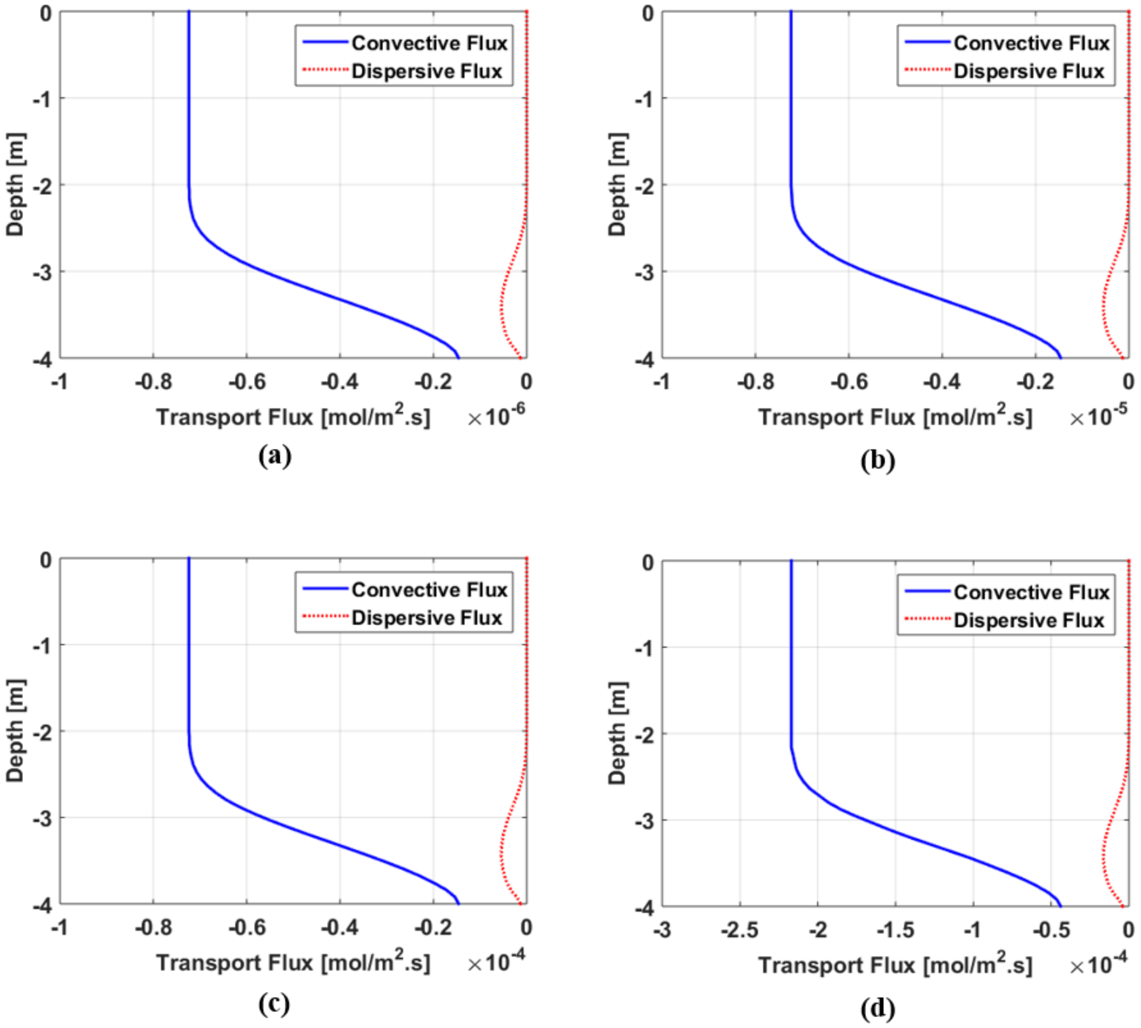

(a) (b)

(c) (d)

Figure 5.15: Comparison of convective and dispersive fluxes for initial solute concentrations of (**a**) 1, (**b**) 10, (**c**) 100 and (**d**) 300 $kmol/m^3$

5.1.7 Assumption of 1D simulation

The real scenario simulation is 3-dimensional which means that the water does not only infiltrate vertically through the unsaturated zone but in all directions. Similar to the vertical water flow, the transverse movement of water in the soil includes both convection and dispersion mechanisms. Radial dispersion always occurs but the radial convection happens only in unsaturated media. The driving force for convective transport is the gradient in the pressure head which happens in the case of water infiltration in the unsaturated medium. The wetted area becomes saturated and consequently owes a higher pressure head compared to horizontally adjacent points. Due to this difference in the pressure head, water moves laterally. However, 3-dimensional simulation is extremely computationally expensive and in this contribution, 1-dimensional simulations were conducted to skip the simulation time problem. This implies the fact that the transverse transport is neglected compared to the domain size. This assumption is discussed in this section.

The burning area of the smaller fire under consideration in this study is $50 \times 50m^2$. According to the approximation provided by equation 5.1, 3750 m^3 of water is needed to extinguish the fire and about 1875 m^3 of water flows as run-off after the application. If the pond formed by run-off is assumed to have a 2 cm depth with a circular base, then the radius of this circle is about 173 m. In this section, just the clay loam and soil 2, both with domain depth of 4 m, are investigated in terms of transverse solute transport. The axisymmetric model is used for the 3-dimensional simulations. Figure 5.16 shows schematically the domain and concentration contour for clay loam at the traveling time. The radius of the cylinder (domain) is 200 m and the radius of the area covered by run-off (red area) is 173 m. The height of the cylinder is 4 m.

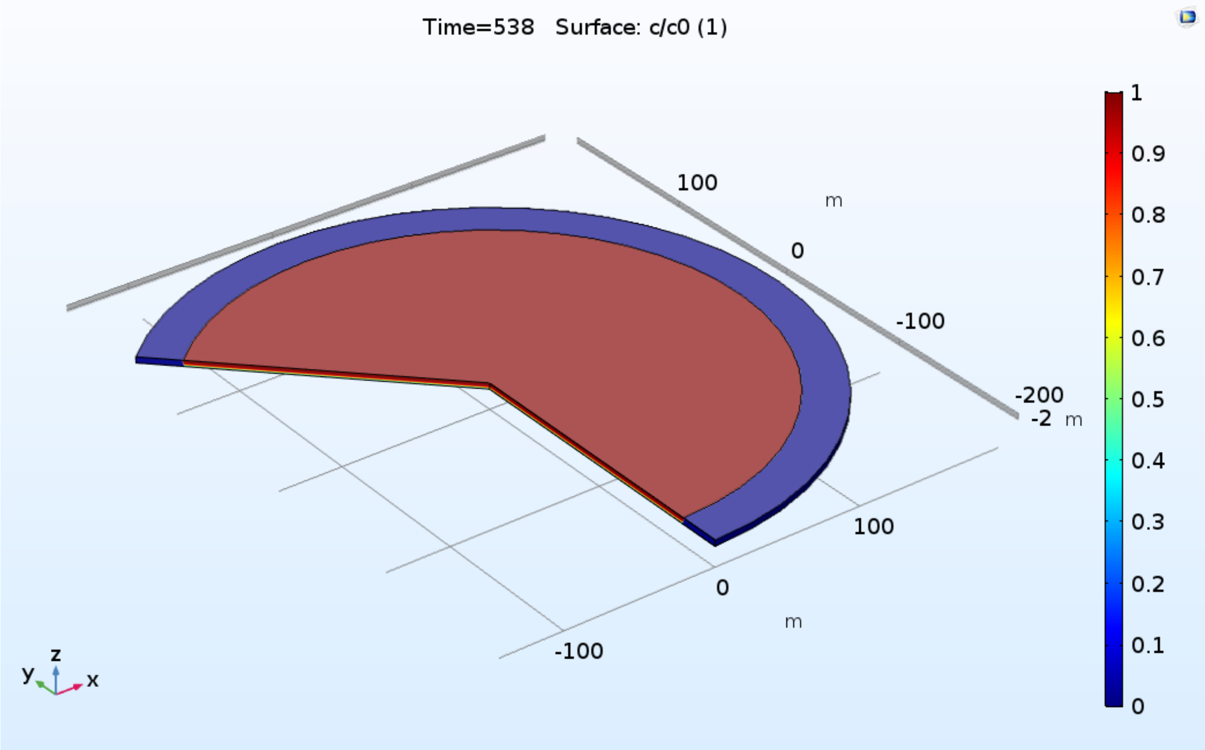

Figure 5.16: Concentration contour of the 3-dimensional domain

Figure 5.17 is the same concentration contour as figure 5.16 (for clay loam at the traveling time) but zooms in on the edge of the pond. It should be noted that running the simulation for times much longer than the traveling time also does not change the plume shape in the soil (plume reaches the steady shape).

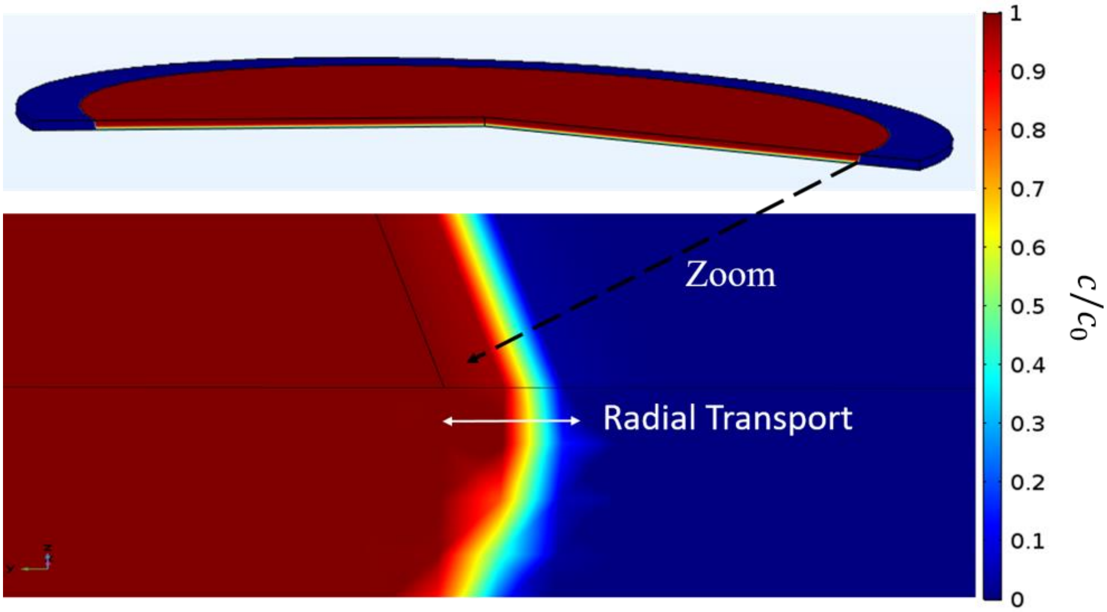

Figure 5.17: Schematic representation of radial transport

As is shown by the concentration contour of figure 5.17, the pollutants also move perpendicular to the main vertical transport direction. The objective of this part is the quantitative investigation of the transverse solute transport. For this purpose, the solute concentration is plotted on three imaginary horizontal lines at different depths of 10, 50 and 100 cm beneath the land surface. The results are represented by the following figures (5.18 and 5.19).

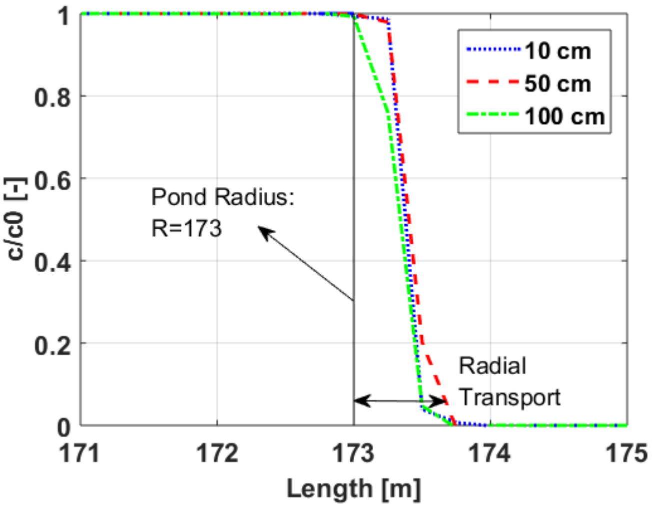

Figure 5.18: Concentration plot on horizontal lines at different depths for clay loam

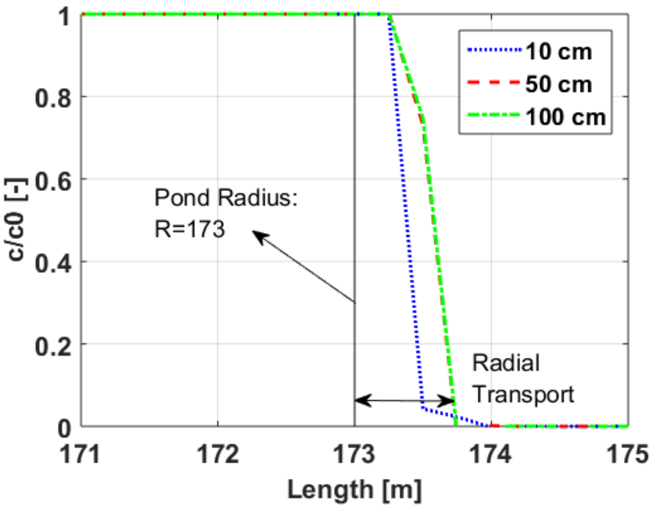

Figure 5.19: Concentration plot on horizontal lines at different depths for soil 2

All plots above are at the traveling time, 538 hours for clay loam (figure 5.18) and 50 hours for soil 2 (figure 5.19). Both figures zoom in on the vicinity of the run-off pond edge in order to provide a clearer view of the phenomenon. The radius of the pond is 173 m. For lengths smaller than the radius of the pond, the ratio of the c/c_0 is unity whereas this ratio equals zero for length larger than 174 m. The concentration drop occurs just in less than one meter for both cases; clay loam and soil 2. The distance the pollutant moves laterally is about 0.5 % of the pond radius. This implies the fact that the assumption of 1-dimensional solute transport is not far from reality.

In order to skip the long and costly computations, the 1-dimensional simulation can be conducted to calculate the critical time for pollutants to reach the groundwater and radial transport is estimated by a reasonable safety factor. The safety factor should always be considered even for 3-dimensional simulation. The numerical simulation is essentially incorporated with errors due to physical assumptions and mathematical rounding techniques. It should be mentioned at the end that applying either 1-dimensional or 3-dimensional simulation does not affect the vertical transport and the quantity of the traveling time. These results support the idea that the 1-dimensional simulation is fairly sufficient for the first order of approximation at the time of occurrence of an accident.

5.1.8 Water retention curve

The Richards equation is highly non-linear and a retention model is needed to establish a functional relationship between the pressure head, water content and unsaturated hydraulic conductivity. According to scientific citations, the Brooks-Corey (B-C) and van-Genuchten (V-G) models are the most popular especially in hydrology. The V-G model was used in this study because of its higher degree of accuracy but it is more complex compared to the B-C model. A significant undesirable feature of the B-C model is the existence of a discontinuity at air entry pressure which leads to numerical difficulties near the saturation condition. The B-C model is less accurate compared to the V-G model but still interesting due to its mathematical simplicity. In this section, a quantitative comparison between these two retention models is provided.

In order to apply the simulation for clay loam and soil 2 with B-C as the retention curve, the air-entry pressure H_b and shape factor λ (B-C constants) should be provided for each soil. For this purpose, parametric conversion from V-G to B-C has been done based on the following empirical equations [126]:

$$\lambda = \frac{m}{1-m}\left(1 - 0.5^{1/m}\right) \tag{5.5}$$

$$H_b = \frac{S_x^{1/\lambda}}{\alpha}\left({S_x}^{-1/m} - 1\right)^{1-m} \tag{5.6}$$

$$S_x = 0.72 - 0.35e^{-n^4} \tag{5.7}$$

Here, m and n are the van-Genuchten parameters and S_x is an auxiliary parameter called match-point effective wetting point saturation. The soil data used in the simulations are listed below. Tables 5.7 and 5.8 show the values for H_b and λ calculated with equations above according to van-Genuchten parameters for clay loam and soil 2.

Table 5.7: V-G and B-C parameters for clay loam

Clay Loam			
Variable	**Unit**	**van-Genuchten**	**Brooks-Corey**
$\boldsymbol{\theta_s}$	-	0.41	
$\boldsymbol{\theta_r}$	-	0.01	
$\boldsymbol{K_s}$	ms^{-1}	7.22 E-7	
$\boldsymbol{\alpha}$	m^{-1}	1.9	-
$\boldsymbol{n}$	-	1.31	-
$\boldsymbol{H_c}$	m	-	0.408
$\boldsymbol{\lambda}$	-	-	0.293

Table 5.8: V-G and B-C parameters for soil 2

Soil 2			
Variable	**Unit**	**van-Genuchten**	**Brooks-Corey**
$\boldsymbol{\theta_s}$	-	0.39	
$\boldsymbol{\theta_r}$	-	0.041	
$\boldsymbol{K_s}$	ms^{-1}	7.26 E-6	
$\boldsymbol{\alpha}$	m^{-1}	5	-
$\boldsymbol{n}$	-	1.63	-
$\boldsymbol{H_c}$	m	-	0.128
$\boldsymbol{\lambda}$	-	-	0.5252

It can be seen in figure 5.20 that the B-C predicts faster solute transport compared to V-G. The solute front reaches the water table at the depth of 1 m in 117 hours whereas the solute front is at the depth of 80 cm at this time based on V-G. The traveling time for the solute to reach 1 m depth is 135 hours using the V-G model. The difference of the curves is also substantial for domain depth of 4 m. The traveling time of the solute front for a 4 m deep water table is 495 hours applying B-C as the retention model whereas this quantity is 538 hours for the same setup with V-G as the water retention curve. However, it is clear that there is a considerable difference between two models in terms of prediction of the traveling time for solute; 18 hours of difference for shallow water table of 1 m and 43 hours for the water table depth of 4 m.

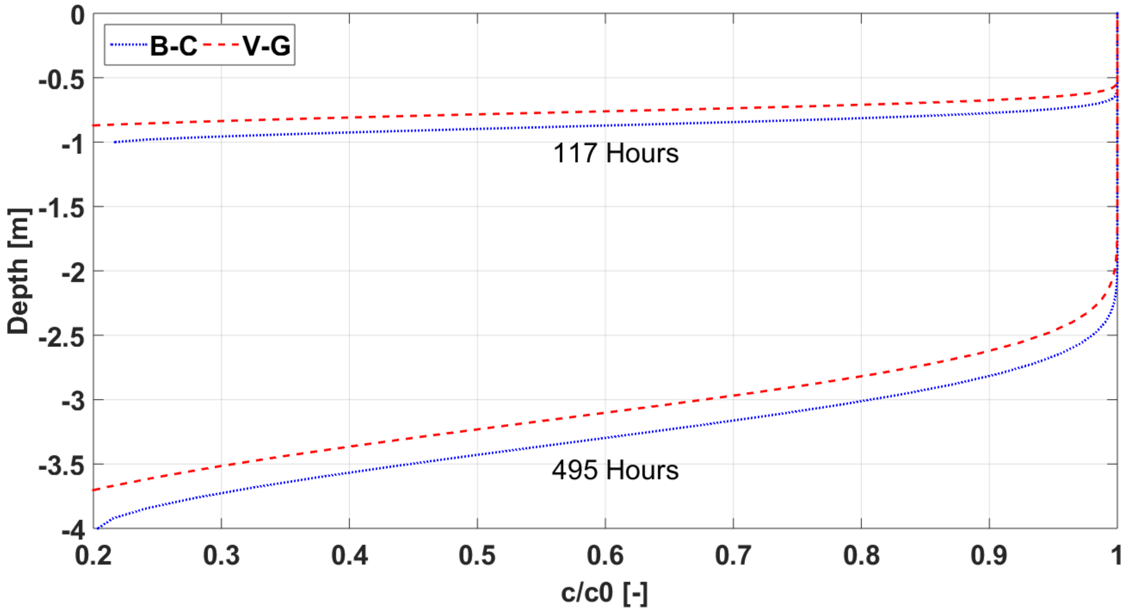

Figure 5.20: Concentration curves of clay loam for depths of 1 and 4 m using V-G & B-C

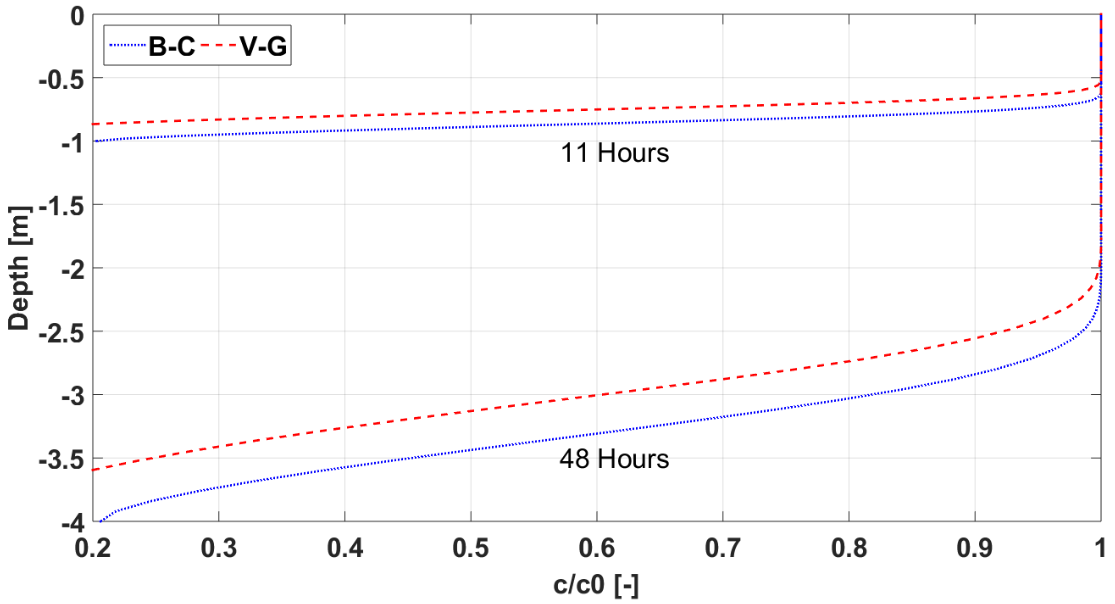

Figure 5.21: Concentration curves of soil 2 for depths of 1 and 4 m using V-G & B-C

There is still a slight difference between the two models in the case of soil 2 as the coarsest-textured soil (figure 5.21) but much smaller compared to clay loam with the finest texture. For water table depth of 1 m, B-C predicts the duration of 11 hours for the solute front to reach the groundwater whereas the V-G predicts 13 hours. For a deeper water table of 4 m, the duration of 48 and 50 hours are predicted respectively by B-C and V-G. The discrepancy of both models in terms of prediction of traveling time is only 2 hours. This implies the fact that for coarser-textured soils, both models are relatively similar; however, moving towards finer-textured soils, the B-C model deviates from the V-G and loses its accuracy. The main reason for this is the lack of well-defined air-entry pressure value for finer-textured soils [11]. As is clear, B-C always overestimates the rate of solute transport compared to V-G. According to the discussions above, it is obvious that the choice of the water retention curve has a significant impact on the simulation of the infiltration through unsaturated soils.

Outcomes

The final scope of this chapter was to make a comparison between CAF and water with respect to their environmental impacts on soil and groundwater. The three strategies of dealing with a fire investigated in this study are extinguishment with water, extinguishment with CAF and letting the fire burn. In the last approach, there is no direct release of pollutants to the soil or water resources; however, the pollutants releasing into the air might deposit. Therefore, only the first two approaches are compared in this chapter.

Extinguishment of fire either with either water or CAF results in the run-off flood. A considerable part of the run-off infiltrates into the soil towards groundwater resources. Accordingly, there are two subjects of concern; soil pollution and groundwater pollution. The soil should be treated after the accident while the polluted soil infects the food chain and also the trapped pollutants might transfer to groundwater with later precipitations. However, the process of remediation of the soil should take place urgently to prevent the transportation of the pollutants dissolved in the infiltrating water to the groundwater. For this purpose, five common soils in nature were selected and the time needed for the polluted infiltrating water to reach the groundwater was calculated for different conditions of water table depth and initial soil saturation. This was accomplished by the simulation of sixty cases summarized in table 5.6. This traveling time determines how fast the remediation of the soil must start. The traveling time of the pollutants to reach the groundwater is nearly independent of the extinguishing agent.

The main difference between CAF and water with respect to soil pollution is the total land surface area polluted by run-off after extinguishment. The less the polluted area is, the smaller the amount of soil should be treated. Based on the results of our small scale experiments in chapter 4, CAF shows 30 % fire-fighting superiority over water for mixed class A fires. Accordingly, it can be assumed that water consumption is reduced by at least 30 %, consequently the covered area by the run-off decreases. As mentioned in chapter 1, there are two big fires with burning areas of $50 \times 50\ m^2$ and $100 \times 100\ m^2$ under consideration. The total amount of water for fire-fighting and run-off were roughly approximated by the empirical equations 5.1 and 5.2 based on the size of fire (surface area of the fuel get involved in the burning). These data are summarized in table 5.9. The run-off finally stabilizes and forms a pond over the land. It is not straightforward to determine the depth of the pond since the ground surface is not uniform over a huge area. As it was explained earlier in the introduction, the fire is assumed to take place in a rural area with bushes and vegetation which prevent the run-off to flow freely over the land. Here, the 10 cm depth is assumed for the pond made by run-off and the calculation of the covered area by the run-off (pond area) is done based on this assumption. However, the depth of the pond does not affect the infiltration process and only has an influence on the amount of polluted area.

Table 5.9: Quantitative representation of superiority of CAF over water with respect to environmental friendliness

	Fire $50 \times 50\ m^2$		**Fire $100 \times 100\ m^2$**	
	Water	**CAF**	**Water**	**CAF**
Total amount of water $[m^3]$	3750	2625	15000	10500
Amount of run/off $[m^3]$	1875	1312	7500	5250
Surface area covered by run-off $[m^2]$	18750	13120	75000	52500

Although the values represented in table 5.9 are only rough approximations, there would be no doubt that the substitution of water with CAF as the extinguisher results in a considerable reduction of water usage and consequently the amount of soil should be treated. As estimated in our study, the application of CAF can decrease the polluted area by run-off up to twenty thousand square meters. This can be also considered as an excellent financial benefit that can compensate for the expenses of CAF production. Soil treatment highly demands financial and human efforts. The considerable reduction in the area polluted by run-off is the most important environmental gain of CAF over water. This point can be even more important for fire scenarios happening in the area of coarse-textured soils when there is a very short traveling time for pollutants to reach the groundwater. As simulation results indicate, the polluted water can reach the water table in less than one day for coarser-textured soils. This makes the situation extremely tough or even impossible to cure a huge volume of soil in such a short duration. The application of CAF has remarkable merit in this regard due to the huge reduction in the area under treatment after extinguishment, especially for very large scale fires.

Before closing the chapter, it would also be worthy to assign a brief discussion about the chemical surfactant existing in the foam concentrate which has arisen some environmental concerns about the application of CAF. The compressed air foam technology was initially developed for class B fires (flammable liquids). The foam concentrate of the class B foams includes fluorinated compounds that are accumulative and toxic. The production of fluorinated foams was already banned in Europa due to environmental impacts. However, the subject of this study is the environmental impact of class A foams. The chemical detergent in the class A foam is mostly hydrocarbon or natural protein which are biodegradable. The foam used for our small scaled tests was examined by one of our partners in this project in terms of biodegradability. According to them and also what already claimed by the manufacturer, the foam lifetime in the soil is about 28 days and the chemical surfactant is biodegradable.

However, even regardless of the biodegradability of the chemical detergent in the class A foam, this detergent cannot be considered as a threat to the environment. First of all the percentage of the foam concentrate in the class A foam solution is very low (maximum 1 %) in contrast to class B foam solutions which contain between 3 to 6 % of foam concentrate. Secondly, the chemical surfactant is a hydrocarbon at relatively low concentration compared to other devil components in the run-off. The run-off is susceptible to carry a vast amount of various pollutants and of course a lot of carbon compounds such as polycyclic aromatic hydrocarbons (PAH). The addition of some more little amount of hydrocarbon to the run-off because of the foam concentrate is totally negligible compared to the substances carried from the fire. Therefore, the foam solution of class A foams can be considered environmentally harmless.

All in all, our experiments described in the previous chapter and numerical simulations of this chapter acknowledge the absolute superiority of CAF over water in regard to the soil pollution and risk of endangering groundwater.

6 Smoke Plume Dispersion

The main scope of this chapter is to provide a fire hazard analysis in terms of non-thermal hazards. Non-thermal hazards can be defined as hazards that are caused by the contribution of fire products and not the heat. Smoke is a general term for all the products emitted from the fire. Smoke consists of various toxic, corrosive and odorous compounds that cannot be easily characterized. There are diverse aspects of non-thermal hazards such as asphyxiation, irritation, corrosivity and reduction of visibility. However, the main issue before performing a fire hazard analysis in safety engineering is to define the concerned target regarding which the hazard analysis is to be conducted. The criterion for analysis in this contribution is the irritation of smoke that affects human life in various ways based on the intensity of exposure; from unpleasant feeling to death. Most of the time asphyxiation is not the case that happens in open fires except in some special scenarios like the occurrence of inversion layer very close to the surface.

Smoke dispersion modeling is the tool used to predict the fate of the smoke plume and quantitatively investigate its influence on the quality of air. The two main factors affecting the plume behavior are the atmospheric condition (atmospheric stability class) and smoke composition which depend on the physical and chemical properties of the burning material. Therefore, the data about both of these factors are necessary for the numerical simulation. In this section, the effect of different atmospheric conditions on the smoke plume for both fire scenarios of $50 \times 50\ m^2$ and $100 \times 100\ m^2$ is discussed. Accordingly, conclusions about the strategy and approach facing the scenario are drawn; either to let the fire continue burning or to extinguish it.

Smoke components

The American Society for Testing and Materials (ASTM) defines smoke as the cloud including evolved gases and aerosols emitted during a fire (flaming or smouldering) [127]. A significant practical difficulty in smoke analysis is to provide information about the size distribution of the particulates in smoke. Measurement and determination of the size distribution of the aerosols in smoke are even controversial in the laboratory. Therefore, it is not practically feasible to fulfill this task for every fire scenario simulation. Generally, safety engineers consider soot (particles) as a continuous fluid phase but with a high density (density of solid carbon) in order to skip the difficulties in dealing with the characterization of the particle sizes. This was also the approach in this study to characterize smoke [141].

Another essential problematic issue regarding smoke characterization is the identification of the smoke ingredients. The occurrence of chemical compounds in the smoke is to some extent stochastic and scenario dependent. There are always some main products resulting from specific burning material, but many products also undergo decomposition or react with oxygen or other molecules after production. So, it is also another impossibility to recognize exactly all the components taking part in the smoke. However, there should be an estimation of the smoke composition in order to define the physical properties of the plume. The most significant factor, that determines which substances appear in the smoke, is the nature of the burning material. As mentioned in chapter 4, the burning material in our experiments consists of wood, PP, PU, PVC, and PE. Therefore, the smoke is a combination of the main combustion products of these fuels.

In our tests, the FTIR device was used to measure the smoke composition but only at one measuring point which is not sufficient at all to be relied on in terms of volume fraction of each component. The main benefit of the usage of the FTIR device was to show which compounds are the main participants in the smoke plume. The FTIR showed carbon dioxide (CO_2), carbon monoxide (CO), hydrogen chloride (HCl), methane (CH_4) in all the tests as the main products of the fire. However, it should be noticed that soot is an inevitable product of combustion of any solid fuel that includes hydrocarbon but FTIR is not able to measure the soot concentration. On the other hand, the volume fractions measured by FTIR during different tests cannot be considered as reliable inputs for simulation due to measurement based on one single point. Therefore, the volume fractions of the components were calculated by yields of combustion products according to the equivalence ratio which are provided in the fourth chapter of the third section in the Handbook of Fire Protection Engineering [135]. The procedure is presented in Appendix B.

Atmospheric conditions under investigation

As described earlier, atmospheric stability is the other crucial factor affecting the smoke plume dispersion. The implementation of atmospheric stability in the CFD software is mainly done by the wind velocity field and thermal vertical gradient in the air. It should be noticed that the thermal stratification of the atmosphere and wind velocity are not independent of each other in reality. This implies the fact that the temperature distribution in the atmosphere is the result of wind velocity field and the solar energy from the sun but in CFD simulations, velocity and temperature fields are initially defined by the user and it is important to set up the wind velocity field for each stability class with its corresponding temperature field. However, the CFD simulation is highly sensitive to the velocity field but not that much to the temperature field. This issue will be deeply discussed later in the error analysis section. The velocity field was described via the power-law wind velocity explained in detail in chapter 3 and the atmospheric classification was according to Pasquill-Gifford.

$$u = u_{10}\left(\frac{z}{10}\right)^{p} \tag{6.1}$$

Table 6.1: Atmospheric conditions under investigation

Stability Class	u_{10}	p	ΔT per $100m$
Stable	1	0.55	1.5
Unstable	1	0.07	-3
Slightly stable	3	0.35	-0.5
Moderately unstable	3	0.1	-1.5
Neutral 5	5	0.15	-1
Neutral 8	8	0.15	-1
Inversion	0.3	0.55	+4

Simulation setup

The ANSYS FLUENT was the CFD software used in this study in order to model the turbulent air dispersion. The smoke plume dispersion modeling was divided into two steps; steady and transient. The first step (steady-state) was just to solve the velocity field without adding the smoke to the domain. This step was performed to provide the horizontal homogeneity of the wind velocity. The solution of the first steady-state simulation (domain with horizontally homogenous velocity field) was used as the initial condition for the next step of the simulation. In the next step, the smoke entered the domain. This step was transient due to the high temperature difference between the plume and the atmospheric air. This significant temperature difference resulted in remarkable buoyancy forces and continuous thermal and mechanical interactions between the plume and atmospheric air. Therefore, this part of the simulation was time-dependent and could not be simplified to steady-state. According to the approach selected to deal with the aerosols (considering soot as a gaseous phase but with the density of solid carbon), the smoke was assumed as one gaseous phase. Consequently, only one phase flow simulation was conducted.

The other options used for the simulation setup are briefly listed in the following:

- Compressible flow simulation due to the significant density difference
- Density-based solver due to its better compatibility with compressible flows
- Implicit linearization due to its unconditional stability
- Realizable k-epsilon model for turbulence
- Implementation of the gravitational force beside density difference to consider the buoyancy effect
- Application of Species Transport model for modeling of smoke as the mixture of various gaseous compounds
- One phase flow simulation since both air and smoke are in the gaseous phase
- Selection of the ideal gas law for calculation of the density
- Second-order upwind spatial discretization for the flow, turbulent kinetic energy, and turbulent dissipation rate
- The convergence criterion of 10^{-5}

6.1.1 Domain

The aim of the study was to investigate the smoke dispersion up to a distance of 2 km from the source (fire). Due to the occurrence of turbulence in the atmosphere, the smoke propagates in all the directions and the simulation should be 3-dimensional. An important subject in the air dispersion modeling is the domain size in the vertical, lateral and flow directions. There are different criteria for extension of the domain in different directions offered by different authors, out of which the most conservative ones were selected in this study. The domain dimension relationships are based on the height of the obstacle H. Here, the obstacle was the burning material. The fire was assumed as a volume source near the ground (height of 5 m) which releases smoke. The height of the flame is negligible compared to the dimensions of the domain. Also, flame height is not constant during the fire and is affected by many factors. Therefore, assuming fire as a volume source producing smoke is an acceptable assumption. On the other hand, fire dynamics features were not the concern of this job and the main focus is on the effect of atmospheric stability on the plume behavior. In the following, the domain size is briefly explained according to the fire height which is assumed to be five meters ($H = 5\ m$).

The distance between the inflow boundary and the fire should be at least $8H$ ($40\ m$) [128]. This distance was $500\ m$ in our study. The distance between the fire and the outflow boundary should be a minimum $15H$ ($75\ m$) [129, 130] whereas it was $2000\ m$ in this study. This length of $2000\ m$ was not selected just to fulfill the requirement, the aim was to investigate the dispersion of the smoke plume in far distances from the pollution source. The recommended length for the lateral extension of the domain is $5H$ ($25\ m$) [129] and in our simulation, the domain extends laterally to $200\ m$. The criterion for the vertical extension of the domain is quite controversial. Different authors suggested different heights for the domain [131]. However, the strictest criterion is a height of $10H$ ($50\ m$) for the domain and the domain height in our study was $300\ m$. $300\ m$ was chosen for the domain height in this study because of the fact that the 'gradient height' is about $274\ m$ for open rural terrain. As discussed in chapter 3, the wind velocity increases with elevation till the height where the surface friction has no substantial effect anymore on the wind velocity and consequently there is no significant vertical gradient in the velocity field. This height is called 'gradient height'. The fire scenario taken into consideration in our research takes place in an open rural area and the height of the domain had to be more than the gradient height. So, a height of $300\ m$ was considered for the domain. As explained, our domain size fulfills all the conservative criteria mentioned by different authors about dimensions. The geometry is represented in figure 6.1.

The capital letters indicate the boundaries which will be discussed in the boundary conditions section. The geometry is symmetric and figure 6.1 only depicts half of the domain. The domain used for simulation of temperature inversion is different from other stability classes. The height of the domain is much smaller for inversion simulations and the top boundary is different from other stability classes. This will be discussed later in detail.

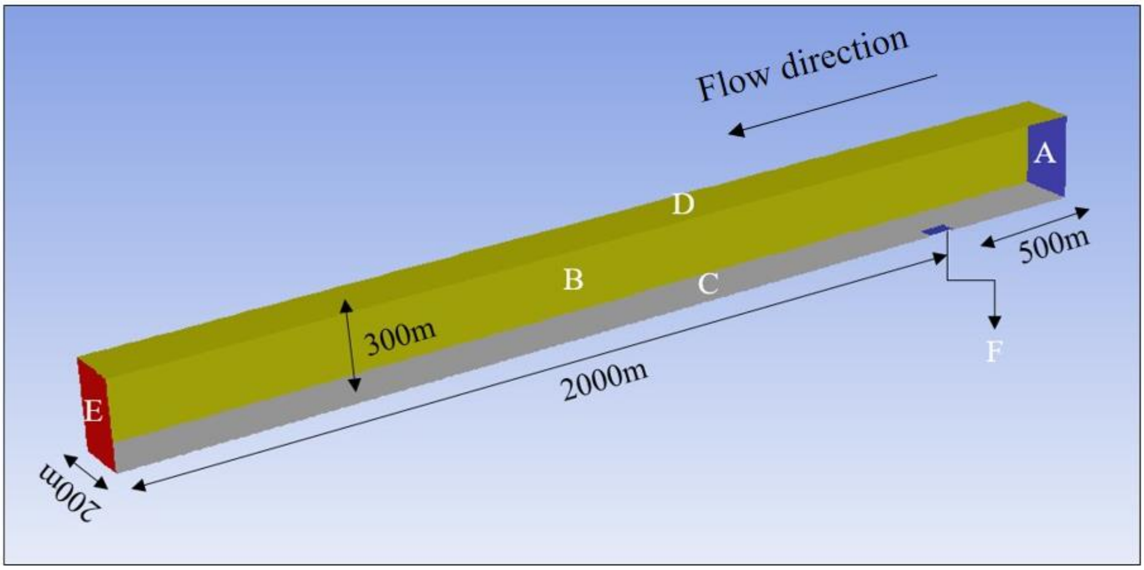

Figure 6.1: Simulation domain

6.1.2 Boundary Conditions

All boundary conditions were selected according to the instructions provided by the practice guideline for the CFD simulation of flows in the urban environment published by Hamburg university [131]. The capital letters A, B, C, D, E and F corresponding to different domain faces (boundaries) were used to name each boundary (figure 6.1).

A: Velocity Inlet

This boundary is the air inlet boundary. The air inlet velocity function was imported to the FLUENT via User Define Function. The velocity function for each atmospheric stability is represented in table 6.1. According to the stability class, the corresponding wind velocity profile was given to the software.

B: Symmetry

The symmetry condition was selected for the side face of the domain.

C: Wall

The no-slip wall condition was used for the ground, meaning the wind velocity at the ground surface is zero. An important characteristic of the wall boundary condition is the surface roughness. Based on the scenario that fire happens in open rural terrain, a value of 0.03 was used for the surface roughness. The roughness values for different lands are available in table 3.4 (chapter 3).

D: Pressure Outlet

The pressure outlet boundary was chosen for the end of the domain in the flow direction.

E: Symmetry

The selection of the top boundary is a controversial task in the dispersion simulation. This boundary is the most important one for sustaining equilibrium in the boundary layer profile and preserving the horizontal homogeneity of the wind velocity. For this purpose, constant shear stress at the top boundary should be established [132, 133]. Otherwise, the inlet wind velocity suddenly decays after the air inlet boundary due to turbulent dissipation and the velocity field near the fire becomes similar for all stability classes independent of the air inlet boundary given to the software. Therefore, there is no criterion to distinguish between different stability classes anymore since the wind velocity is the main indicator of the stability class. The best and most efficient way to deal with the top boundary is to increase the height of the domain in a way that the domain top lies out of the boundary layer. This means that the domain height should be larger than the gradient height where there is no more vertical momentum transfer anymore and the shear stress tends towards zero. Then, the symmetry boundary condition can be used as a fairly accurate representation of this boundary.

F: Mass Flow Inlet

This boundary is the inlet for smoke and the mass flow rate condition was selected for it. As a result, the total mass flow rate of the smoke and mass fraction of each component had to be specified for this boundary. The calculation procedure is described in Appendix B. All the data needed for the smoke inlet boundary condition are represented by table 6.2 for both fires.

The smoke temperature is also needed for this boundary. The temperature above the fire (plume zone) was measured in our small scale experiments. The temperature was nearly 300 $°C$ in all tests. This temperature was used also in the numerical simulation as the temperature at the smoke inlet boundary. If the smoke temperature is much higher, the unburnt hydrocarbons start to burn and also temperatures less than 300 $°C$ at the flame boundary is rare or impossible. However, the effect of smoke inlet temperature on the plume fate will be discussed later in the error analysis section.

Table 6.2: Smoke inlet boundary conditions

	Fire 50×50	**Fire 100×100**
x_{CO_2}	0.167	0.17
x_{CO}	0.037	0.036
x_{CH_4}	0.0315	0.030
x_{HCl}	0.0084	0.0082
x_{soot}	0.0125	0.0123
$\dot{m}_{smoke}$	$113 \frac{kg}{s}$	$457 \frac{kg}{s}$
T	$300°C$	$300°C$

Initial Condition

Smoke dispersion modeling had two steps. The first step was the steady-state solution of the velocity field to produce the horizontally homogenous velocity field in the domain. The solution of this step was used as the initial condition for smoke dispersion simulation. This was the most significant part of the simulation to establish the same velocity field in the whole domain as the velocity function in the air inlet boundary which was given to the software by User Define Function. Choosing the symmetry boundary condition for the top boundary fulfills this circumstance but as explained earlier, the symmetry boundary condition for the top boundary is a true assumption only if the height of the domain is more than the gradient height. In other words, the height of the domain should be large enough so that the top boundary lies in the region where there is no vertical gradient in the wind velocity and zero shear stress (symmetry) assumption is applicable.

To examine the horizontal homogeneity of the velocity field in the flow direction, the x-velocity plots are compared at different distances from the beginning of the domain (200, 1000 and 1500 m). Figure 6.2 proves that the wind velocity is nearly the same as the inlet air velocity ($x = 0$) in all the cross-sections. This implies the fact that horizontal homogeneity of the wind velocity was obtained. Figures 6.2 is for the simulation case of Neutral 8. However, the same procedure was applied to all other cases.

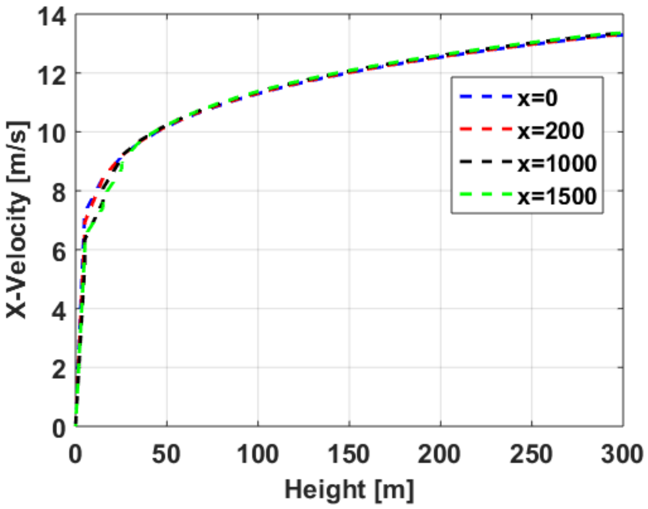

Figure 6.2: x-velocity at different cross-sections

Smoke plume behavior

The identification of smoke is a crucial issue that should be first clarified before analyzing the smoke plume. The critical concentration of smoke according to which the hazards analysis is performed is dependent on the objective of the analysis. In other words, the target of the analysis determines the criterion for the identification of smoke. As explained at the beginning of the chapter, the aim of hazard analysis in this study was the investigation of non-thermal hazards. There are various types of non-thermal fire hazards that affect human life. However, the most important ones are asphyxiation and irritation.

Asphyxiation is normally not the case happening in open fires due to the fact that asphyxiation does not only depend on the concentration of the asphyxiants but also on the exposure time. During huge fires, people stay at home closing all the windows till the excavation process starts by firefighters or they run away from the affected area. The only scenario for which asphyxiation risk should be noticed is the occurrence of temperature inversion in the atmosphere (worst case scenario) which will be discussed later in the inversion section. Therefore, smoke irritation is the most important non-thermal hazard that impacts human life in case of open fires. In contrast to asphyxiation, irritation occurs immediately upon the exposure and does not depend on the exposure time but the concentration of the irritants. There are various irritant effects of smoke on humans from mild pain in the eyes and higher respiratory tract to severe lung inflammation and death. Severe irritant effects occur only close to the fire where the concentrations of the irritants are high. Our aim was to consider fire hazards for long distances from the fire where the smoke has no lethal or incapacitating effects anymore but can still be harmful and unpleasant and affect human life. The only irritant gas amoung the fire products in our fire scenario is hydrogen chloride (HCl).

According to the Handbook of Fire Protection Engineering [135], the lower concentration limit for hydrogen chloride to be perceived as an irritant is 10 ppm. This value was selected as the basis for investigation in this study; however, it is a very conservative criterion and counts the largest area affected by smoke. The aim was to compare the behavior of smoke plume from the same fire for different atmospheric stability classes and draw a general conclusion about the worst atmospheric condition. Suppression of the pollutants near the surface and also the longitudinal and transversal transport length scales were the three criteria used to judge the stability classes and determine the worst scenario. The atmospheric conditions that lead to a higher concentration of the pollutants near the ground (in the first 10 m) and establishment of a larger smoke cloud over the area are undesirable.

6.1.3 Fire $50 \times 50\ m^2$

In the following, the smoke plume contours according to the concentration of HCl for different stability classes are depicted. The contours are drawn on the symmetry plane.

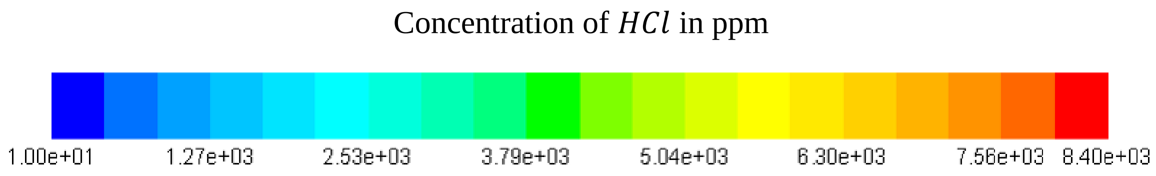

Strongly Unstable:

$$u = 1\left(\frac{z}{10}\right)^{0.7} \tag{6.2}$$

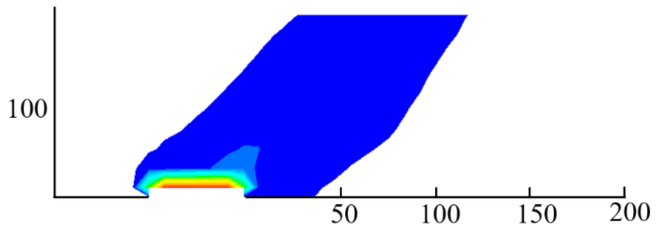

Figure 6.3: Plume shape in the strongly unstable atmosphere

Strongly Stable:

$$u = 1\left(\frac{z}{10}\right)^{0.55} \tag{6.3}$$

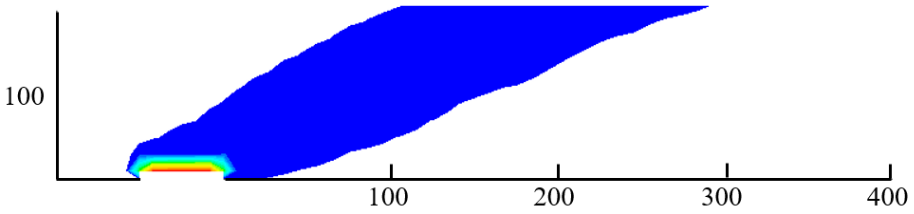

Figure 6.4: Plume shape in the strongly stable atmosphere

Moderately Unstable:

$$u = 3\left(\frac{z}{10}\right)^{0.1} \tag{6.4}$$

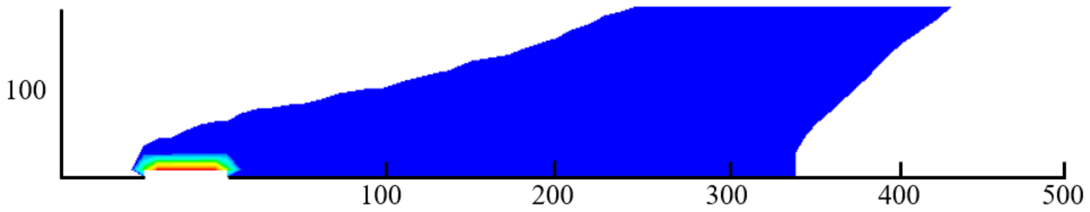

Figure 6.5: Plume shape in the moderately unstable atmosphere

Slightly Stable:

$$u = 3\left(\frac{z}{10}\right)^{0.35} \tag{6.5}$$

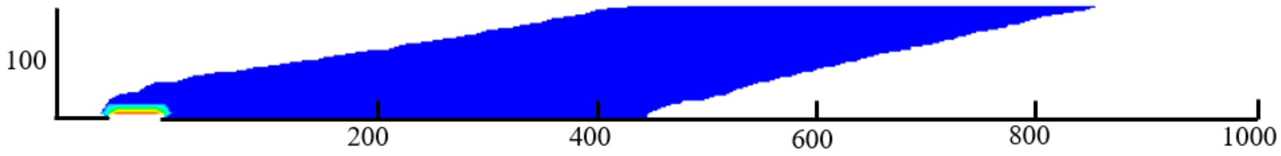

Figure 6.6: Plume shape in the slightly stable atmosphere

Neutral 5:

$$u = 5\left(\frac{z}{10}\right)^{0.15} \tag{6.6}$$

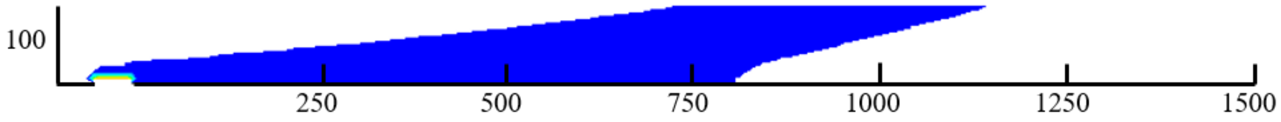

Figure 6.7: Plume shape in the neutral 5 atmosphere

Neutral 8:

$$u = 8\left(\frac{z}{10}\right)^{0.15} \tag{6.7}$$

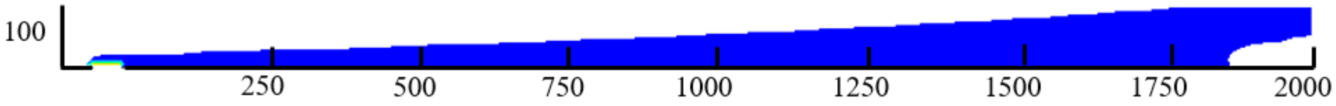

Figure 6.8: Plume shape in the neutral 8 atmosphere

The smoke plume dispersion in the atmosphere is mainly affected by the buoyancy force, due to the huge temperature difference between the plume and the ambient air, and the atmospheric condition (stability class). The stability class is normally classified according to the thermal stratification of the atmosphere and the wind velocity field. The buoyancy force is substantially large because of the large temperature difference, therefore, the smoke tends to go up because of much lower density compared to ambient air. The upward smoke flux due to buoyancy is the dominant flux in calm atmospheres with low wind velocity. Increasing the wind velocity disturbs this upward movement of smoke and suppresses the smoke near the ground.

As is clear in figure 6.3, a strongly unstable atmosphere is the most favorable atmospheric condition. The hot smoke plume goes up easily without any disturbance and the smoke affected area near the ground is relatively small. This is mainly due to very low wind speed in the strongly unstable atmospheres. There are two driving forces for upward movement of the plume in an unstable atmosphere; buoyancy due to the temperature gradient and convective upward air flux due to the thermal stratification of the atmosphere. The contribution of each factor will be discussed in the error analysis section.

In a strongly stable atmosphere, the wind speed is also very low near the ground. In both of these extreme cases (strongly stable and strongly unstable), the wind velocity at an elevation of 10 m is less than 2 m/s according to Pasquill-Gifford. This explains exactly why in these extreme cases the temperature gradient in the atmosphere is considerable, compared to the other atmospheric conditions with higher wind velocity. The wind breaks the thermal stratification of the atmosphere. The temperature gradient in the atmosphere decreases as the wind velocity increases. However, the wind velocity is low near the ground in the strongly stable atmosphere but it increases steeply with height. It can be seen also in figure 6.4 that the smoke plume moves up from the surface because of low wind speed near the ground but make a cloud at higher elevations because of high wind speed which disturbs the upward movement of the plume. So, the plume behavior near the ground in the strongly stable atmosphere is relatively similar to the unstable atmosphere (in both cases u_{10} equals 1 m/s). Therefore, the strongly stable atmosphere, as far as temperature inversion does not occur, is also not a catastrophic condition when it comes to dispersion of hot plume of smoke from a source near the ground. However, there is no guarantee that these rising pollutants do not come back to the surface via either dry or wet deposition.

Increasing the wind velocity slightly ($u_{10} = 3$), reduces the deviation of the temperature gradient in the atmosphere from the adiabatic lapse rate. So, the atmospheric condition deviates from the extreme cases (either strongly stable or unstable) but the wind velocity is still not sufficiently high to destroy the thermal stratification of the atmosphere completely. The terms ‘slightly stable’ and ‘moderately unstable’ were used to name the atmospheric conditions between extreme conditions and neutral atmosphere. In the slightly stable conditions, the wind velocity near the ground is larger than the strongly stable conditions whereas the rate of increase of the wind speed with elevation is smaller. In the moderately unstable conditions, the wind velocity near the ground and the rate of increase of the wind speed with elevation are both larger compared to the strongly unstable conditions. As shown by figures 6.5 and 6.6, both slightly stable and moderately unstable atmospheres result in the accumulation of pollutants near the ground. This is because of the higher wind speed near the ground.

However, for the same value of the wind speed at the elevation of 10 m (u_{10}), the slightly stable atmosphere leads to a larger region near the ground to be affected by smoke and the pollutants are transferred to longer distances in the wind flow direction compared to the slightly unstable condition. Thermal stratification and consequently the vertical wind profile in the unstable atmosphere provide the possibility for the hot plume to rise easier. The atmospheric conditions amenable to the unstable conditions have greater potency for the vertical transportation of the pollutants to higher elevations. The thermal stratification of the unstable atmosphere is in a way that there is always an upward air movement (atmospheric convective cycle) that transports pollutants upward whereas, in the stable atmosphere, there is no upward air flux contributing to the vertical plume transport. However, in the case of hot smoke plumes, the buoyancy force resulted from the temperature difference between the smoke plume and ambient air also plays a considerable role in the upward plume movement which decreases to some extent the importance of atmospheric stability classes. This buoyancy flux is strong enough to oblige the hot smoke to rise up independent of the temperature gradient in the atmosphere. The temperature distribution in the atmosphere can be more noticeable for pollutants with lower temperatures close to ambient air temperature especially when the zone of interest is lower elevations near the ground.

Wind velocities larger than 5 m/s break the thermal stratification of the atmosphere completely and the temperature gradient in the atmosphere tends to adiabatic lapse rate. This implies the fact that there is no external force on the plume because of the temperature distribution in the atmosphere. As a result, the main driving force for the upward movement of the hot smoke plume is its lower density compared to ambient air (buoyancy force). Increasing the wind velocity reduces the significance of the buoyancy force due to the fact that the high wind velocity strongly disturbs the upward plume movement due to the buoyancy. Therefore, the smoke cannot rise up and accumulates near the ground surface. As illustrated in figure 6.7 and 6.8, a neutral atmosphere is the worst possible atmospheric condition compared to the other situations (except temperature inversion) in terms of suppression of pollutants near the ground. The comparison of neutral 5 and neutral 8 reveals the fact that the higher the wind speed is, the more area near the ground is affected by smoke. It should be mentioned again that all these arguments discussed above are only valid when the source of the pollutants is near the ground with much higher temperature compared to the ambient air. The identification of the worst atmospheric condition regarding air pollution depends strongly on the characteristics of the pollution source. Here for the hot fire plume, the neutral condition can be recognized as the worst case unless there is a temperature inversion in the atmosphere which is susceptible to create even more catastrophic situations compared to the neutral atmosphere. However, the worst atmospheric condition for other pollution scenarios might be different.

According to the discussion above, wind speed near the ground is the most important factor to accumulate airborne fire pollutants near the surface. The following figures (6.9 and 6.10) show the concentration of HCl at elevations of 1 and 5 m for all six stability classes. The horizontal axis shows the longitudinal distance from the fire in the flow direction. The vertical axis represents the concentrations between the maximum value and 10 ppm as the starting point for the irritant effect of HCl. As discussed earlier, 10 ppm of HCl was the criterion selected in this study for the identification of smoke. If the concentration of the HCl is less than this value in a computational cell, the effect and existence of smoke at that location are negligible.

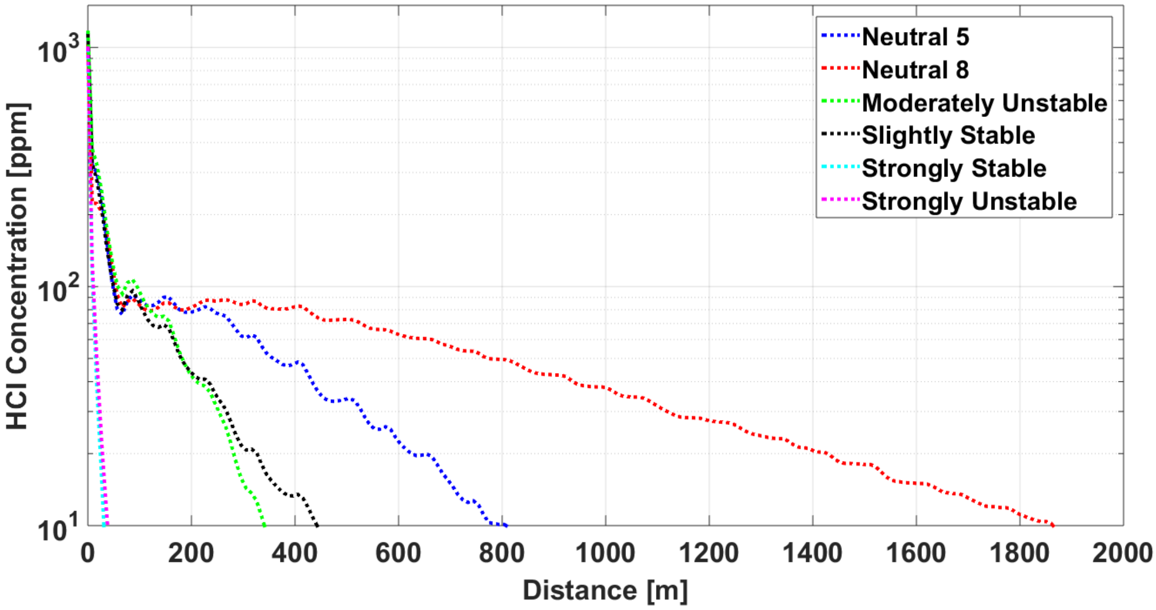

Figure 6.9: Concentration of HCl according to longitudinal distance from the fire at the height of 1 m from the ground

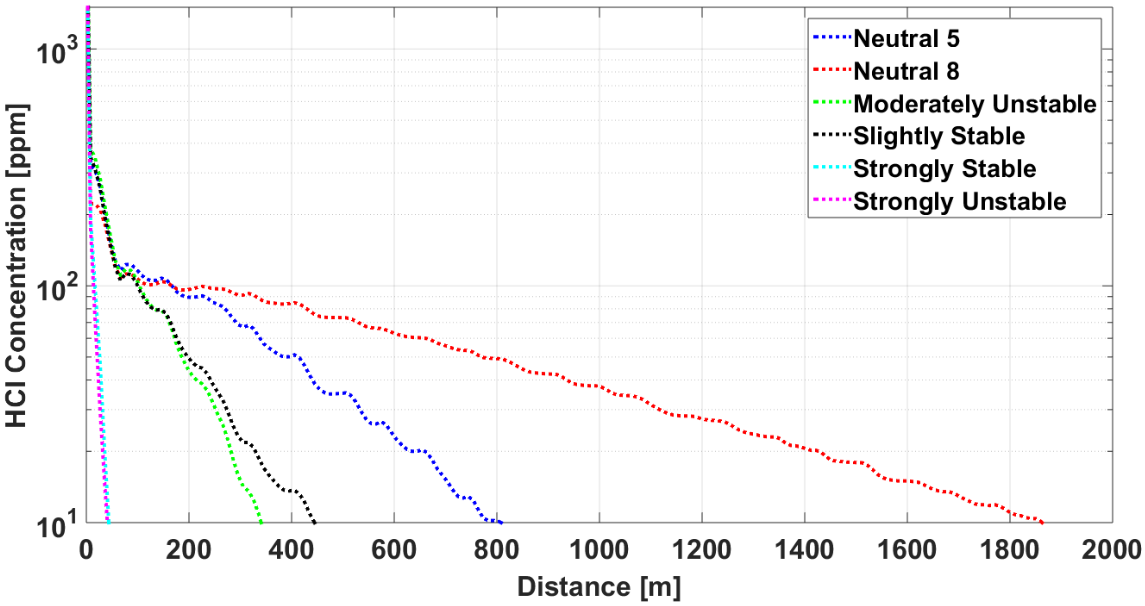

Figure 6.10: Concentration of HCl according to longitudinal distance from the fire at the height of 5 m from the ground

As is evident, both strongly stable and strongly unstable atmospheres show nearly similar behavior near the ground at both elevations of 1 and 5 m. The plume rises up easily and does not stay close to the surface. This is mainly due to the very low wind speed and calm atmosphere near the ground. The fire plume influence is till 50 m in the flow direction and the concentration of the HCl drops below 10 ppm after that, meaning that there is no unpleasant irritant feeling after about 50 m at lower elevations near the ground.

The other stability classes lead to nearly the same results close to the fire (first 100 m) and deviate from each other at larger distances. HCl at concentrations of 100 ppm or more has excruciatingly irritant effects on the eyes and respiratory tract. For slightly stable, moderately unstable, neutral 5 and neutral 8 atmospheres, the HCl concentration is more than 100 ppm in the first 100 m from the fire. This area is extremely irritant and intolerable for human beings. HCl concentrations between 50 and 100 ppm are still strongly irritant, especially for sensitive people. This strong irritant effect can be felt until about 200 m from the fire when the atmosphere is either slightly stable or moderately unstable. The distance from the fire over which the strong irritant effect of the smoke can be percieved for neutral 5 and neutral 8 atmospheres, is 400 and 800 m respectively. Although HCl at concentrations of less than 50 ppm is not strongly irritant and even working is possible but still, irritation can be felt and has an unpleasant effect especially when it stays for a long time.

The distance from the fire over which the irritant effect of smoke is present can be up to 2 km far from the source (fire) depending on the wind velocity. The higher the wind speed is, the longer the distance from the fire is affected by the smoke irritant effect. It should be noticed that the data for these graphs were captured from imaginary lines plotted in the symmetry plane at different heights of 1 and 5 m. The above graphs in figures 6.9 and 6.10 provide information about the longitudinal pollutant transport in the main flow direction but do not say anything about the lateral pollutant transfer and the area influenced by the smoke plume. To analyze the lateral plume dispersion, the concentration contour was plotted on an imaginary surface at the elevation of 1 m from the ground (figure 6.11). It is clear that the smoke affected area is quite narrow and the maximum width is a little more than 100 m. It can be explained by the fact that the plume becomes dilute rapidly by wind flow in the open fires. The mass fraction of HCl at the smoke boundary is 8400 ppm and as figures 6.9 and 6.10 show, it drops rapidly to below 100 ppm after 100 m. Dilution of the plume by wind is the reason why smoke does not spread laterally.

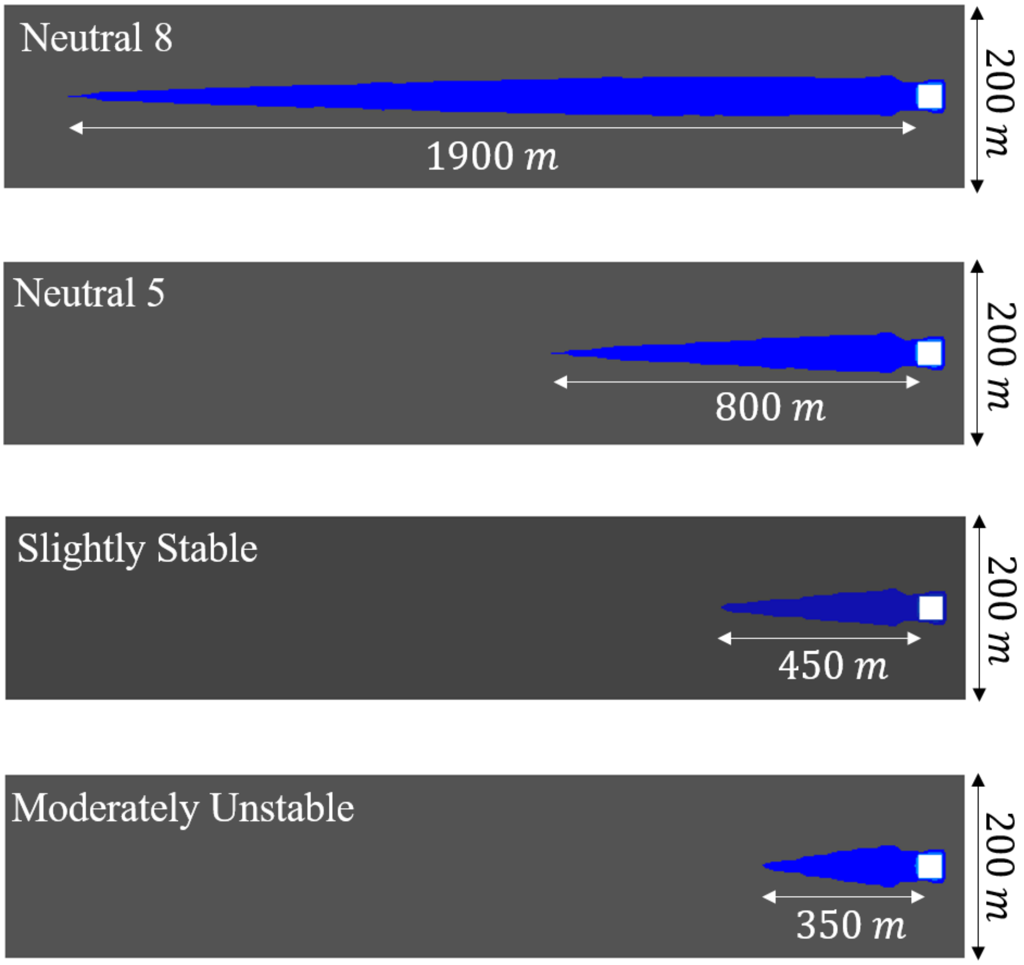

Figure 6.11: Smoke affected area at the heighit of 1 m from the ground

According to figure 6.11, the average affected area by the smoke can vary approximately between $70 \times 350\, m^2$ for the slightly unstable atmosphere (minimum affected area) and $100 \times 1900\, m^2$ for the neutral 8 condition (maximum affected area). This is a relatively huge area near the ground (at a height of $1\, m$) besides the fact that these simulations were based on the assumption of constant wind velocity field during the fire. The atmospheric stability changes continuously during the day and the smoke plume does not have a constant shape during the whole time. The wind direction changes randomly and the smoke plume spreads in all directions. However, it does not change the main outcome that claims the main factor leading to the suppression of pollutants near the ground is the wind speed close to the ground when the pollutants are released from a source near the ground with much higher temperature compared to the ambient air.

6.1.4 Fire $100 \times 100\, m^2$

In the following, the smoke plume contours according to the concentration of HCl for different stability classes are depicted. The contours are drawn on the symmetry plane.

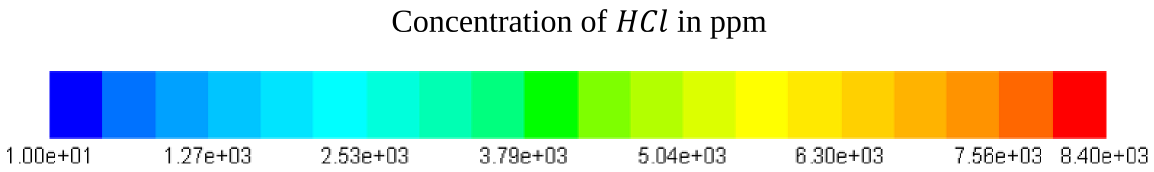

Strongly Unstable:

$$u = 1\left(\frac{z}{10}\right)^{0.7} \tag{6.8}$$

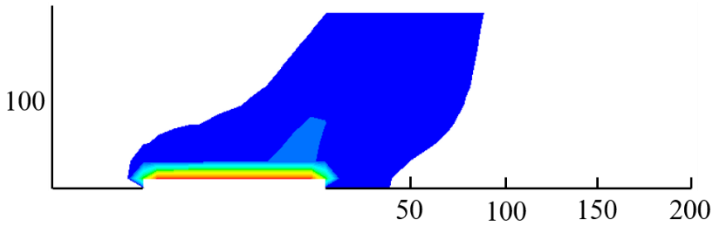

Figure 6.12: Plume shape in the strong unstable atmosphere

Strongly Stable:

$$u = 1\left(\frac{z}{10}\right)^{0.55} \tag{6.9}$$

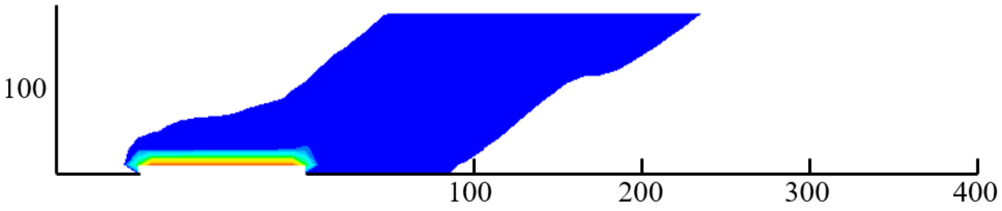

Figure 6.13: Plume shape in the strongly stable atmosphere

Moderately Unstable:

$$u = 3\left(\frac{z}{10}\right)^{0.1} \tag{6.10}$$

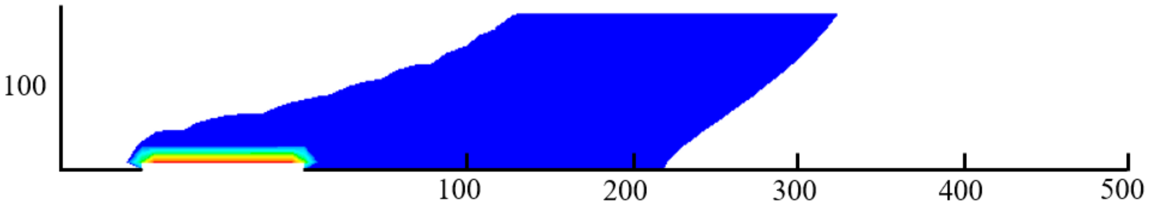

Figure 6.14: Plume shape in the moderately unstable atmosphere

Slightly Stable:

$$u = 3\left(\frac{z}{10}\right)^{0.35} \tag{6.11}$$

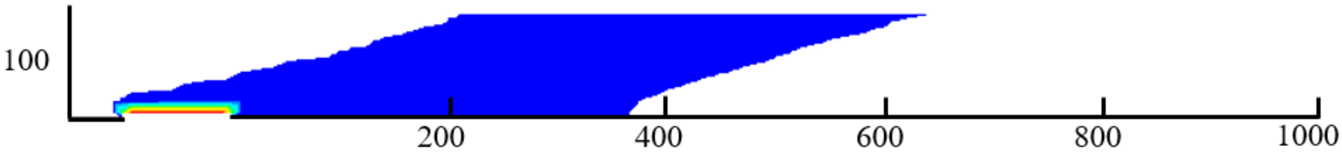

Figure 6.15: Plume shape in the slightly stable atmosphere

Neutral 5:

$$u = 5\left(\frac{z}{10}\right)^{0.15} \tag{6.12}$$

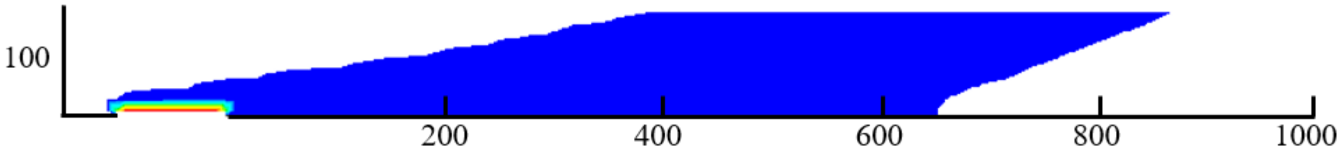

Figure 6.16: Plume shape in the neutral 5 atmosphere

Neutral 8:

$$u = 8\left(\frac{z}{10}\right)^{0.15} \tag{6.13}$$

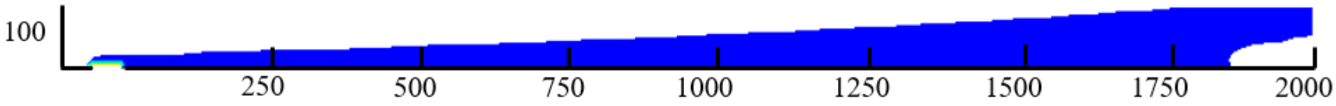

Figure 6.17: Plume shape in the neutral 8 atmosphere

All the things which were discussed about the atmospheric stability classes for the fire $50 \times 50\ m^2$ in the previous section are true for the fire $100 \times 100\ m^2$ as well. The only difference is that the fire $100 \times 100\ m^2$ releases much more airborne pollutants because of the higher rate of smoke production. The results from the simulation of the fire $100 \times 100\ m^2$ also approve that a neutral atmosphere is the worst case scenario due to the higher wind velocity near the ground. The hot plume tends to go up due to the large buoyancy force and the wind speed is the only factor that can break this buoyant flux and keep the pollutants near the ground surface. At lower wind velocities (calmer atmospheres), different stability classes show discrepancies with respect to dispersion of the plume at higher elevations but not near the ground when the plume has a much higher temperature compared to the ambient air. This is due to the fact that when the wind speed is low near the ground, the hot plume rises easily and does not stay at the surface. Figures 6.18 and 6.19 show the concentration of HCl according to the longitudinal distance from the fire in the wind direction at different heights of 1 and 5 m from the ground. As explained in the previous section, it can be seen again that the concentration curves for strongly unstable and strongly stable atmospheres drop rapidly below 10 ppm in less than 100 m from the fire. However, increasing the wind speed near the ground (moving towards the neutral atmosphere) leads to the accumulation of the pollutants near the surface. A higher wind velocity near the ground means a greater accumulation of pollutants near the surface.

Although all the simulations argued in this chapter are transient simulations, the plume reaches a steady state after about 15 minutes in all the cases. In the beginning, the domain was just occupied by air and the initial concentration of all other components was zero. Afterward, the smoke entered the domain. The hot smoke rose continuously due to buoyancy but after some time, the plume shape became constant and did not change with time anymore. This happened because of the steady wind velocity field.

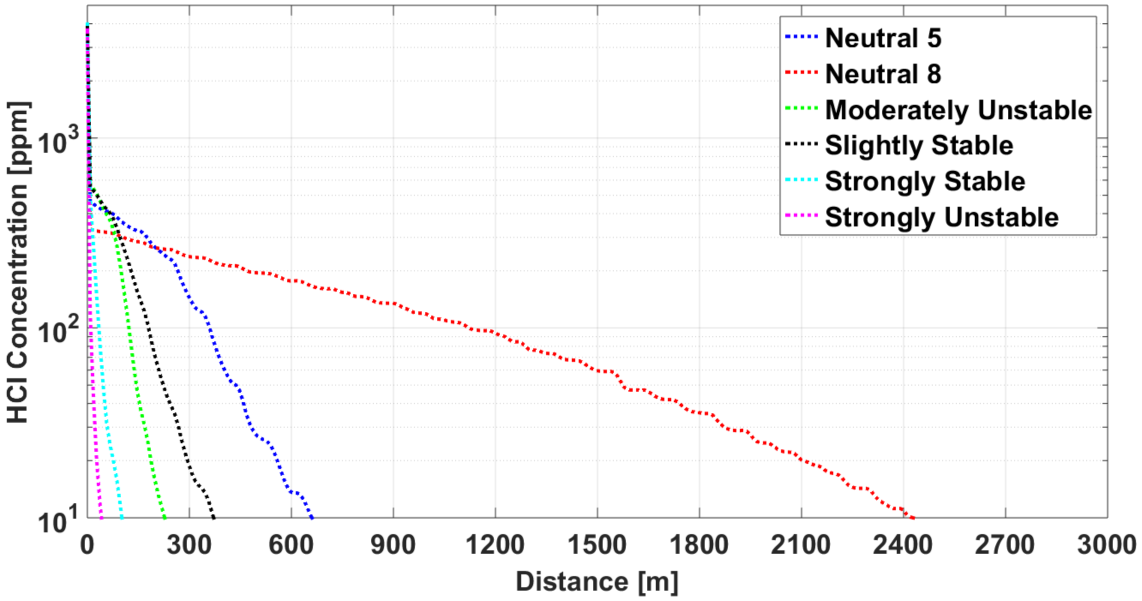

Figure 6.18: Concentration of HCl according to longitudinal distance from the fire at the height of 1 m from the ground

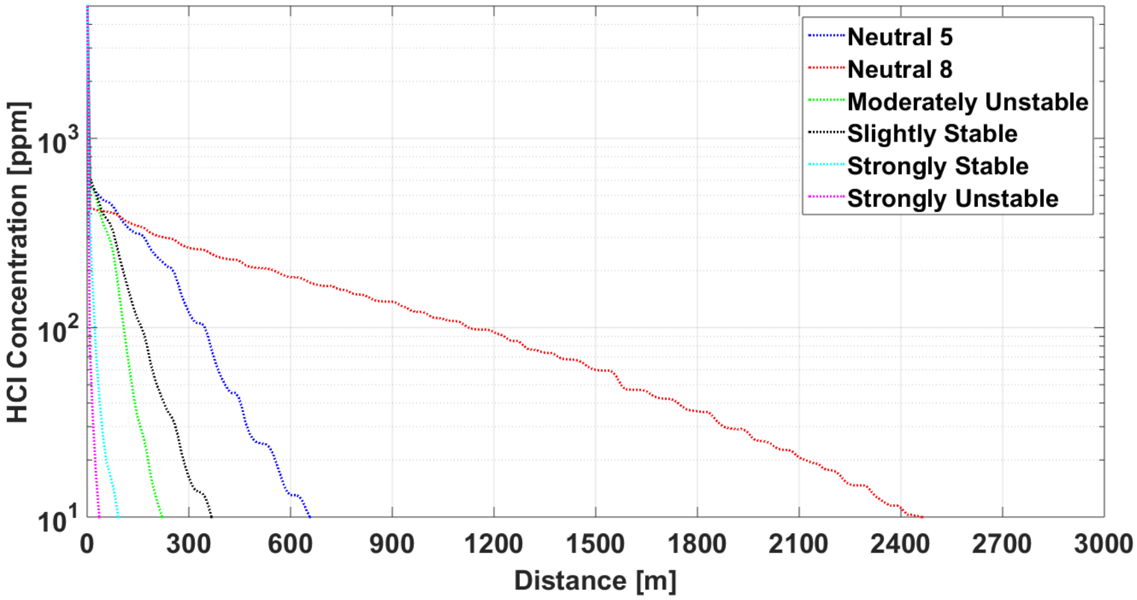

Figure 6.19: Concentration of HCl according to longitudinal distance from the fire at the height of 5 m from the ground

6.1.5 Inversion

As mentioned in chapter 3, the closest capping layer to the surface happens during the ground-based inversion. Other types of inversion create the capping layer at higher elevations. Based on the fact that the scope of this study was the investigation of the worst scenarios with respect to air pollution, only the lowest heights of the mixing height will be discussed. Practically, the inversion layer might happen at any height from the surface. Many studies [136-138] have focused on the inversion height based on the meteorological data at different places in the world. Even at one certain place, the inversion height varies over a considerable range in a year (from one month to another one). However, none of these studies mentioned inversion height lower than 100 m from the surface. So, a height of 100 m was one of the elevations considered in this study. It should not be neglected that the mentioned studies were mostly conducted in the urban areas. The mixing height over urban terrains is always larger than rural terrains. This is mainly due to the higher surface roughness of the urban areas and consequently, a higher degree of turbulence, larger atmospheric boundary layer and mixing height. The inversion height in rural terrains can be even as low as 50 % of its value in the urban areas. The fire scenarios discussed in this contribution take place in a rural area. Therefore, height 50 m was also investigated for the height of the capping layer during the ground-based inversion. Although the frequency of occurrence of the capping inversion layer at these elevations (50 and 100 m) is low, it is still possible to happen according to meteorological data.

In contrast to other atmospheric conditions that only result in the irritation effects of smoke near the surface, the occurrence of temperature inversion at the time of fire accident can lead also into incapacitative effects (asphyxiation) of smoke near the ground. Carbon monoxide is the main asphyxiant produced by a fire. In contrast to the irritation effect of the smoke, which happens immediately upon the exposure, asphyxiation depends on the dose of the toxicant. This implies that to discuss the asphyxiation effects, the concentration of the asphyxiant and the exposure time are both taken into consideration. The most used method for toxicity assessment based on asphyxiation is the 'Fractional Effective Dose' model proposed by Hartzell [139]. The modified form of the equation to assess the incapacitative effect of the carbon monoxide is written as following [135]:

$$F_{I_{CO}} = \frac{K(ppmCO^{1.036})(t)}{D} \tag{6.14}$$

Where $F_{I_{CO}}$ is the fraction of incapacitating dose which equals 0.3 for the beginning of incapacitation, t is exposure time, K is constant equals 8.2925 E-4 and D is COHb concentration at incapacitation which equals 30 %. Therefore, to calculate the critical concentration of the carbon monoxide resulting in incapacitation, the exposure time should be known. During the large fires, people mostly stay indoor until the excavation process is carried out by fire-fighters. So, to consider the worst scenario, the longest possible exposure time which results in the lowest critical concentration of carbon monoxide is selected to be investigated. The longest exposure time is assumed 30 minutes. The critical concentration of the carbon monoxide resulting in incapacitation for a normal person after 30 minutes of exposure is 285 ppm according to equation 6.14.

As mentioned earlier, the domain for simulation of inversion was a little different from the other atmospheres. The height of the domain was the height of the capping layer and the top boundary condition was wall instead of symmetry. The width of the domain was 1500 m. The other characteristics are the same as other simulations. In contrast to other atmospheres, the plume did not reach a steady state under temperature inversion condition. The plume spreads as long as the inversion lasts and did not reach a constant shape after some time. In this study, the simulations were conducted just for 1 hour because the early morning inversion mostly lasts between 45 minutes to 1 hour. However, this study deals with micro-scale meteorology and investigates only till a distance of 2 km from the fire not further but it should be noticed that by continuing the inversion plume goes further.

6.1.5.1 Inversion height of 100 m

Fire $50 \times 50\ m^2$

Figure 6.20 shows that the smoke plume goes up without any disturbance until it reaches the capping layer. The capping layer behaves like a wall and does not let the plume rise up anymore. The smoke plume accumulates below the capping layer resulting in a cloud over the surrounding area.

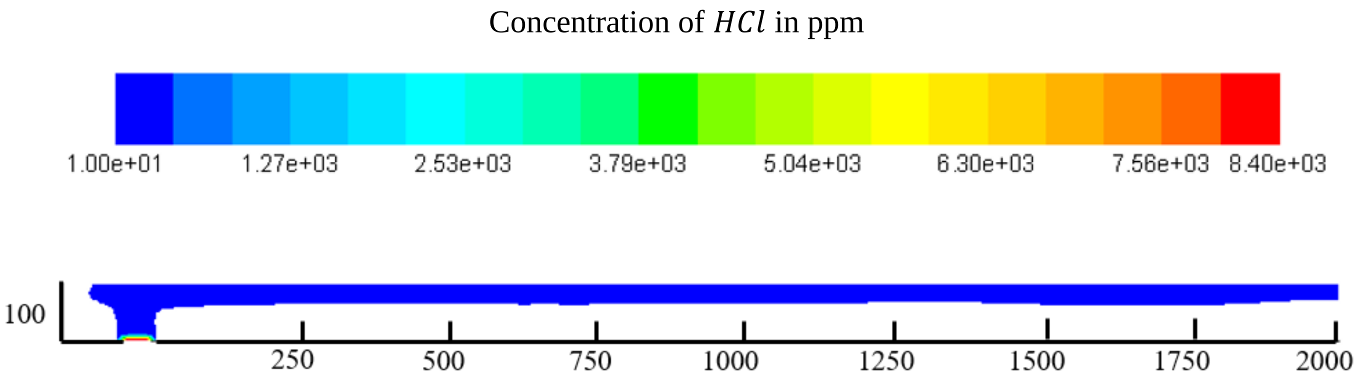

Figure 6.20: Plume shape under the inversion layer at the height of 100 m (Fire $50 \times 50\ m^2$) according to the concentration of HCl [ppm]

Fire $50 \times 50\ m^2$ does not lead to the accumulation of pollutants near the surface but creates a huge cloud over the surrounding area (figure 6.21). A big portion of the accumulated pollutants below the capping layer might come back to the surface.

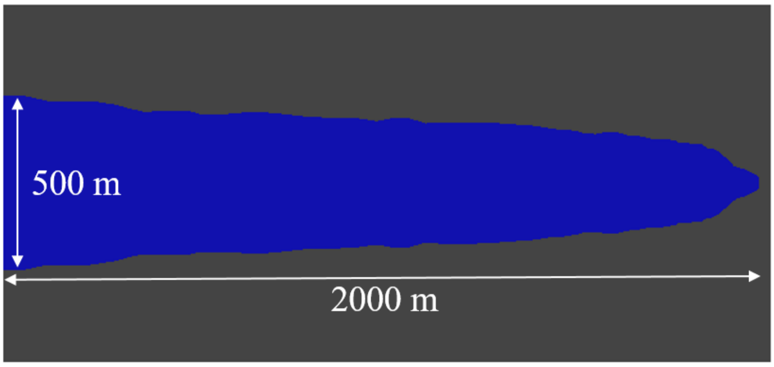

Figure 6.21: Top view of the smoke plume at the height of 100 m

Fire $100 \times 100\ m^2$

The same as fire $50 \times 50\ m^2$ (figure 6.20), the plume rises till it reaches the capping layer; then, the plume spreads horizontally and laterally. The difference is that the fire $100 \times 100\ m^2$ results in the accumulation of the plume also near the surface because of the higher intensity of the pollution source (higher rate of smoke production) compared to fire $50 \times 50\ m^2$. Also, the formed cloud at the inversion height is about 3 times larger than the cloud from fire $50 \times 50\ m^2$ (figure 6.22). However, the same as fire $50 \times 50\ m^2$, fire $100 \times 100\ m^2$ also does not result in any asphyxiation zone near the ground. At the surface, only the irritation effect of the plume can be received.

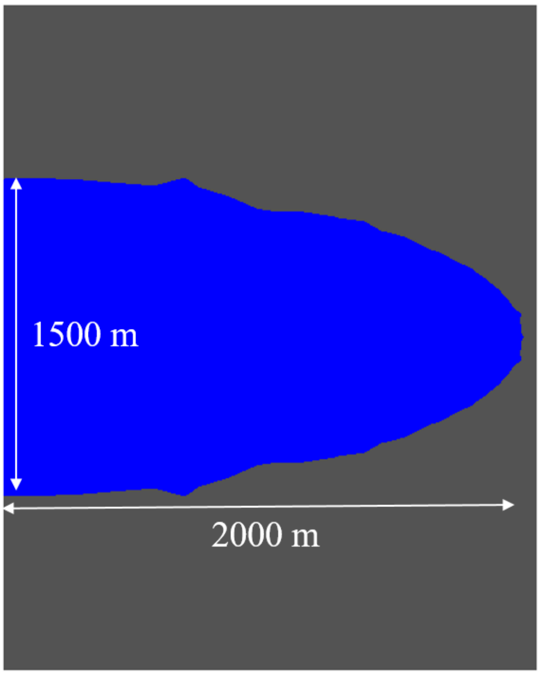

Figure 6.22: Top view of the smoke plume at the height of 100 m

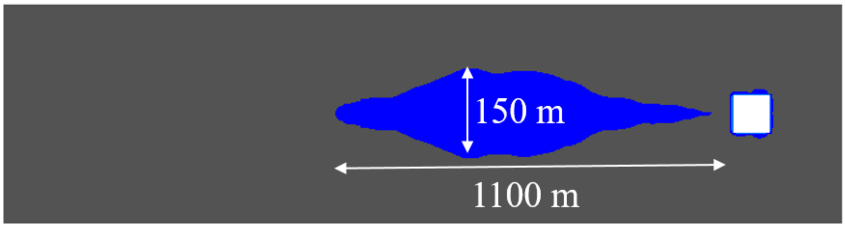

Figure 6.23: Smoke affected area (irritation zone) at the height of 1 m from the ground

6.1.5.2 Inversion height of 50 m

Decreasing the inversion height leads to a larger smoke cloud over the surrounding area and also a larger amount of pollutants accumulated near the surface. Although the occurrence of the capping layer at the height of 50 m from the ground is nearly impossible in the urban terrains due to the higher degree of turbulence and mixing as a result of buildings, it might happen over rural areas where the roughness of the surface is small. The occurrence of the capping layer at such low heights creates also an incapacitation zone near the surface. The maximum exposure time of 30 minutes was chosen for the calculation of the incapacitation zone. However, the incapacitation zone is relatively smaller than the irritation zone but still large enough to be investigated.

Fire $50 \times 50\ m^2$

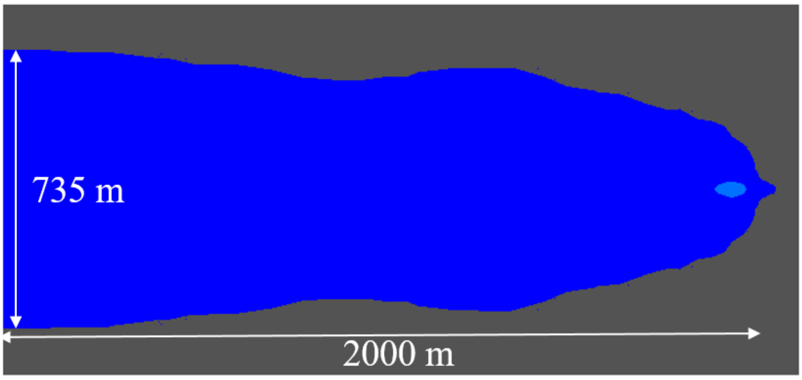

Figure 6.24: Top view of the smoke plume at the height of 50 m

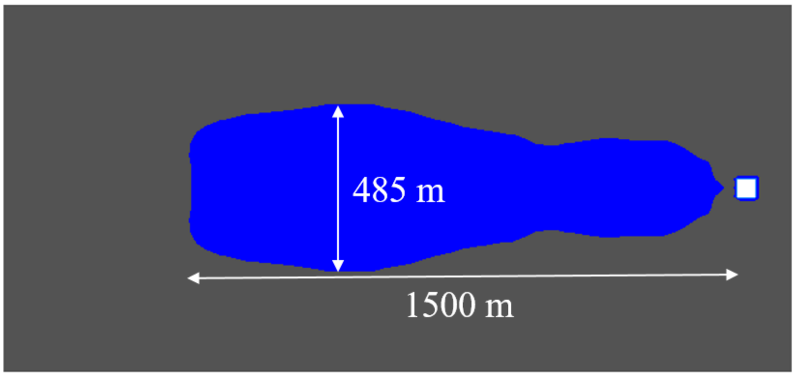

Figure 6.25: Smoke affected area (irritation zone) at the height of 1 m from the ground

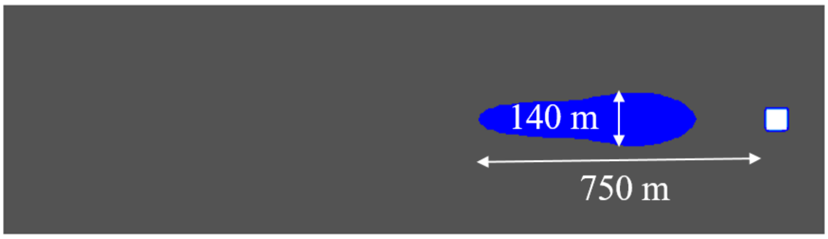

Figure 6.26: Asphyxiation zone at the height of 1 m from the ground

Fire $100 \times 100\ m^2$

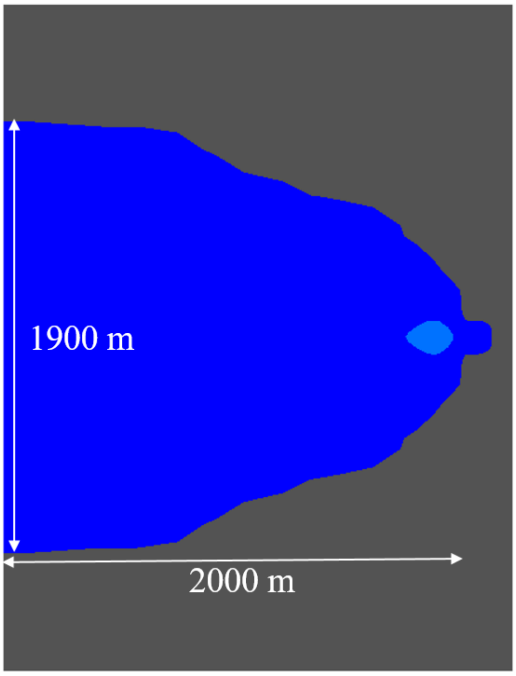

Figure 6.27: Top view of the smoke plume at the height of 50 m

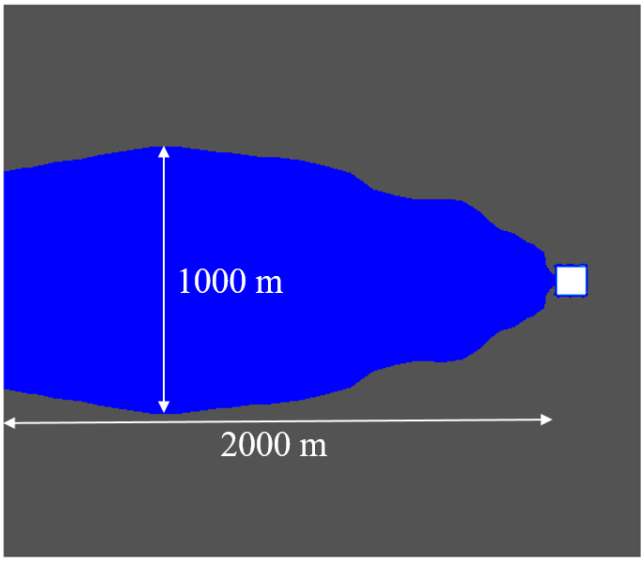

Figure 6.28: Smoke affected area (irritation zone) at the height of 1 m from the ground

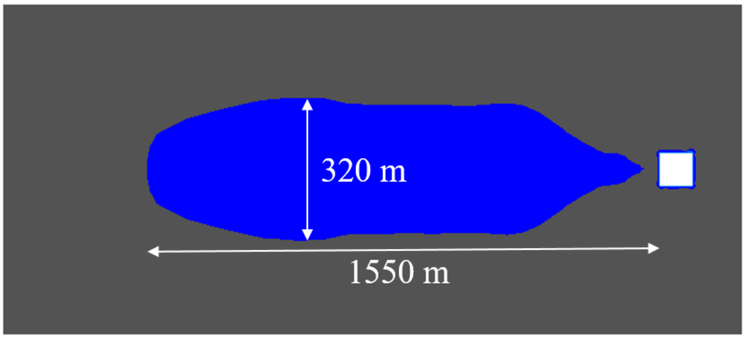

Figure 6.29: Asphyxiation zone at the height of 1 m from the ground

The inversion simulations show that the occurrence of the temperature inversion in the atmosphere is the worst atmospheric condition with respect to air pollution, although the wind velocity is very low. The lower the inversion height is, the worse the atmospheric condition is. When the capping layer is established very close to the ground, it results in a huge zone affected by smoke; both irritation and asphyxiation effects. Although higher heights of the capping layer do not immediately suppress the plume near the ground, the accumulated pollutants below the capping layer (smoke cloud) eventually deposit. During inversion, the smoke plume rises up without any disturbance because of the very low wind velocity. The rising plume reaches the capping layer which acts as a wall and does not let the plume go up further. Then, depending on the scenario (height of the inversion layer and intensity of the pollution source), the plume spreads further.

Error Analysis

Characterization of the factors affecting the smoke dispersion is not very straightforward. A fire has a totally stochastic nature and the smoke properties at the smoke inlet boundary change constantly. However, the main smoke properties which can affect smoke plume dispersion simulation are:

1. The smoke temperature at the smoke inlet boundary
2. Smoke components’ mass fraction at the smoke inlet boundary

The error analysis was just performed for the fire $50 \times 50\ m^2$. The aim was to consider the effect of these parameters (smoke temperature and smoke composition) on the plume dispersion; therefore, there was no need to repeat the analysis also for fire $100 \times 100\ m^2$.

6.1.6 Smoke temperature at the smoke inlet boundary

As explained previously in section 6.4.1, the buoyancy force is the most important driving force for the upward movement of the plume. The factor determining the magnitude of this buoyant flux is the smoke temperature. The temperature of 300 $°C$ was selected for the smoke at the boundary in this thesis according to our experiments. The temperature at the top of the flame of huge fires where smoke initiates can not be less than 300 $°C$. On the other hand, the smoke temperature is not much higher than 300 $°C$ because at higher temperatures the unburnt hydrocarbons in the smoke experience burning and there would be a flame. However, the effect of the smoke temperature at the smoke inlet on the dispersion simulation was investigated by conducting the simulations for different smoke temperatures at the boundary.

Once, all the simulations were performed with the smoke temperature of 600 $°C$ at the boundary to show the influence of higher temperatures on the plume behavior. The second time, the plume at the ambient temperature (25 $°C$) was taken into consideration. Although the smoke temperature is never 25 $°C$, this low temperature was chosen to show that the characterization of the worst atmospheric scenario with respect to air pollution is a case dependent analysis. As will be discussed later, the worst atmospheric condition for low-temperature plume is different from the hot plume. According to the analysis of the plume with low temperature, it is also possible to discuss the importance of the buoyancy in the upward movement of the hot plume in comparison to upward flux due to the vertical momentum of the plume and also the vertical transport due to wind turbulence.

Strongly Unstable:

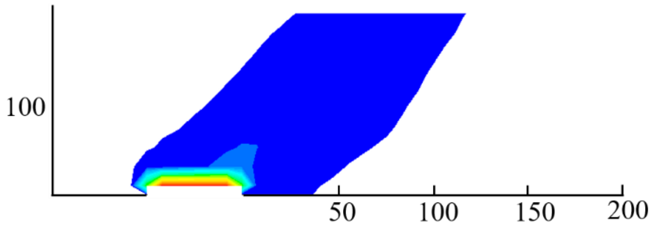

Figure 6.30: Plume shape for the plume temperature of 300 $°C$ at the smoke boundary

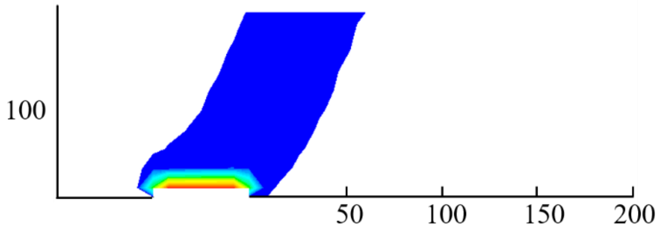

Figure 6.31: Plume shape for the plume temperature of 600 $°C$ at the smoke boundary

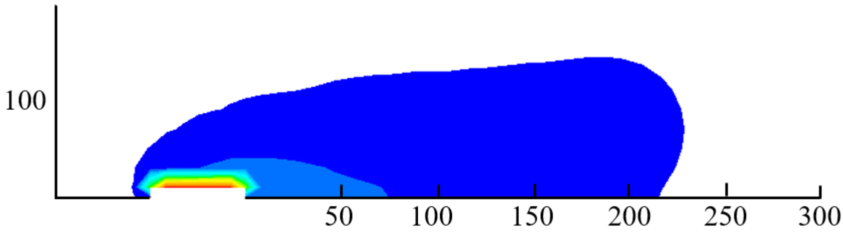

Figure 6.32: Plume shape for the plume temperature of 25 $°C$ at the smoke boundary

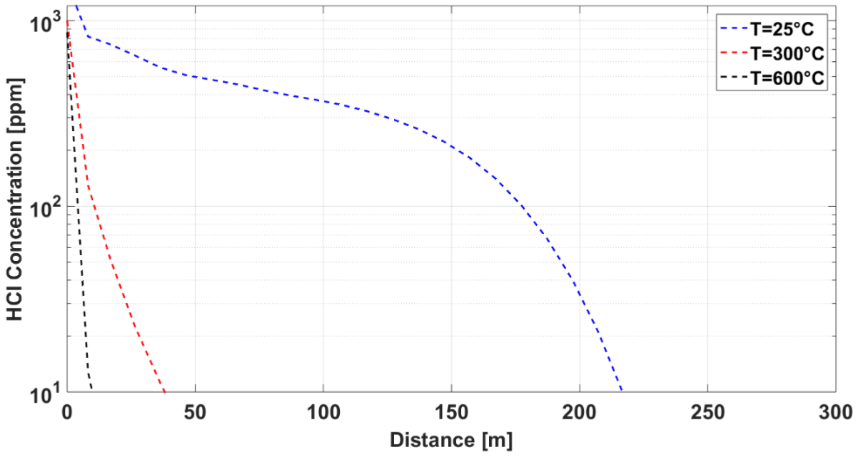

Figure 6.33: Concentration of HCl according to longitudinal distance from the fire

At the height of 1 m from the ground

Strongly Stable

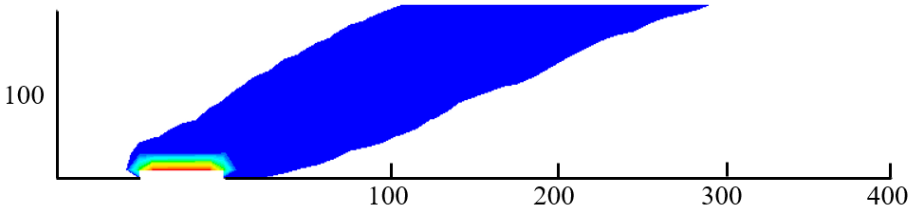

Figure 6.34: Plume shape for the plume temperature of 300 $°C$ at the smoke boundary

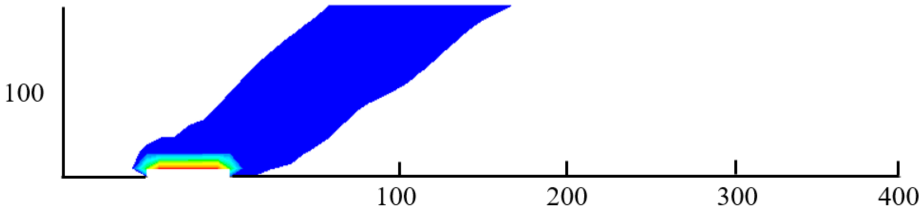

Figure 6.35: Plume shape for the plume temperature of 600 $°C$ at the smoke boundary

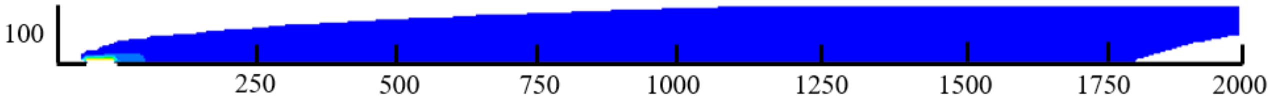

Figure 6.36: Plume shape for the plume temperature of 25 $°C$ at the smoke boundary

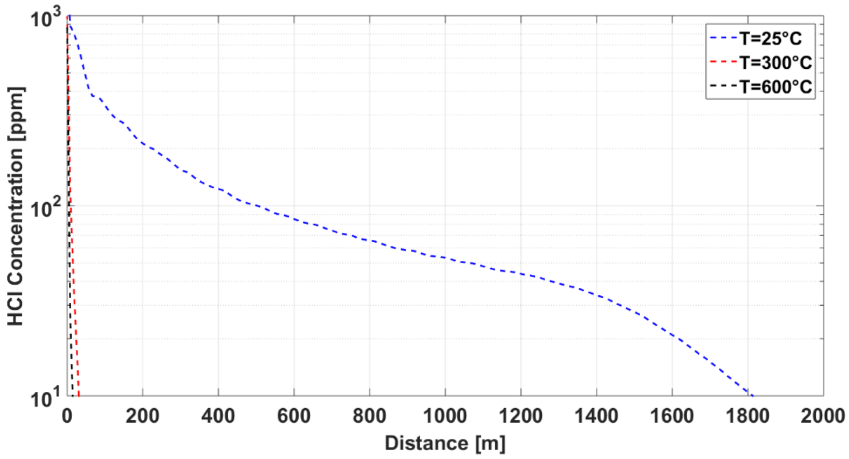

Figure 6.37: Concentration of HCl according to longitudinal distance from the fire at the height of 1 m from the ground (strongly stable)

Moderately Unstable:

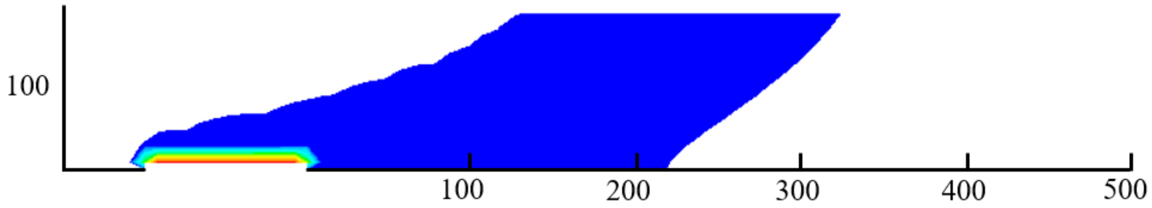

Figure 6.38: Plume shape for the plume temperature of 300 $°C$ at the smoke boundary

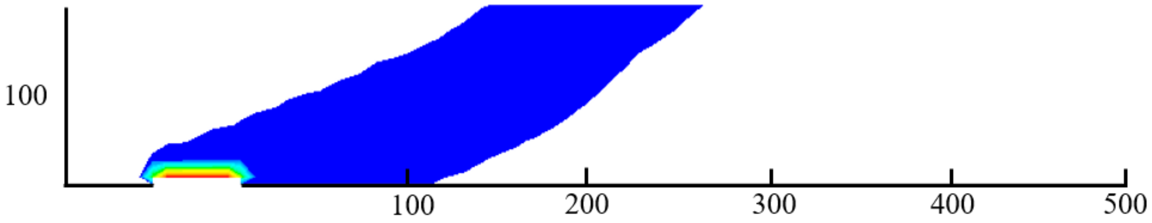

Figure 6.39: Plume shape for the plume temperature of 600 $°C$ at the smoke boundary

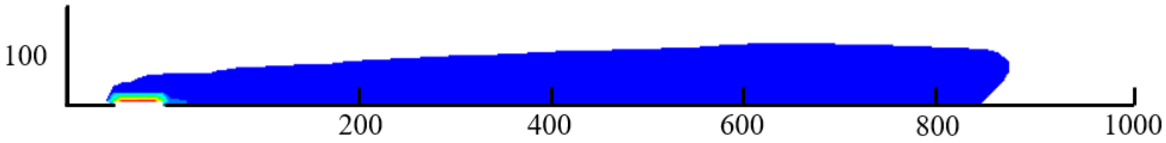

Figure 6.40: Plume shape for the plume temperature of 25 $°C$ at the smoke boundary

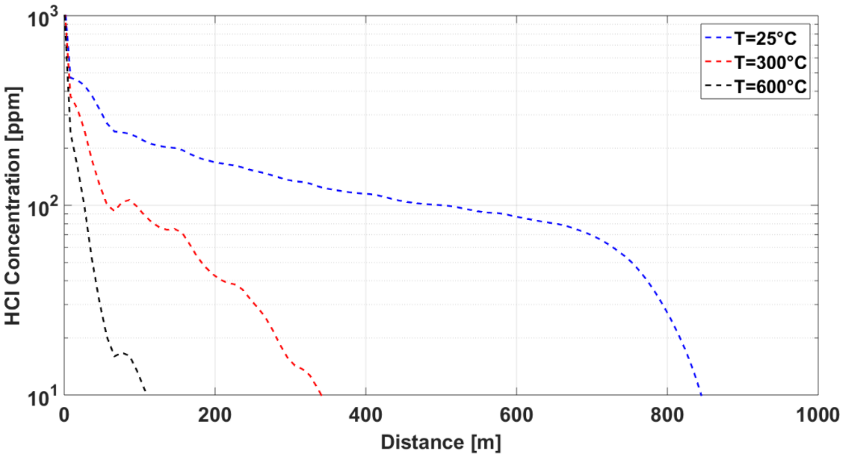

Figure 6.41: Concentration of HCl according to longitudinal distance from the fire

At the height of 1 m from the ground (moderately unstable)

Slightly Stable

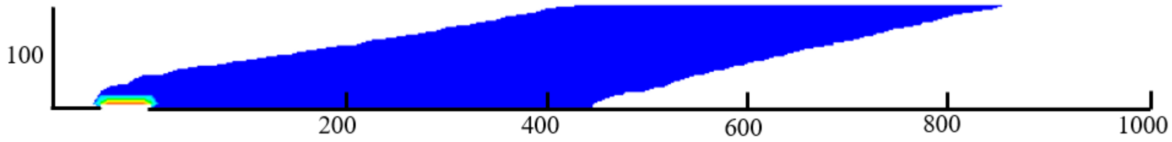

Figure 6.42: Plume shape for the plume temperature of 300 °C at the smoke boundary

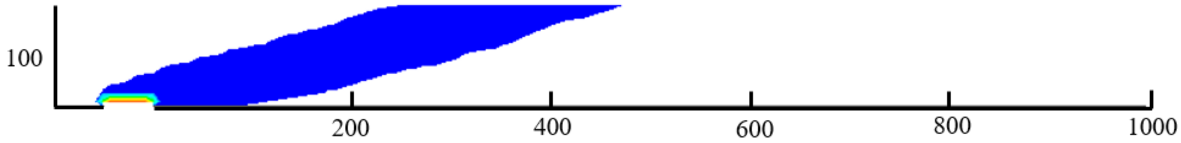

Figure 6.43: Plume shape for the plume temperature of 600 °C at the smoke boundary

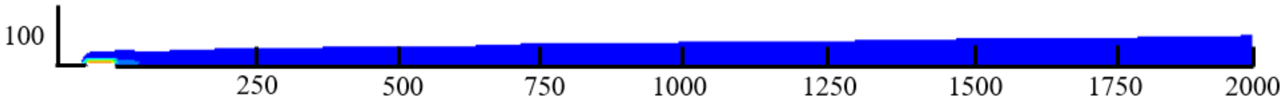

Figure 6.44: Plume shape for the plume temperature of 600 °C at the smoke boundary

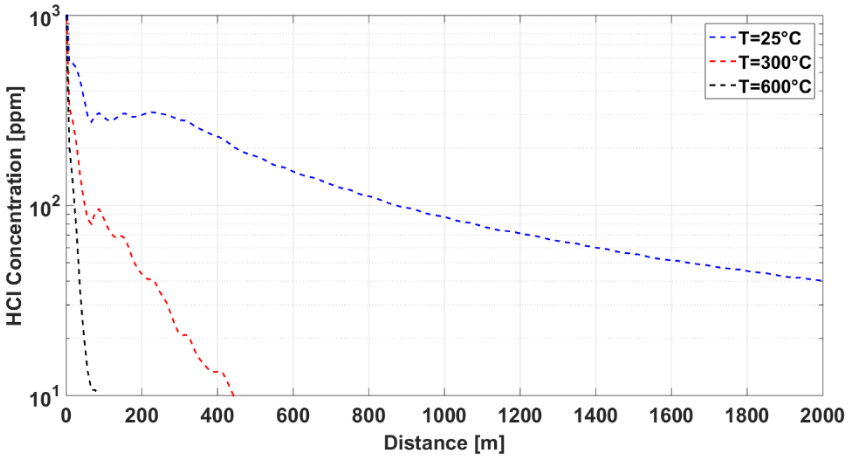

Figure 6.45: Concentration of HCl according to longitudinal distance from the fire at the height of 1 m from the ground (moderately unstable)

Neutral 5

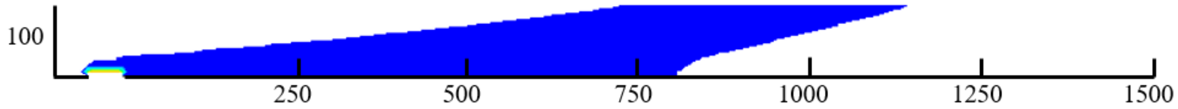

Figure 6.46: Plume shape for the plume temperature of 300 $°C$ at the smoke boundary

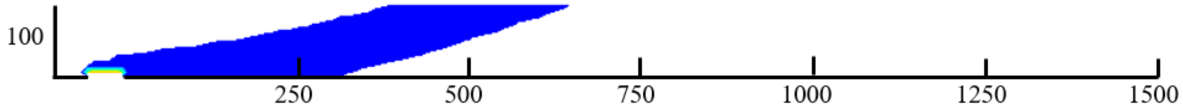

Figure 6.47: Plume shape for the plume temperature of 600 $°C$ at the smoke boundary

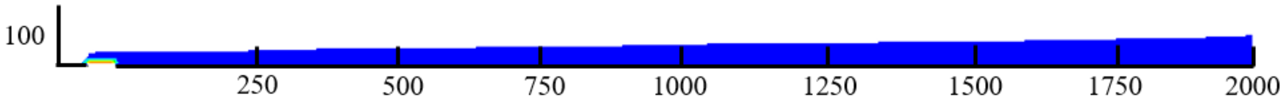

Figure 6.48: Plume shape for the plume temperature of 25 $°C$ at the smoke boundary

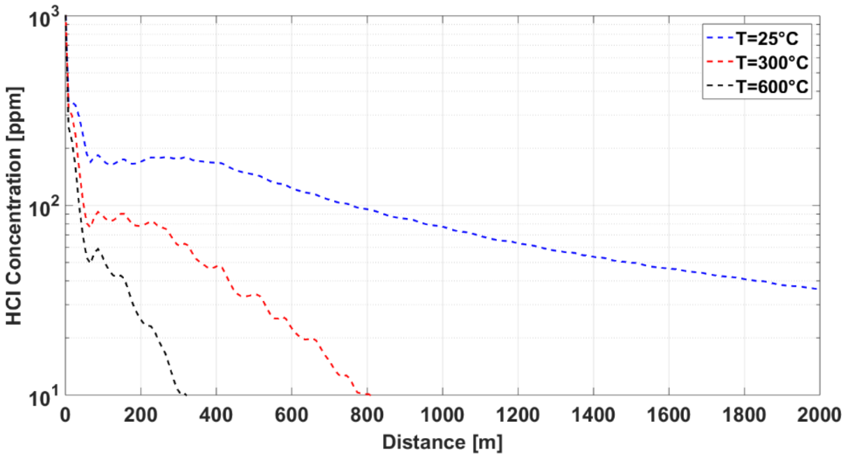

Figure 6.49: Concentration of HCl according to longitudinal distance from the fire at the height of 1 m from the ground (Neutral 5)

Neutral 8

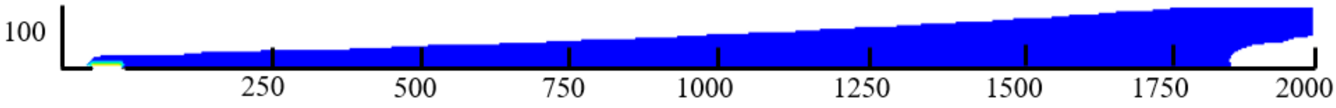

Figure 6.50: Plume shape for the plume temperature of 300 $°C$ at the smoke boundary

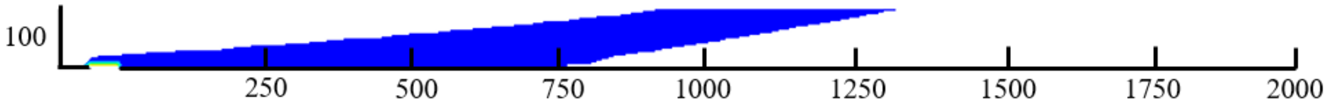

Figure 6.51: Plume shape for the plume temperature of 600 $°C$ at the smoke boundary

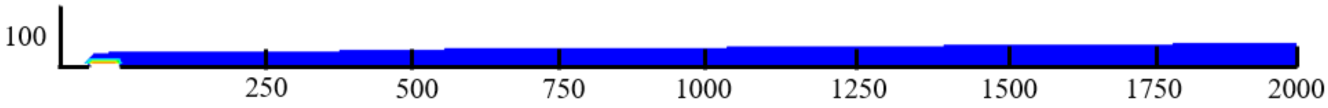

Figure 6.52: Plume shape for the plume temperature of 25 $°C$ at the smoke boundary

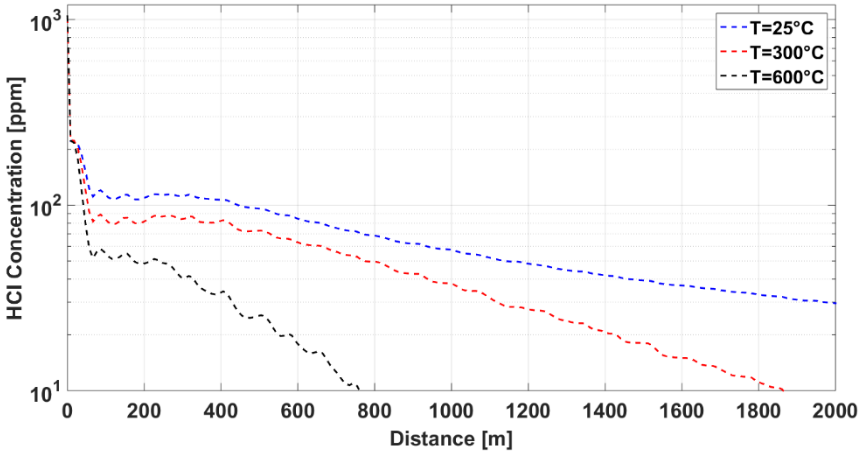

Figure 6.53: Concentration of HCl according to longitudinal distance from the fire at the height of 1 m from the ground (Neutral 8)

As shown by the above concentration contours, higher temperature for the smoke at the smoke inlet boundary results in the faster rising of the plume. The buoyant upward flux becomes stronger; consequently, the affected region by smoke near the ground (first 100 m) becomes smaller. This is true for all the atmospheric conditions. Even in neutral atmospheres with high wind velocity near the surface, the upward buoyant flux is not completely destroyed by the wind field on contrary to what happens for colder plumes (destruction of the upward buoyant flux by the wind field). This can be well-explained by figures 6.50 and 6.51 for the Neutral 8 atmosphere when wind speed at the height of 10 m from the surface is 8 m/s. When the smoke temperature at the boundary is 300 $°C$, the strong wind field disturbs the upward buoyant flux and keeps the pollutants near the surface. The plume affects till 2000 m far from the fire whereas this length decreases to about 750 m when the smoke temperature at the smoke inlet boundary is 600 $°C$. So, it is clear that decreasing the temperature of the pollution source leads to more unfavorable situations with respect to air quality.

The scope of this study was to provide a hazard analysis of smoke dispersion. Hazards analysis in safety engineering always deals with the prediction of the worst-case scenarios. So, smoke temperatures much larger than 300 $°C$ are more favorable compared to the lower temperatures. The concentration plots at the height of 1 m from the surface show that the longitudinal pollutant transport length for the smoke temperature of 600 $°C$ at the boundary is between 25 to 50 % of the transport length scale when the smoke temperature is 300 $°C$. In other words, the polluted region decreases between 50 to 75 % by increasing the smoke temperature from 300 to 600 $°C$.

The other temperature taken into account for the smoke boundary is the ambient temperature. As mentioned before, the smoke temperature can never be the ambient temperature but this low temperature is studied just to show the case dependency of the air pollution analysis and also the significance of the buoyancy in the ascendant of hot plumes. All the concentration contours show the accumulation of the pollutants near the ground when the smoke inlet temperature is ambient temperature. At the ambient temperature, there is no substantial buoyancy force. The comparison of the plume concentration contours reveals the fact that the main driving force for the upward movement of the plume is the buoyancy due to the temperature difference between the hot plume and the ambient air. In the absence of this huge temperature difference, plume does not rise and is strongly suppressed by the wind at the surface. Even in the unstable atmosphere where there is a convective upward air flux in the atmosphere, the plume only rises about 60 m. Concentration polts at the height of 1 m from the surface indicate that in all the atmospheric conditions, the plume with ambient temperature stays near the ground. Therefore, buoyancy is the main reason for the plume rise in comparison with vertical plume speed and vertical transport due to turbulence in the wind flow.

However, the most remarkable outcome out of the simulation of the plume with ambient temperature is the change in the worst atmospheric condition which declares that the analysis of the worst atmospheric condition with respect to air pollution is a case dependent study and varies with the variation of the characteristics of the pollution source. According to section 6.4.1, the wind speed near the surface is the main factor determining the worst atmospheric condition when it comes to the dispersion of pollutants from a pollution source with a high temperature near the ground. The higher the wind speed near the ground is, the more unfavorable atmospheric situation happens. So, the neutral atmosphere is the worst condition. This is not true when the temperature of the pollution source is close to the ambient temperature. In the absence of buoyancy, the effect of the thermal stratification in the atmosphere becomes more substantial. As depicted by the concentration contours (6.36 and 6.44), the strongly stable and slightly stable atmospheres also lead to the pollution of a huge area near the ground by the plume. Furthermore, moving towards a stable atmosphere results in a more catastrophic scenario because of the lower wind velocities near the surface. The high wind velocity near the surface dilutes the pollutants and reduces the concentration of pollutants.

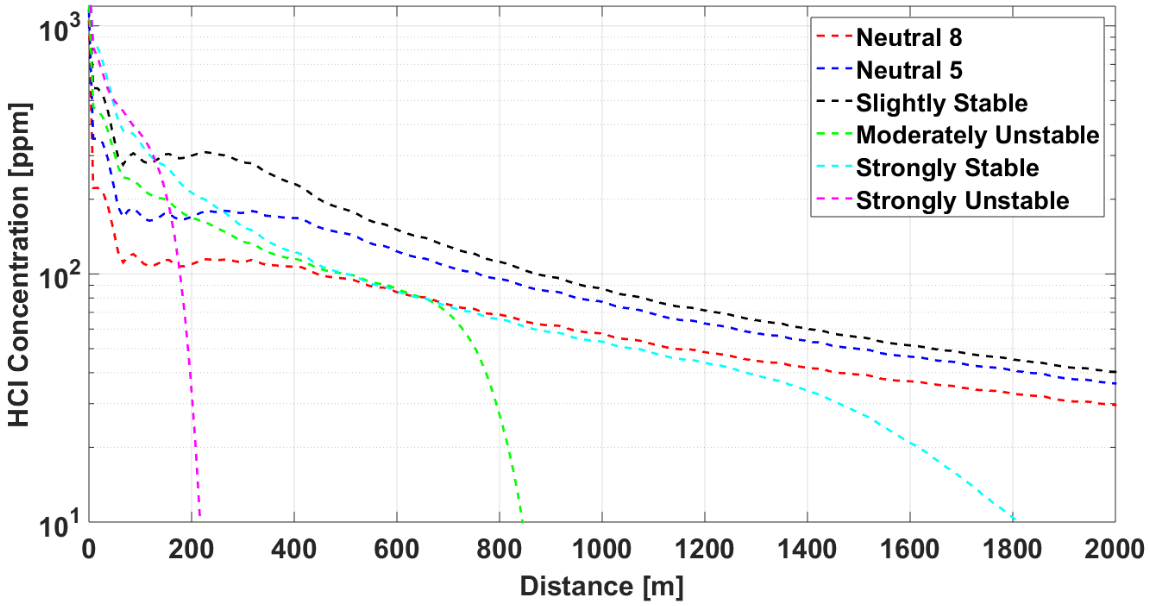

Figure 6.54: Concentration of HCl according to longitudinal distance from the fire at the height of 1 m from the ground ($T = 25\ °C$)

The strongly unstable atmosphere is still the most favorable atmosphere. On contrary to the simulation results obtained from plume with temperature of 300 °C at the smoke boundary, a strongly stable atmosphere results in worse condition compared to a moderately unstable atmosphere although wind speed near the ground in a strongly stable is less than a moderately unstable. This implies the fact that in the absence of strong upward buoyant flux, the temperature distribution in the atmosphere plays an important role in the plume dispersion. Then, the higher wind velocity near the surface does not necessarily lead into the worst condition. The most noticeable point of the cold plume simulation is the variation of the worst atmospheric conditions. For hot plume, the neutral 8 is the worst scenario because of the high wind speed near the surface. For cold plume, decreasing the wind speed up to a certain value (critical wind velocity) increases the concentration of the pollutants, meaning the air quality reduces.

As is clear from figure 6.54, reducing the wind speed near the ground from the Neutral 8 atmosphere ($u_{10} = 8$) to the slightly stable atmosphere ($u_{10} = 3$) increases the concentration of the accumulated pollutants near the ground substantially. The differences between the stability classes are more significant near the pollution source and going further from the source decreases the discrepancies. In the first 400 m from the fire, the HCl concentration at the height of 1 m from the surface is about three times larger in the slightly stable atmosphere compared to the Neutral 8 atmosphere. Furthur reduction in the magnitude of wind speed near the ground from the slightly stable atmosphere ($u_{10} = 3$) to strongly stable atmosphere ($u_{10} = 3$) again increases the air quality. This is mainly due to the fact that the low wind velocity does not suppress the pollutants near the surface. It is clear that both the concentration of the accumulated HCl near the surface (height of 1 m) and the longitudinal transport length scale in the flow direction are remarkably smaller in the strongly stable atmosphere compared to slightly stable. So, there is a critical wind velocity in the stable atmospheres which results in the worst air quality when the temperature of the pollution source is at ambient temperature.

Wind speeds less than this critical value do not suppress the plume strongly and wind speeds higher than this critical value dilute the concentration of the pollutants in the atmosphere. The concentration curves of HCl from the strongly stable and Neutral 8 atmospheres are relatively similar, although the wind speed in the Neutral 8 is much higher. This again shows the fact that when it comes to dispersion of the pollutants from a cold source near the ground, the wind speed magnitude near the surface is not the only important factor for the characterization of the worst atmosphere and the role of the thermal stratification of the atmosphere becomes considerable. The temperature distribution in the atmosphere (thermal stratification) determines the rate of variation of the wind speed with height. This is the mechanism through which the temperature distribution in the atmosphere and the wind field are coupled. It was explained at the beginning of this chapter that these two are not independent, although the characterization of the atmospheric condition in CFD simulation is mainly done by the specification of the wind velocity field.

6.1.7 Smoke components' mass fractions

The mass fraction of each component at the smoke boundary layer is dependent on the yield of that component. There are several different factors affecting the yield of a product during a fire, out of which the equivalence ratio (Φ) is the most important one. The amount of air influences the mass fraction of smoke components at the smoke boundary in two ways. On one hand, a higher amount of air results into more complete combustion and consequently lower yields for pollutants. On the other hand, a higher amount of air as the bulk spice in the smoke mixture dilutes the concentration of other components (pollutants).

The determination of the equivalence ratio for real open fires is impossible. Large fires are always incorporated with a lack of air because of the difficulty of penetration of air through the burning material. The simulations in this study were conducted for the equivalence ratio of 2 (worst case scenario); however, the effect of other values for the equivalence ratio is investigated in this section. Only the worst atmospheres (slightly stable, Neutral 5 and Neutral 8) are discussed in this section.

Table 6.3: Smoke component mass fractions at the smoke boundary for different equivalence ratios

Components	$\mathbf{\Phi = 2}$	$\mathbf{\Phi = 1.5}$	$\mathbf{\Phi = 1}$
x_{CO_2}	0.17	0.132	0.092
x_{CO}	0.037	0.029	0.020
x_{CH_4}	0.0315	0.024	0.0171
x_{HCl}	0.0084	0.0066	0.0046
x_{soot}	0.0125	0.0097	0.0068
$\dot{m}_{smoke}$	$113\,\frac{kg}{s}$	$144\,\frac{kg}{s}$	$207\,\frac{kg}{s}$

Slightly Stable:

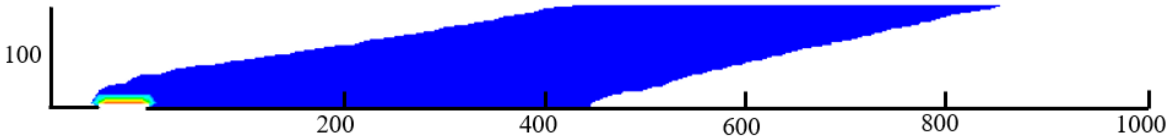

Figure 6.55: Plume shape for the equivalence ratio of 2

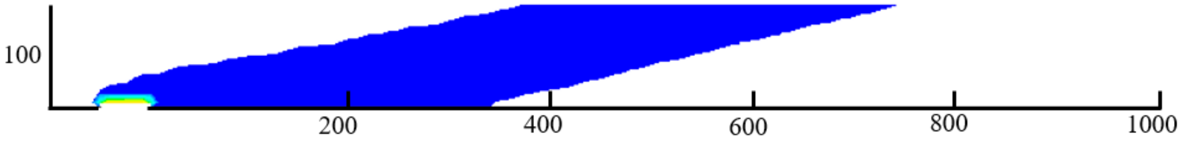

Figure 6.56: Plume shape for the equivalence ratio of 1.5

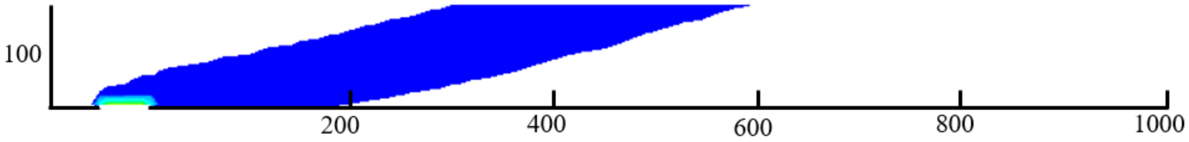

Figure 6.57: Plume shape for the equivalence ratio of 1

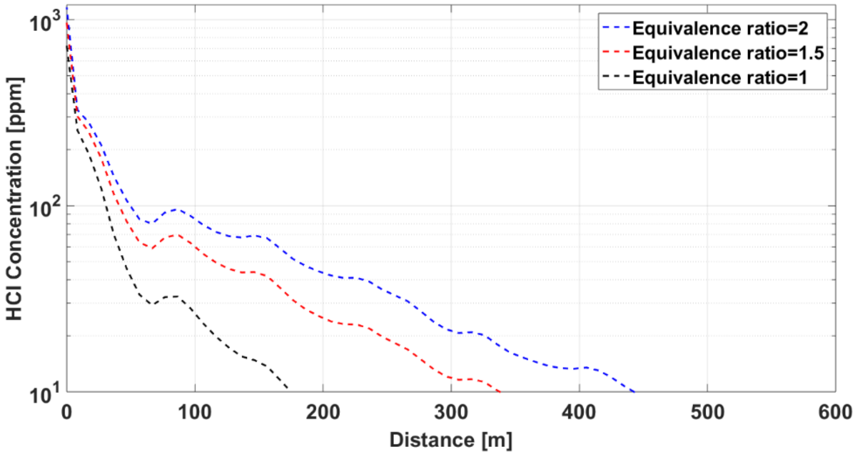

Figure 6.58: Concentration of HCl according to longitudinal distance from the fire at the height of 1 m from the ground (slightly stable)

Neutral 5:

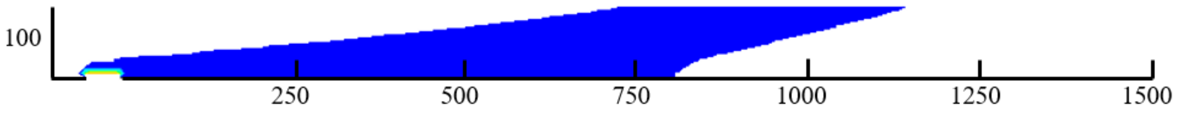

Figure 6.59: Plume shape for the equivalence ratio of 2

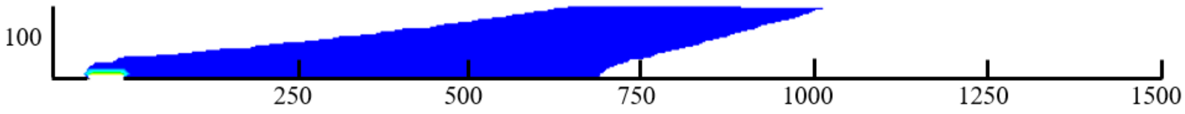

Figure 6.60: Plume shape for the equivalence ratio of 1.5

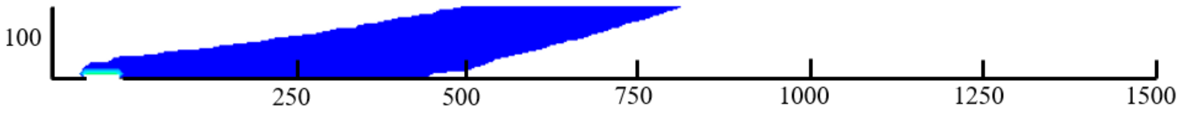

Figure 6.61: Plume shape for the equivalence ratio of 1

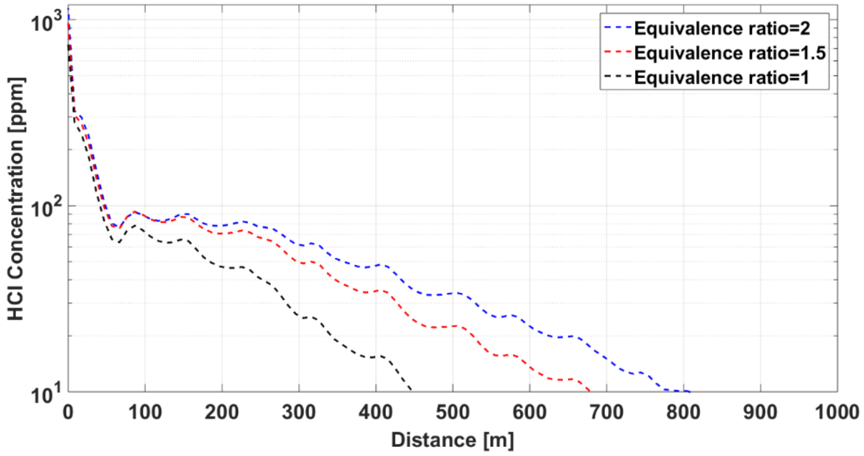

Figure 6.62: Concentration of HCl according to longitudinal distance from the fire at the height of 1 m from the ground (Neutral 5)

Neutral 8:

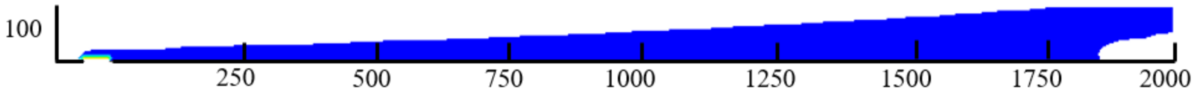

Figure 6.63: Plume shape for the equivalence ratio of 2

Figure 6.64: Plume shape for the equivalence ratio of 1.5

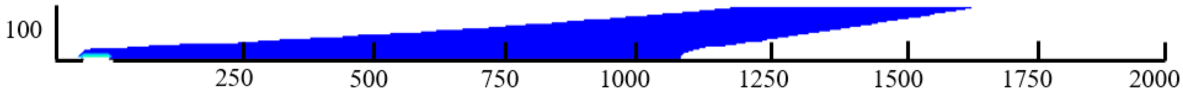

Figure 6.65: Plume shape for the equivalence ratio of 1

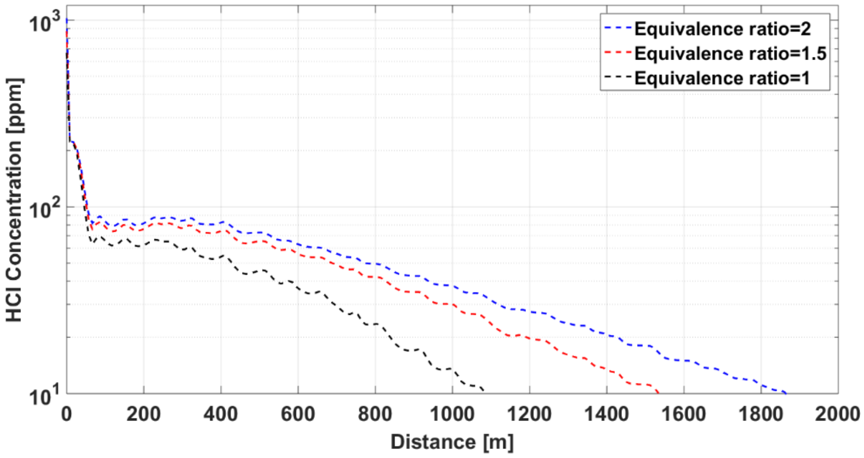

Figure 6.66: Concentration of HCl according to longitudinal distance from the fire at the height of 1 m from the ground (Neutral 8)

All the concentration contours show that decreasing the equivalence ratio (increasing the amount of air) results in the smaller volume polluted by the plume. The more the amount of air for the combustion is, the less the amount of toxic products is. Lack of air leads into incomplete combustion and the more the combustion incomplete is, the more toxicants are produced. The available air for burning is never the stoichiometric amount, which happens only for ideal burning, however, determination of the equivalence ratio for large open fires is not possible. There is no opportunity to measure the amount of entrained air during a large open fire. Due to the fact that the scope of this study was considering the worst scenario, the equivalence ratio of 2 was selected. An equivalence ratio of 2 means that the available air for the combustion of the fuels is 50 % of the air needed for complete combustion. Although this value of the equivalence ratio is a little pessimistic, it can be used as a conservative choice to cover the worst possibilities. Before closing the section, it would be worthy to mention that the equivalence ratio only affects the amount of smoke emission and its composition but does not change the analysis of the atmospheric condition. Independent of the value of the equivalence ratio, atmospheres with higher wind speed near the ground are the worst atmospheric conditions for the scenario in which the plume is released from a source with a much higher temperature than the ambient temperature near the ground.

Outcomes

The scope of this chapter was to draw a comparison between three different strategies facing an open fire with respect to air pollution. As described in chapter 1, the three strategies are letting the fire burn, extinguishment of fire with CAF and extinguishment of fire with water. In order to investigate the effect of fire on the air quality (non-thermal hazards), the fate of the smoke plume from the fire and also the smoke affected area should be predicted. In this regard, air dispersion modeling should be applied. In this contribution, the behavior of the smoke plume under different atmospheric conditions was investigated. The adopted stability classification was according to Pasquill-Gifford.

In the absence of temperature inversion in the atmosphere, wind speed magnitude near the surface is the key factor to suppress the pollutants near the ground in all atmospheric conditions. The higher the wind speed near the ground is, the lower the air quality at the surface is. Accordingly, the neutral condition is the worst atmospheric condition and slightly stable and moderately unstable atmospheres come after the neutral condition. The occurrence of inversion results in a more catastrophic situation (larger area affected by smoke near the ground), although wind velocity is very low. The occurrence of inversion is a more undesirable situation compared to the neutral condition. The most favorable atmospheric conditions regarding vertical transport of the pollutants are the strongly unstable and strongly stable atmospheres. In both of these conditions, the plume rises up without any disturbance from the wind.

Based on the simulation results in this chapter, all kinds of atmospheres lead to the pollution of a considerably huge region near the ground. The polluted region means the region, which is strongly irritant for human beings. The occurrence of inversion can create also an incapacitation zone near the ground. Although the strongly unstable and strongly stable atmospheres let the plume rise, it should be noted that there is no guarantee that pollutants do not come back again to the surface. The simulations in this study were based on the assumption of the steady wind field which does not happen in reality. The wind field is totally random and the atmospheric stability changes several times during a day. For example, the atmosphere does not constantly stay strongly unstable for several days. So, the pollutants are susceptible to deposit via precipitation or turbulence in the atmosphere. Based on the burning rate of the fuel measured during small-scale experiments and the amount of the burning material in the real assumed scenarios, both fires $50 \times 50\, m^2$ and $100 \times 100\, m^2$ continue to burn for about a week if they are not extinguished. Therefore, a huge area surrounding the fire cannot be allowed to be polluted for such a long time considering the fact that fire might also spread or cause different financial and human costs. All in all, it is clear that the strategy of 'let the fire burn' cannot be counted as a wise option and is out of the question; the fire should be extinguished.

When it comes to analysis with respect to air pollution, CAF and water differ from each other only in extinguishing time. Calculation of the extinguishing time for real fire scenarios is based on the extrapolation from the small-scale experiments. The extinguishing time for the fire $50 \times 50\, m^2$ and the fire $100 \times 100\, m^2$ is respectively 6.6 and 26.5 hours when water is applied as the fire-fighting agent. Based on the outcomes of the experiments, CAF has about 30 % higher fire-fighting efficiency than water. It implies that CAF is able to control the fire in 70 % of the time that water needs. So, the extinguishing time is reduced to 4.6 and 18.5 hours for the fire $50 \times 50\, m^2$ and the fire $100 \times 100\, m^2$ respectively. Reduction in the extinguishing time means a decrease in the production of smoke and toxicants. Table 6.5 shows the amount of reduction of each smoke component when water is substituted by CAF.

Table 6.4: Reduction in the produced amount of smoke and toxicants

Components	**Reduction in the produced amount (Fire 50×50)**	**Reduction in the produced amount (Fire 100×100)**
CO_2	137808 kg	2198304 kg
CO	30888 kg	494784 kg
CH_4	26352 kg	420480 kg
HCl	6768 kg	110304 kg
$soot$	10368 kg	166464 kg
$smoke$	813600 kg	13161600 kg

Although all the data shown in table 6.4 are approximations, the quantitative analysis shows the substantial advantage of CAF over water with respect to air pollution. The application of CAF decreases considerably the total amount of airborne pollutants that are produced by a fire.

7 Conclusions

In this study, the plume dispersion modeling was applied under various atmospheric conditions. The results show that a considerably massive volume near the ground can be affected by the smoke plume. The higher the wind speed near the surface is, the larger is the affected region by the smoke. Only very calm atmospheres such as strongly unstable and strongly stable do not accumulate the pollutants near the surface. Although the low wind speed in the calm atmospheric conditions let the plume rise without any disturbance, there is no guarantee that the pollutants do not come back to the land again. The pollutants might deposit via further precipitations (wet deposition) or wind turbulence (dry deposition). On the other hand, large fires can last for several days or even weeks if they are not extinguished and the atmospheric condition and wind velocity field do not stay constant for such a long time. Even if the atmosphere is strongly calm, it may change in some hours. All in all, the air dispersion modeling shows that the 'let the fire burn' is not really an option due to the fact that open fires affect the air quality of an enormous volume near the ground for a long time (until the fire finishes).

When it comes to the extinguishment of a fire, a controversial issue is to opt for the most efficient fire-fighting agent. In this regard, a set of small-scale experiments were conducted to quantify the fire suppression effectiveness of both CAF and water. Our experiments recorded up to 30 % higher fire-fighting efficiency of CAF over water. 30 % higher efficiency of CAF means a minimum reduction of 30 % in the water consumption during the extinguishment and 30 % lower extinguishment duration. The application of CAF instead of water decreases environmental damages with respect to soil and air pollution. Reduction of water usage decreases the amount of run-off; this is the main environmental advantage of CAF over water.

Less amount of run-off leads to a smaller covered area, therefore, less amount of soil should be treated. Remediation of the soil is an expensive process, reduction in the amount of polluted soil has a great financial benefit that can compensate for the costs of production of CAF. Less water consumption upon application of CAF becomes even more important when the soil at the location of the fire accident has a coarse texture and the water table is also shallow (close to the surface). The pollutant transport process through coarse-textured soils is very fast and consequently, the vulnerability of groundwater is high. The polluted soil should be treated urgently after the extinguishment process to protect groundwater from the contaminated infiltrating flux and a 30 % reduction in the amount of the polluted soil is a great beneficial point under this circumstance. The vulnerability of groundwater because of the run-off for different fire locations with different soils was investigated according to the critical traveling time that pollutants need to pass through the vadose zone and enter groundwater. This traveling time is mainly a function of the soil texture and depth of the water table. Traveling time can vary from several hours (when the soil has a coarse texture and the water table is shallow) to several weeks (occurrence of a deep water table beneath a fine-textured soil). However, the application of either water or CAF as the extinguishing agent does not change the traveling time for pollutants to groundwater.

Application of CAF also reduces the airborne pollutants via faster extinguishment process. CAF is able to reduce the extinguishment duration considerably meaning, the amount of the smoke released from the fire is reduced by several tons. All in all, class A foam is a more environmentally friendly agent compared to water in terms of air, soil, and groundwater pollution. However, the comparison between CAF and water was performed only with respect to environmental impacts. Other factors such as financial expenses and difficulties incorporated with the application of the CAF system were not taken into account in this investigation.

References

1. Clark, W.E., *Firefighting principles and practices*. 1991: PennWell Books.
2. Bureau, M.F., *COMPRESSED AIR FOAM SYSTEMS IN LIMITED STAFFING CONDITIONS.* 1997.
3. Darley, P.C., *The use of class" A" foam and compressed air foam systems (CAFS) in firefighting*. 1995.
4. Routley, J., *Compressed air foam for structural fire fighting: A field test.* TR074, Boston Fire Department, 1993.
5. Kim, A.K. and G.P. Crampton. *Application of a Newly-developed compressed-air-foam fire suppression system*. in *Proceedings of INTERFLAM*. 2001.
6. Van Genuchten, M.T., *A closed-form equation for predicting the hydraulic conductivity of unsaturated soils 1.* Soil science society of America journal, 1980. **44**(5): p. 892-898.
7. Brooks, R. and T. Corey, *HYDRAU uc properties of porous media.* Hydrology Papers, Colorado State University, 1964. **24**: p. 37.
8. Nandagiri, L. and R. Prasad, *Field evaluation of unsaturated hydraulic conductivity models and parameter estimation from retention data.* Journal of hydrology, 1996. **179**(1-4): p. 197-205.
9. Gifford Jr, F.A., *Use of routine meteorological observations for estimating atmospheric dispersion.* Nuclear Safety, 1961. **2**: p. 47-51.
10. Pasquill, F., *The estimation of the dispersion of windborne material.* Met. Mag., 1961. **90**: p. 33.
11. Haverkamp, R., et al., *Soil properties and moisture movement in the unsaturated zone*, in *The Handbook of Groundwater Engineering, Third Edition*. 2016, CRC Press. p. 167-208.
12. Nash, J., *Water as a Resource Chapter 10. The Global Water Budget Consider water as a resource because it is important for domestic use, agriculture, and industry.* 2016, https://slideplayer.com/slide/8493858/.
13. Fitts, C.R., *Groundwater science*. 2002: Elsevier.
14. Dippenaar, M.A., *Assessment of vadose zone hydrology: concepts, methods, applications and guidelines*. 2014, University of Pretoria.

15. Hillel, D., *Environmental soil physics: Fundamentals, applications, and environmental considerations*. 1998: Elsevier.
16. Whitlow, R., *Basic soil mechanics*. 1990.
17. Angulo-Jaramillo, R., et al., *An Introduction to Soil and Water Infiltration*, in *Infiltration Measurements for Soil Hydraulic Characterization*. 2016, Springer. p. 1-42.
18. Landon, J.R., *Booker tropical soil manual: a handbook for soil survey and agricultural land evaluation in the tropics and subtropics*. 2014: Routledge.
19. Helmig, R., *Multiphase flow and transport processes in the subsurface: a contribution to the modeling of hydrosystems*. 1997: Springer-Verlag.
20. Civan, F., *Porous media transport phenomena*. 2011: John Wiley & Sons.
21. Gray, W.G., *Macroscale equilibrium conditions for two-phase flow in porous media.* International Journal of Multiphase Flow, 2000. **26**(3): p. 467-501.
22. Nield, D.A. and A. Bejan, *Convection in porous media*. Vol. 3. 2006: Springer.
23. Brown, G., H. Hsieh, and D.A. Lucero, *Evaluation of laboratory dolomite core sample size using representative elementary volume concepts.* Water Resources Research, 2000. **36**(5): p. 1199-1207.
24. FrackOptima, *Fluid flow in porous media and Carter's equation*. 2014, http://www.frackoptima.com/userguide/theory/fluidflow-porousmedium-carter.html#f2
25. Davis, S.N., *Porosity and permeability of natural materials.* Flow through porous media, 1969: p. 54-89.
26. Ghanbarian, B., et al., *Tortuosity in porous media: a critical review.* Soil science society of America journal, 2013. **77**(5): p. 1461-1477.
27. Huinink, H., *Fluids in Porous Media*. 2016: Morgan & Claypool Publishers.
28. Matyka, M., A. Khalili, and Z. Koza, *Tortuosity-porosity relation in porous media flow.* Physical Review E, 2008. **78**(2): p. 026306.
29. Sahimi, M., *Flow phenomena in rocks: from continuum models to fractals, percolation, cellular automata, and simulated annealing.* Reviews of modern physics, 1993. **65**(4): p. 1393.
30. Scheidegger, A.E., *The physics of flow through porous media.* Soil Science, 1958. **86**(6): p. 355.

31. Nelson, P.H. *Evolution of permeability-porosity trends in sandstones*. in *SPWLA 41st Annual Logging Symposium*. 2000. Society of Petrophysicists and Well-Log Analysts.
32. Bear, J. and Y. Bachmat, *Introduction to modeling of transport phenomena in porous media*. Vol. 4. 2012: Springer Science & Business Media.
33. Ingham, D.B. and I. Pop, *Transport phenomena in porous media*. 1998: Elsevier.
34. Li, Y. and C.-W. Park, *Permeability of packed beds filled with polydisperse spherical particles.* Industrial & engineering chemistry research, 1998. **37**(5): p. 2005-2011.
35. Liu, S., A. Afacan, and J. Masliyah, *Steady incompressible laminar flow in porous media.* Chemical engineering science, 1994. **49**(21): p. 3565-3586.
36. Mauran, S., L. Rigaud, and O. Coudevylle, *Application of the carman–kozeny correlation to a high-porosity and anisotropic consolidated medium: The compressed expanded natural graphite.* Transport in Porous Media, 2001. **43**(2): p. 355-376.
37. Rahli, O., et al., *Fluid flow through randomly packed monodisperse fibers: The Kozeny-Carman parameter analysis.* Journal of fluids engineering, 1997. **119**(1): p. 188-192.
38. Rogowski, A., *Watershed physics: Model of the soil moisture characteristic.* Water Resources Research, 1971. **7**(6): p. 1575-1582.
39. Luckner, L., M.T. Van Genuchten, and D. Nielsen, *A consistent set of parametric models for the two-phase flow of immiscible fluids in the subsurface.* Water Resources Research, 1989. **25**(10): p. 2187-2193.
40. Miyazaki, T., et al., *Water flow in soils.* Soil Science, 1994. **157**(4): p. 264.
41. Schneider, M., *Wettability patterning in microfluidic systems and applications in the petroleum industry*. 2011, Université Pierre et Marie Curie-Paris VI.
42. Bonn, D., et al., *Wetting and spreading.* Reviews of modern physics, 2009. **81**(2): p. 739.
43. De Gennes, P.-G., *Wetting: statics and dynamics.* Reviews of modern physics, 1985. **57**(3): p. 827.
44. Young, T., *III. An essay on the cohesion of fluids.* Philosophical transactions of the royal society of London, 1805(95): p. 65-87.
45. Lunati, I., *Young's law and the effects of interfacial energy on the pressure at the solid-fluid interface.* Physics of Fluids, 2007. **19**(11): p. 118105.
46. Lagree, B., *Modelling of two-phase flow in porous media with volume-of-fluid method*. 2014, Paris 6.

47. Craig, F.F., *The reservoir engineering aspects of waterflooding, Vol. 3.* HL Doherty Memorial Fund of AIME New York, 1971.
48. Suh, H.S., et al., *Capillary pressure at irregularly shaped pore throats: Implications for water retention characteristics.* Advances in water resources, 2017. **110**: p. 51-58.
49. Szymkiewicz, A., *Modelling water flow in unsaturated porous media: Accounting for nonlinear permeability and material heterogeneity*. 2012: Springer Science & Business Media.
50. Tarboton, D.G., *Rainfall-runoff processes.* Utah State University, 2003. **1**(2).
51. Uliana, M.M., *Storage Coefficient.* Water Encyclopedia, 2005. **5**: p. 480-483.
52. Tanaka, H. and Q. Huimin, *Numerical simulation of sand terrace formation in front of a river mouth.* WIT Transactions on Modelling and Simulation, 1970. **6**.
53. Learner, A., *Confined and unconfined aquifer*. 2017, https://www.learner.org/courses/envsci/unit/text.php?unit=8&secNum=3#confined_unconfined_aquifer.
54. Rumynin, V.G., *Water movement and solute transport in unsaturated porous media,* in *Subsurface Solute Transport Models and Case Histories*. 2011, Springer. p. 77-119.
55. Nasta, P., J.A. Vrugt, and N. Romano, *Prediction of the saturated hydraulic conductivity from Brooks and Corey's water retention parameters.* Water Resources Research, 2013. **49**(5): p. 2918-2925.
56. Van Genuchten, M.v., F. Leij, and S. Yates, *The RETC code for quantifying the hydraulic functions of unsaturated soils.* 1991.
57. Visser, W., *An empirical expression for the desorption curve*. 1969, [sn].
58. Clapp, R.B. and G.M. Hornberger, *Empirical equations for some soil hydraulic properties.* Water resources research, 1978. **14**(4): p. 601-604.
59. King, L., *Description of Soil Characteristics for Partially Saturated Flow 1.* Soil Science Society of America Journal, 1965. **29**(4): p. 359-362.
60. Laliberte, G., *A mathematical function for describing capillary pressure-desaturation data.* Hydrological Sciences Journal, 1969. **14**(2): p. 131-149.
61. Su, C. and R.H. Brooks. *Soil hydraulic properties from infiltration tests*. in *Watershed Management; Proceedings of a Symposium*. 1975.
62. Van Genuchten, M.T. and D. Nielsen. *On describing and predicting the hydraulic properties*. in *Annales Geophysicae*. 1985.
63. Brutsaert, W., *Probability laws for pore-size distributions.* Soil Science, 1966. **101**(2): p. 85-92.

64. Vauclin, M., D. Khanji, and G. Vachaud, *Experimental and numerical study of a transient, two-dimensional unsaturated-saturated water table recharge problem.* Water Resources Research, 1979. **15**(5): p. 1089-1101.

65. Bumb, A.C., C.L. Murphy, and L.G. Everett, *A comparison of three functional forms for representing soil moisture characteristics.* Groundwater, 1992. **30**(2): p. 177-185.

66. Oosterbaan, R. and H. Nijland, *12 Determining the Saturated Hydraulic Conductivity.* 1994.

67. Guarracino, L., *Estimation of saturated hydraulic conductivity Ks from the van Genuchten shape parameter α.* Water resources research, 2007. **43**(11).

68. Patil, N.G. and S.K. Singh, *Pedotransfer functions for estimating soil hydraulic properties: A review.* Pedosphere, 2016. **26**(4): p. 417-430.

69. Freeze, R. and J. Cherry, *1979, Groundwater, Prentice-Hall, Englewood Cliffs, N. J.*

70. Mualem, Y., *A new model for predicting the hydraulic conductivity of unsaturated porous media.* Water resources research, 1976. **12**(3): p. 513-522.

71. Oh, S., Y. Kim, and J.-W. Kim, *A modified van Genuchten-Mualem Model of hydraulic conductivity in Korean Residual Soils.* Water, 2015. **7**(10): p. 5487-5502.

72. Bear, J., *Dynamics of fluids in porous media*. 2013: Courier Corporation.

73. Vafai, K., *Handbook of porous media*. 2015: Crc Press.

74. Šimůnek, J., M.T. van Genuchten, and M. Šejna, *Development and applications of the HYDRUS and STANMOD software packages and related codes.* Vadose Zone Journal, 2008. **7**(2): p. 587-600.

75. Gardner, W., *Some steady-state solutions of the unsaturated moisture flow equation with application to evaporation from a water table.* Soil science, 1958. **85**(4): p. 228-232.

76. Vanderborght, J., et al., *A set of analytical benchmarks to test numerical models of flow and transport in soils.* Vadose Zone Journal, 2005. **4**(1): p. 206-221.

77. Corey, A.T., *Mechanics of immiscible fluids in porous media*. 1994: Water Resources Publication.

78. Gerke, H.H., *Preferential flow descriptions for structured soils.* Journal of Plant Nutrition and Soil Science, 2006. **169**(3): p. 382-400.

79. Ranatunga, K., E.R. Nation, and D.G. Barratt, *Review of soil water models and their applications in Australia.* Environmental Modelling & Software, 2008. **23**(9): p. 1182-1206.

80. Bear, J., *Hydraulics of groundwater*. 2012: Courier Corporation.

81. Van Dam, J., et al., *Concepts and dimensionality in modeling unsaturated water flow and solute transport.* Frontis, 2005: p. 1-36.

82. Spitz, K. and J. Moreno, *A practical guide to groundwater and solute transport modeling*. 1996: John Wiley and sons.

83. Patil, S. and H. Chore, *Contaminant transport through porous media: An overview of experimental and numerical studies.* Advances in environmental research, 2014. **3**(1): p. 45-69.

84. Goode, D.J. and L.F. Konikow, *Apparent dispersion in transient groundwater flow.* Water Resources Research, 1990. **26**(10): p. 2339-2351.

85. Gelhar, L.W., C. Welty, and K.R. Rehfeldt, *A critical review of data on field-scale dispersion in aquifers.* Water resources research, 1992. **28**(7): p. 1955-1974.

86. Neuman, S.P., *Universal scaling of hydraulic conductivities and dispersivities in geologic media.* Water resources research, 1990. **26**(8): p. 1749-1758.

87. Radcliffe, D.E. and J. Simunek, *Soil physics with HYDRUS: Modeling and applications*. 2010: CRC press.

88. Colls, J., *Air pollution.* 2002.

89. De Visscher, A., *Air dispersion modeling*. 2014: Wiley Online Library.

90. DARRAN SIMON, M.P.A.R.R., CNN *A huge fire at a Texas chemical plant is out, 4 days after it started*. 2019, https://www.kyma.com/news/national-world/fire-at-texas-petrochemical-facility-still-burning-4-days-later/1060926536.

91. Leelőssy, Á., et al., *Dispersion modeling of air pollutants in the atmosphere: a review.* Open Geosciences, 2014. **6**(3): p. 257-278.

92. Vesilind, P.A., S.M. Morgan, and L.G. Heine, *Introduction to environmental engineering-SI version*. 2010: Cengage Learning.

93. Antonacci, G., *Air pollution modelling over complex topography*. 2004, University of Trento.

94. Driedonks, A. and H. Tennekes, *Entrainment effects in the well-mixed atmospheric boundary layer.* Boundary-Layer Meteorology, 1984. **30**(1-4): p. 75-105.

95. Stull, R.B., *An introduction to.* Boundary Layer Meteorology, 1988: p. 224-287.

96. Weiner, R., R. Matthews, and P.A. Vesilind, *Environmental engineering*. 2003: Butterworth-Heinemann.

97. Patil, R., *A Brief Look at the Causes and Effects of Temperature Inversion*. 2018 https://sciencestruck.com/causes-effects-of-temperature-inversion.

98. Kushkin, A.V., *Understanding the impact of vegetation on surface roughness length for enhancing wind resource characterization in Iowa.* 2014.

99. Gualtieri, G. and S. Secci, *Wind shear coefficients, roughness length and energy yield over coastal locations in Southern Italy.* Renewable Energy, 2011. **36**(3): p. 1081-1094.

100. Thom, A.S., *Momentum, mass, and heat exchange of plant communities.* Vegetation and the Atmosphere, 1975. **1**: p. 57-109.

101. Gupta, A.K. and P.J. Moss, *Guidelines for design of low-rise buildings subjected to lateral forces*. 1993: CRC Press.

102. Newman, J. and P. Klein, *The impacts of atmospheric stability on the accuracy of wind speed extrapolation methods.* Resources, 2014. **3**(1): p. 81-105.

103. Atkinson, D.G., et al., *Improvements to the EPA industrial source complex dispersion model.* Journal of Applied Meteorology, 1997. **36**(8): p. 1088-1095.

104. Nicholas, F.W. and J.E. Lewis, *Relationships between aerodynamic roughness and land use and land cover in Baltimore, Maryland*. 1980: USGPO.

105. Wieringa, J. *New revision of Davenport roughness classification*. in *Proceedings of the 3rd European & African Conference on Wind Engineering, Eindoven, Netherlands*. 2001.

106. Speziale, C.G., *Analytical methods for the development of Reynolds-stress closures in turbulence.* Annual review of fluid mechanics, 1991. **23**(1): p. 107-157.

107. Centre, S.R.L., *Laminar vs Turbulent Flow with Reynolds Number*. 2019, http://learn.sigmarockets.com/lessons/understanding-aerodynamics-with-the-educator-rocket/.

108. Versteeg, H.K. and W. Malalasekera, *An introduction to computational fluid dynamics: the finite volume method*. 2007: Pearson education.

109. Make, M., *Predicting Scale Effects on Floating Offshore Wind Turbines: A Numerical Analysis of Modeland Full-scale Wind Turbines using a RANS CFD Solver*. 2014, Master thesis, Technical University Delft.

110. Guide, A.F.U., *Release 14.0, ANSYS.* Inc., USA, November, 2011.

111. Launder, B.E. and D.B. Spalding, *The numerical computation of turbulent flows*, in *Numerical prediction of flow, heat transfer, turbulence and combustion*. 1983, Elsevier. p. 96-116.

112. Fluent, A., *Ansys fluent theory guide.* ANSYS Inc., USA, 2011. **15317**: p. 724-746.

113. Melcher, T., et al., *Experimental investigations on the repeatability of real scale fire tests.* Fire Safety Journal, 2016. **82**: p. 101-114.

114. German Institute for Standardization, DIN EN 3-7 Tragbare Feuerlöoscher - Teil 7: Eigenschaften, Löoschleistung, Anforderungen und Prüfungen, Beuth Verlag, 2004.

115. Holemann, H., *Environmental problems caused by fires and fire-fighting agents.* Fire Safety Science, 1994. **4**: p. 61-77.

116. Sharma, P., et al., *Fate and transport of fire-born particles in porous media.* Technologies, 2016. **4**(1): p. 2.

117. Palmer, R. and M. Lewis, *Assessment of groundwater vulnerability in England and Wales.* Geological Society, London, Special Publications, 1998. **130**(1): p. 191-198.

118. Albinet, M. and J. Margat, *Groundwater pollution vulnerability mapping.* Bulletin du Bureau de Recherches Géologiques et Minières Bull BRGM 2nd Series, 1970. **3**(4): p. 13-22.

119. Olmer, M. and B. Rezac, *Methodical principles of maps for protection of groundwater in Bohemia and Moravia scale 1/200.000.* Mem. IAH, 1974. **10**(1): p. 105-107.

120. Bachmat, Y. and M. Collin. *Mapping to assess groundwater vulnerability to pollution*. in *Vulnerability of soil and groundwater to pollutants, Proceedings and Information*. 1987.

121. Sotornikova, R. and J. Vrba, *Some remarks on the concept of vulnerability maps.* Atti Int, 1987.

122. Squillace, P.J., et al., *Preliminary assessment of the occurrence and possible sources of MTBE in groundwater in the United States, 1993− 1994.* Environmental Science & Technology, 1996. **30**(5): p. 1721-1730.

123. Carsel, R.F. and R.S. Parrish, *Developing joint probability distributions of soil water retention characteristics.* Water resources research, 1988. **24**(5): p. 755-769.

124. Delleur, J.W., *The handbook of groundwater engineering*. 2010: CRC press.

125. Schroeder, P.R., et al., *The hydrologic evaluation of landfill performance (HELP) model: engineering documentation for version 3.* 1994.

126. Lenhard, R., J. Parker, and S. Mishra, *On the correspondence between Brooks-Corey and van Genuchten models.* Journal of Irrigation and Drainage Engineering, 1989. **115**(4): p. 744-751.

127. Blau, P.J., *Microindentation Techniques in Materials Science and Engineering: A Symposium Sponsored by ASTM Committee E-4 on Metallography and by the*

International Metallographic Society, Philadelphia, PA, 15-18 July 1984. 1986: Astm International.

128. Bartzis, J.G., *Thematic area 5: Best practice advice for environmental flows.* The QNET-CFD Network Newsletter, 2004. **2**: p. 34-39.
129. Cowan, I.R., I.P. Castro, and A.G. Robins, *Numerical considerations for simulations of flow and dispersion around buildings.* Journal of Wind Engineering and Industrial Aerodynamics, 1997. **67**: p. 535-545.
130. Scaperdas, A., *Best practice advice for civil construction and HVAC.* The QNET-CFD Network Newletter, 2004.
131. Frank, J., et al., *Best practice guideline for the CFD simulation of flows in the urban environment. COST action 732.* Quality Assurance and Improvement of Meteorological Models. University of Hamburg, Meteorological Institute, Center of Marine and Atmospheric Sciences, 2007.
132. Hargreaves, D. and N.G. Wright, *On the use of the k–ε model in commercial CFD software to model the neutral atmospheric boundary layer.* Journal of Wind Engineering and Industrial Aerodynamics, 2007. **95**(5): p. 355-369.
133. Richards, P. and R. Hoxey, *Appropriate boundary conditions for computational wind engineering models using the k-ϵ turbulence model.* Journal of wind engineering and industrial aerodynamics, 1993. **46**: p. 145-153.
134. Krause, U., M. Schmidt, and F. Ferrero, *Investigation of the development of conflagration of solid material via analysis of coupled heat, mass and momentum transport.* Chemical Engineering & Technology: Industrial Chemistry-Plant Equipment-Process Engineering-Biotechnology, 2009. **32**(2): p. 292-305.
135. Hurley, M.J., et al., *SFPE handbook of fire protection engineering*. 2015: Springer.
136. Emslie, J., *Ground-based inversion frequencies determined from surface climatological data.* Boundary-Layer Meteorology, 1979. **16**(4): p. 409-419.
137. Morgan, T. and R.D. Bornstein, *Inversion Climatology at San José California.* Monthly Weather Review, 1977. **105**(5): p. 653-656.
138. Myrick, R., et al., *Seasonal mixing heights and inversions at Edmonton, Alberta.* Atmospheric Environment, 1994. **28**(4): p. 723-729.
139. Hartzell, G., D. Priest, and W. Switzer, *Modeling of toxicological effects of fire gases: II. Mathematical modeling of intoxication of rats by carbon monoxide and hydrogen cyanide.* Journal of fire sciences, 1985. **3**(2): p. 115-128.

140. de Santana, S.C., et al., *Modeling and simulation of breakthrough curves during purification of two chitosanases from Metarhizium anisopliae using ion-exchange with expanded bed adsorption chromatography*. Korean Journal of Chemical Engineering, 2014. **31**(4): p. 684-691.

141. Löhnert, A., *Modellierung von Brandszenarien mit CFD unter Berücksichtigung des Einflusses der Brandrauchzusammensetzung auf die Toxizität und Sichtweiten. 2015.*

142. Schubert-Polzin S., Krause U., *AERIUS Alternatives Löschmittel Druckluftschaum- komplexe Großschadenslagen vermeiden, Part: Ermittlung der Löschwirkung und der Umweltbilanz anhand von Brandversuchen, Final report to project part, Project registration number 13N13630, Otto-von-Guericke-Universität Magdeburg.*

143. Ahlers, L.; *Störungen des Ökosystems „Boden“ durch Feuerlöschschäume, Bachelorarbeit, Hochschule-Magdeburg Stendal, Fachbereich Wasserwirtschaft, 2018.*

Appendix A: Coefficient Form PDE in COMSOL

The coefficient form PDE was selected for expression of the both Richards and solute transport equations (figure A.1). The general view of the coefficient form PDE is shown in figure A.2. u is the dependent variable whereas the rest are the equation coefficients. The coefficients should be assigned in a proper way to obtain the required PDE. The coefficients can be either function or constant.

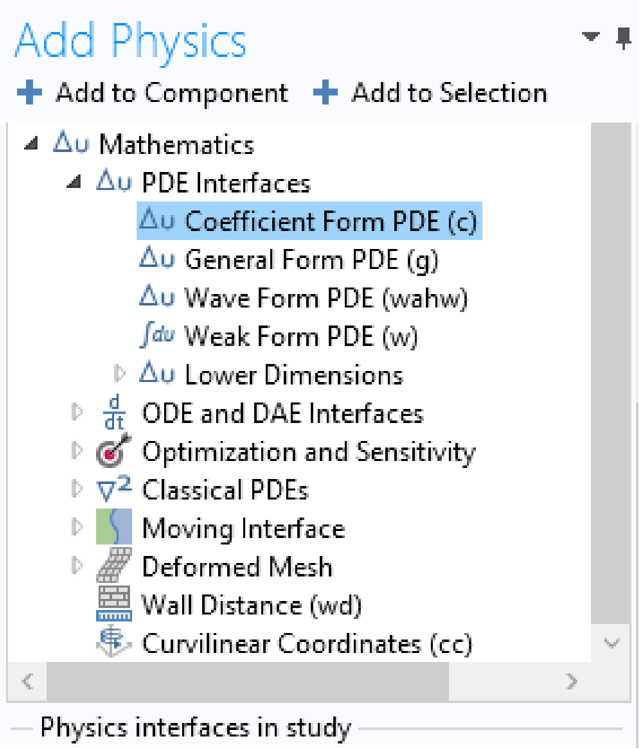

Figure A.1: Physics selection interface in COMSOL Multiphysics (screenshot from Comsol)

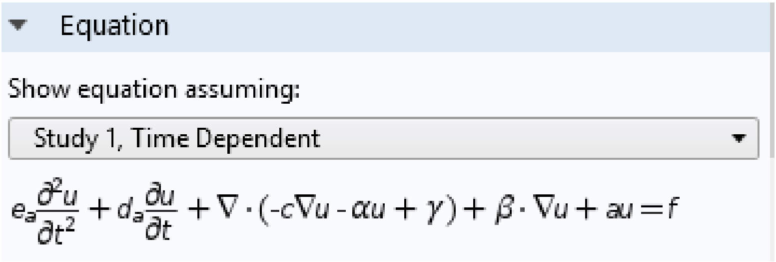

Show equation assuming:

Study 1, Time Dependent

$$e_a\frac{\partial^2 u}{\partial t^2} + d_a\frac{\partial u}{\partial t} + \nabla\cdot(-c\nabla u - \alpha u + \gamma) + \beta\cdot\nabla u + au = f$$

Figure A.2: General view of the coefficient form PDE (screenshot from Comsol)

Appendix B: Calculation of Mass Fractions at Smoke Inlet Boundary

The burning rate per unit area obtained from our experiments for mixed burning material is:

$$m_f'' = 0.008 \, \frac{kg}{m^2 . s} \tag{B.1}$$

Accordingly, the burning rate for a larger fire can be calculated by upscaling the small scale experiments:

$$Burning\ Area = 50 \times 50 = 2500 \, m^2 \tag{B.2}$$

$$\dot{m}_f = m_f'' \times Burning\ Area = 0.008 \times 2500 = 20 \, \frac{kg}{s} \tag{B.3}$$

So, the burning rate of the fuel is available. The smoke mass is the sum of the mass of burning fuel and entrained air:

$$\dot{m}_{smoke} = \dot{m}_f + \dot{m}_{air} \tag{B.4}$$

In order to obtain the mass flow rate of the air, the combustion reaction equation should be written. In this regard, the chemical formula of the burning material is needed, although it is not possible to represent the whole mixed burning material with one chemical formula. Krause et al. (2009) [134] offered the chemical formula of $C_{241}H_{228}O_{46}$ for the construction foam which was also used in this contribution. For the sake of simplification, the number of moles of each element was divided by 46 (molar amount of oxygen in one mole of fuel) and the final form of the chemical formula used for writing the chemical reaction was C_5H_5O. The molar mass of the fuel is nearly 80 $kg/kmol$. Using this chemical formula for the burning material is fairly accurate as of the first order of approximation.

The stoichiometric combustion reaction for the fuel is:

$$C_5H_5O + 5.5\,(O_2 + 3.76\,N_2) \rightarrow 5\,CO_2 + 2.5\,H_2O + 5.5\, \times 3.76\,N_2 \tag{B.5}$$

The molar burning rate of the fuel is 0.25 [$kmol/s$], so the combustion reaction is:

$$0.25\,C_5H_5O + 1.37\,(O_2 + 3.76\,N_2) \rightarrow 1.25\,CO_2 + 0.625\,H_2O + 5.17\,N_2 \tag{B.6}$$

According to the stoichiometric reaction:

$$\dot{m}_{O_2,required} = 1.37 \times 32 \approx 43\ \frac{kg}{s} \tag{B.7}$$

And:

$$\dot{m}_{N_2,required} = 5.17 \times 28 \approx 144\ \frac{kg}{s} \tag{B.8}$$

The total amount of stoichiometric air is sum of oxygen and nitrogen:

$$\dot{m}_{air,required} = \dot{m}_{O_2,required} + \dot{m}_{N_2,required} = 43 + 144 = 187\ \frac{kg}{s} \tag{B.9}$$

The above calculations are for a stoichiometric reaction. The stoichiometric reaction is needed for the calculation of the amount of air contributing to the combustion reaction for other equivalence ratios. In our case, the equivalence ratio of 2 is assumed.

The mass flow rate of the fuel is the same as the stoichiometric reaction which is based on our small scale experiments. The amount of air changes from its value for the stoichiometric reaction. For the equivalence ratio of 2, the entrained air is half of the stoichiometric value.

$$\dot{m}_f = 20\ \frac{kg}{s} \tag{B.10}$$

$$\dot{m}_{air} = \frac{\dot{m}_{air,stoi}}{2} = \frac{187}{2} = 93.5\ \frac{kg}{s} \tag{B.11}$$

And the total rate of production of smoke for an equivalence ratio of 2 is:

$$\dot{m}_{smoke} = \dot{m}_f + \dot{m}_{air} = 20 + 93.5 = \mathbf{113}\ \boldsymbol{\frac{kg}{s}} \tag{B.12}$$

For the smoke inlet boundary (mass flow inlet), the total mass flow rate of smoke and mass fractions of its components are required. Till now, the mass flow rate has been calculated and the next step is to obtain the components' mass fractions. The combustion products of incomplete combustion are totally different from the products of the stoichiometric combustion reaction. It was discussed earlier that carbon dioxide (CO_2), carbon monoxide (CO), hydrogen chloride (HCl), methane (CH_4), soot (C) and air are the main components of the smoke and air is the bulk specie of the mixture.

The mixed crib was the combination of wood, PE, PP, PU, and PVC. Each burning material leads to different yields for the smoke components. To calculate the yields from each burning material, the burning rate of each of them was needed. It was assumed that the contribution of each material in the burning process is directly proportional to its mass fraction in the mixed crib. So, the burning rate of each material equals the multiplication of the total mass flow rate of smoke by the mass fraction of that material in the crib.

$$\dot{m}_\alpha = \dot{m}_f \times x_\alpha \tag{B.13}$$

Where x_α is the mass fraction of the material α in the fuel and $\dot{m}_f = 20$.

Table B.1: Contribution of each material in the burning process

Burning material	**Mass [kg]**	**Mass fraction**	**Burning rate ($\dot{m}_\alpha$) [kg/s]**
Wood	55	0.75	15
PE	3.2	0.056	1.13
PP	2.9	0.051	1.04
PU	4	0.068	1.37
PVC	4.5	0.071	1.42
	$\sum \approx 70$		

The next step is to calculate the yield and mass flow rate of each product from each material. The relationships for the calculation of yields of combustion products according to the equivalence ratio are provided in the fourth chapter of the third section in the Handbook of Fire Protection Engineering [135].

$\boldsymbol{CO_2}$:

Yields:

$$Y_{CO_2,wood} = 1.33\left[1 - \frac{1}{\exp{(\Phi/2.15)^{-1.2}}}\right] = 0.8831\ \frac{kg_{CO_2}}{kg_{wood}} \tag{B.14}$$

$$Y_{CO_2,PP} = 2.79\left[1 - \frac{1}{\exp{(\Phi/2.15)^{-1.2}}}\right] = 1.8526\ \frac{kg_{CO_2}}{kg_{PP}} \tag{B.15}$$

$$Y_{CO_2,PE} = 2.76\left[1 - \frac{1}{\exp{(\Phi/2.15)^{-1.2}}}\right] = 1.8327\ \frac{kg_{CO_2}}{kg_{PE}} \tag{B.16}$$

$$Y_{CO_2,PU} = 1.51\left[1 - \frac{1}{\exp{(\Phi/2.15)^{-1.2}}}\right] = 1.0026\ \frac{kg_{CO_2}}{kg_{PU}} \tag{B.17}$$

$$Y_{CO_2,PVC} = 0.46\left[1 - \frac{0.3}{\exp{(\Phi/0.53)^{-11}}}\right] = 0.3220\ \frac{kg_{CO_2}}{kg_{PVC}} \tag{B.18}$$

Mass flow rates:

$$\dot{m}_{CO_2,wood} = \dot{m}_{wood} \times Y_{CO_2,wood} = 15 \times 0.8831 = 13.247\ \frac{kg_{CO_2}}{s} \tag{B.19}$$

$$\dot{m}_{CO_2,PP} = \dot{m}_{PP} \times Y_{CO_2,PP} = 1.04 \times 1.8526 = 1.9267\ \frac{kg_{CO_2}}{s} \tag{B.20}$$

$$\dot{m}_{CO_2,PE} = \dot{m}_{PE} \times Y_{CO_2,PE} = 1.13 \times 1.8327 = 2.0709\ \frac{kg_{CO_2}}{s} \tag{B.21}$$

$$\dot{m}_{CO_2,PU} = \dot{m}_{PU} \times Y_{CO_2,PU} = 1.37 \times 1.0026 = 1.3736\ \frac{kg_{CO_2}}{s} \tag{B.22}$$

$$\dot{m}_{CO_2,PVC} = \dot{m}_{PVC} \times Y_{CO_2,PVC} = 1.42 \times 0.3220 = 0.4572\ \frac{kg_{CO_2}}{s} \tag{B.23}$$

The total production rate of carbon dioxide is:

$$\begin{gathered}\dot{m}_{CO_2} = \dot{m}_{CO_2,wood} + \dot{m}_{CO_2,PP} + \dot{m}_{CO_2,PE} + \dot{m}_{CO_2,PP} + \dot{m}_{CO_2,PU} \\ + \dot{m}_{CO_2,PVC} = \mathbf{19.0754}\ \frac{\boldsymbol{kg_{CO_2}}}{\boldsymbol{s}}\end{gathered} \tag{B.24}$$

CO:

Yields:

$$Y_{CO,wood} = 0.005\left[1+\frac{44}{\exp\,(\Phi/1.3)^{-3.5}}\right] = 0.1813\ \frac{kg_{CO}}{kg_{wood}} \qquad \text{(B.25)}$$

$$Y_{CO,PP} = 0.024\left[1+\frac{10}{\exp\,(\Phi/1.39)^{-2.8}}\right] = 0.1913\ \frac{kg_{CO}}{kg_{PP}} \qquad \text{(B.26)}$$

$$Y_{CO,PE} = 0.024\left[1+\frac{10}{\exp\,(\Phi/1.39)^{-2.8}}\right] = 0.1913\ \frac{kg_{CO}}{kg_{PE}} \qquad \text{(B.27)}$$

$$Y_{CO,PU} = 0.031\left[1+\frac{10}{\exp\,(\Phi/1.39)^{-2.8}}\right] = 0.2471\ \frac{kg_{CO}}{kg_{PU}} \qquad \text{(B.28)}$$

$$Y_{CO,PVC} = 0.063\left[1+\frac{7}{\exp\,(\Phi/0.42)^{-8}}\right] = 0.5040\ \frac{kg_{CO}}{kg_{PVC}} \qquad \text{(B.29)}$$

Mass flow rates:

$$\dot{m}_{CO,wood} = \dot{m}_{wood} \times Y_{CO,wood} = 15 \times 0.1813\ = 2.7196\ \frac{kg_{CO}}{s} \qquad \text{(B.30)}$$

$$\dot{m}_{CO,PP} = \dot{m}_{PP} \times Y_{CO,PP} = 1.04 \times 0.1913 = 0.1989\ \frac{kg_{CO}}{s} \qquad \text{(B.31)}$$

$$\dot{m}_{CO,PE} = \dot{m}_{PE} \times Y_{CO,PE} = 1.13 \times 0.1913 = 0.2161\ \frac{kg_{CO}}{s} \qquad \text{(B.32)}$$

$$\dot{m}_{CO,PU} = \dot{m}_{PU} \times Y_{CO,PU} = 1.37 \times 0.2471 = 0.3385\ \frac{kg_{CO}}{s} \qquad \text{(B.33)}$$

$$\dot{m}_{CO,PVC} = \dot{m}_{PVC} \times Y_{CO,PVC} = 1.42 \times 0.5040 = 0.7157\ \frac{kg_{CO}}{s} \qquad \text{(B.34)}$$

The total production rate of carbon monoxide is:

$$\dot{m}_{CO} = \dot{m}_{CO,wood} + \dot{m}_{CO,PP} + \dot{m}_{CO,PE} + \dot{m}_{CO,PP} + \dot{m}_{CO,PU} + \dot{m}_{CO,PVC} = \mathbf{4.1888}\ \frac{\boldsymbol{kg_{co}}}{\boldsymbol{s}} \tag{B.35}$$

***CH_4*:**

Yields:

$$Y_{CH_4,wood} = 0.001\left[1 + \frac{200}{\exp\,(\Phi/2.33)^{-1.9}}\right] = 0.0535\ \frac{kg_{CH_4}}{kg_{wood}} \tag{B.36}$$

$$Y_{CH_4,PP} = 0.006\left[1 + \frac{220}{\exp\,(\Phi/1.90)^{-2.5}}\right] = 0.5537\ \frac{kg_{CH_4}}{kg_{PP}} \tag{B.37}$$

$$Y_{CH_4,PE} = 0.007\left[1 + \frac{220}{\exp\,(\Phi/1.90)^{-2.5}}\right] = 0.6460\ \frac{kg_{CH_4}}{kg_{PE}} \tag{B.38}$$

$$Y_{CH_4,PU} = 0.005\left[1 + \frac{220}{\exp\,(\Phi/1.90)^{-2.5}}\right] = 0.4614\ \frac{kg_{CH_4}}{kg_{PU}} \tag{B.39}$$

$$Y_{CH_4,PVC} = 0.023\left[1 + \frac{25}{\exp\,(\Phi/0.42)^{-1.8}}\right] = 0.5644\ \frac{kg_{CH_4}}{kg_{PVC}} \tag{B.40}$$

Mass flow rates:

$$\dot{m}_{CH_4,wood} = \dot{m}_{wood} \times Y_{hc,wood} = 15 \times 0.0535 = 0.8032\ \frac{kg_{CH_4}}{s} \tag{B.41}$$

$$\dot{m}_{CH_4,PP} = \dot{m}_{PP} \times Y_{hc,PP} = 1.04 \times 0.5537 = 0.5759\ \frac{kg_{CH_4}}{s} \tag{B.42}$$

$$\dot{m}_{CH_4,PE} = \dot{m}_{PE} \times Y_{hc,PE} = 1.13 \times 0.6460 = 0.7300\ \frac{kg_{CH_4}}{s} \tag{B.43}$$

$$\dot{m}_{CH_4,PU} = \dot{m}_{PU} \times Y_{hc,PU} = 1.37 \times 0.4614 = 0.6321 \ \frac{kg_{CH_4}}{s} \tag{B.44}$$

$$\dot{m}_{CH_4,PVC} = \dot{m}_{PVC} \times Y_{hc,PVC} = 1.42 \times 0.5644 = 0.8014 \ \frac{kg_{CH_4}}{s} \tag{B.45}$$

The total production rate of methane is:

$$\begin{gathered}\dot{m}_{CH_4} = \dot{m}_{CH_4,wood} + \dot{m}_{CH_4,PP} + \dot{m}_{CH_4,PE} + \dot{m}_{CH_4,PP} + \dot{m}_{CH_4,PU} \\ + \dot{m}_{CH_4,PVC} = \boldsymbol{3.5426} \ \boldsymbol{\frac{kg_{CH_4}}{s}}\end{gathered} \tag{B.46}$$

HCl:

Yields:

HCl is produced only due to the burning of the PVC with the yield of 0.581 $\frac{kg_{HCl}}{kg_{PVC}}$.

Mass flow rate:

$$\begin{gathered}\dot{m}_{HCl,PVC} = \dot{m}_{PVC} \times Y_{HCl,PVC} = 1.63 \times 0.581 = \\ \boldsymbol{0.95} \ \boldsymbol{\frac{kg_{HCl}}{s}}\end{gathered} \tag{B.47}$$

Soot:

Yields:

$$Y_{soot,wood} = 0.015 \left[1 + \frac{2.5}{\exp{(\Phi/2.15)^{-1.2}}}\right] = 0.0276 \ \frac{kg_{soot}}{kg_{wood}} \tag{B.48}$$

$$Y_{soot,PP} = 0.059 \left[1 + \frac{2.2}{\exp{(\Phi/2.5)^{-1}}}\right] = 0.0962 \ \frac{kg_{soot}}{kg_{PP}} \tag{B.49}$$

$$Y_{soot,PE} = 0.06 \left[1 + \frac{2.2}{\exp{(\Phi/2.5)^{-1}}}\right] = 0.0978 \ \frac{kg_{soot}}{kg_{PE}} \tag{B.50}$$

$$Y_{soot,PU} = 0.227 \left[1 + \frac{2.2}{\exp{(\Phi/2.5)^{-1}}}\right] = 0.3701 \ \frac{kg_{soot}}{kg_{PU}} \tag{B.51}$$

$$Y_{soot,PVC} = 0.172\left[1 + \frac{0.38}{\exp{(\Phi/2.02)^{-8}}}\right] = 0.1941\ \frac{kg_{soot}}{kg_{PVC}} \tag{B.52}$$

Mass flow rates:

$$\dot{m}_{soot,wood} = \dot{m}_{wood} \times Y_{soot,wood} = 15 \times 0.0276 = 0.414\ \frac{kg_{soot}}{s} \tag{B.53}$$

$$\dot{m}_{soot,PP} = \dot{m}_{PP} \times Y_{soot,PP} = 1.04 \times 0.0962 = 0.1\ \frac{kg_{soot}}{s} \tag{B.54}$$

$$\dot{m}_{soot,PE} = \dot{m}_{PE} \times Y_{soot,PE} = 1.13 \times 0.0978 = 0.1105\ \frac{kg_{soot}}{s} \tag{B.55}$$

$$\dot{m}_{soot,PU} = \dot{m}_{PU} \times Y_{soot,PU} = 1.37 \times 0.3701 = 0.5070\ \frac{kg_{soot}}{s} \tag{B.56}$$

$$\dot{m}_{soot,PVC} = \dot{m}_{PVC} \times Y_{soot,PVC} = 1.42 \times 0.1941 = 0.2757\ \frac{kg_{soot}}{s} \tag{B.57}$$

The total production rate of soot is:

$$\begin{aligned}\dot{m}_{soot} &= \dot{m}_{soot,wood} + \dot{m}_{soot,PP} + \dot{m}_{soot,PE} + \dot{m}_{soot,PP} + \dot{m}_{soot,PU} \\ &+ \dot{m}_{soot,PVC} = \mathbf{1.4072}\ \boldsymbol{\frac{kg_{soot}}{s}}\end{aligned} \tag{B.58}$$

Now, the total mass flow rate of smoke and also the mass flow rate of each component in the smoke at the smoke inlet boundary are known. The mass fraction of each component of smoke is calculated based on the following expression:

$$x_\alpha = \frac{\dot{m}_\alpha}{\dot{m}_{smoke}} \tag{B.59}$$

Where, $\dot{m}_\alpha$ is the mass flow rate of component α, $\dot{m}_{smoke}$ is the total mass flow rate of smoke and x_α is the mass fraction of component α at the boundary. As mentioned before, the air was the bulk spice, so, only the mass fractions of CO_2, CO, CH_4, HCl and soot were needed for the boundary. Exactly the same process has been performed for the fire $100 \times 100\ m^2$ to calculate the total mass flow rate of smoke and also the mass fraction of each smoke component at the smoke boundary, however, the calculations for that are not written here so as to avoid repetition.